Late Paleozoic low-angle southward-dipping thrust in the Züünharaa area, Mongolia: Implication for the tectonic process of the Central Asian Orogenic belt

（モンゴル国，ズーンハラア地域における後期古生代の低角南傾斜衝上断層運動：中央アジア造山帯の地質構造発達史との関連について）

GANTUMUR, Onon

A dissertation for the degree of Doctor of Science

Department of Earth and Environmental Sciences,

Graduate School of Environmental Studies, Nagoya University

2017

Contents

Abstract

The Central Asian Orogenic belt (CAOB), which lies among the Siberian craton (SC), East European craton (EEC), North China block (NCB), and Tarim block (TB), is one of the largest Paleozoic-Mesozoic orogenic belts in the world. The Sayan-Baikal (SB) and Hangai-Daur (HD) belts between SC and NCB are, an especially, significant portion in the tectonics of the CAOB. The SB and HD belts are regarded as marginal parts of the Siberian continent. The HD belt, south of the SB belt, includes the following two types of terranes: (1) the terranes composed mainly of Cambrian–Ordovician proximal shallow-marine clastic rocks (e.g. Haraa terrane) and (2) the terranes composed of Paleozoic accretionary complexes (PAC). The Haraa terrane of the HD belt, which lies between the SB belt and PAC, is a key geologic unit to reveal the Paleozoic subduction process at the continental margin. However, little attention has been given to its tectonic significance. This study describes lithology, stratigraphy, geological structure, geochemistry and detrital zircon U-Pb age of Carboniferous sandstone, and magmatic zircon U-Pb age of granitic rock in the Züünharaa area (type locality of the Haraa terrane) to discuss the tectonic relationship between the SB and HD belts.

The Züünharaa area exposes metamorphosed Lower Cambrian (?) clastic rocks of the Haraa Group, Lower Devonian volcanic rocks of the Ulaan Öndör Formation, and Lower Carboniferous clastic rocks of the Örmögtei Formation, in ascending order. The Haraa Group is intruded by Cambrian and Silurian granitic rocks. The Haraa terrane is quite different from the PAC of the HD belt, which is composed of Upper Paleozoic clastic rocks, radiolarian chert, limestone and oceanic island basalt; resembles the SB belt, from a lithostratigraphical viewpoint. Therefore, it seems reasonable to suppose that the Haraa terrane, which has been regarded as a northern constituent of the HD belt so far, is excluded from the HD belt and is incorporated into the SB belt.

All rocks in the study area, except for the Örmögtei Formation, are cut by a low-angle southward-dipping thrust, and the rocks along the thrust are intensely fractured into the foliated

and non-foliated cataclasites to form a brittle shear zone up to ca. 40 m wide. The foliated cataclasite has clear P-Y fabric showing a top-to-the northward sense of shear. The granitic rock, cut by the thrust, has magmatic zircon U-Pb ages of 433–424 Ma, and the Örmögtei Formation covering the thrust yields Visean bryozoans at its type locality. The thrusting is, thus, assumed to have occurred between the latest Silurian and Visean.

The Late Paleozoic low-angle southward-dipping thrust, which is similar to that in the Haraa terrane, is widely recognized in the SB belt. On the other hand, contemporaneous southeast-verging folds and northward-dipping thrusts formed by northward subduction of oceanic plate have been described from the PAC.

The Carboniferous sandstones in both the Haraa terrane and PAC are very similar to each other in modal/chemical compositions and detrital zircon U-Pb age distribution. Furthermore, chemical data indicate that the sedimentary basins of these sandstones were located near an active continental margin. Thus, it is quite likely that the Haraa terrane and PAC had been located close together at an active continental margin in the Carboniferous.

This observation gives a strong suggestion that the structural contrast of the “SB belt + Haraa terrane (continental affinity) versus PAC” was formed in a same plate-convergent field, and it corresponds to the doubly-vergent structure which has been illustrated from the Alps, Andes, and many other orogenic belts. The doubly-vergent structure in the SB and HD belts was probably caused by the Late Paleozoic northward subduction of the Mongol–Okhotsk oceanic plate beneath the margin of the Siberian continent.

Introduction

The Altaid Collage (Sengör et al. 1993; Sengör and Natal'in 1996) or the Central Asian Orogenic belt (CAOB; e.g. Janh et al. 2000; Xiao et al. 2003; Windley et al. 2007) is one of the largest Paleo-Mesozoic orogenic belts in the world (Fig. 1a). The CAOB, which lies within the Siberian craton (SC), East European craton (EEC), North China block (NCB), and Tarim block (TB) includes continental fragments, low–high T/P metamorphic rocks, ophiolite, continental/oceanic volcanic arc rocks and accretionary complexes (e.g. Petrov et al. 2014). The geological structure of the CAOB is a key to understanding the Paleo-Mesozoic geodynamic processes of the Eurasian continent. The CAOB is generally considered to have been formed by the time-stepped subduction-accretions of various oceanic materials, volcanic arc magmatism, and collisions of the continental fragments which derived from the supercontinent Rodinia during the amalgamation of the SC, EEC, NCB, and TB. However, the detailed development process of the CAOB is still unclear (Fig. 1a; e.g. Sengör et al. 1993; Sengör and Natal'in 1996; Badarch et al. 2002; Xiao et al. 2003; Vernikovsky et al. 2003; Kovalenko et al. 2004; Windley et al. 2007).

The Mongolian territory (Fig. 1a) between SC and NCB makes up a significant portion of the Paleo–Mesozoic tectonics of the CAOB in northeastern Asia. The basement rocks of Mongolia are divided by the Main Mongolian Lineament (MML; e.g. Badarch et al. 2002; Tomurtogoo 2006; Kröner et al. 2007; Windley et al. 2007). North of the MML, the rocks of the Sayan-Baikal (SB) and Hangai-Daur (HD) belts are exposed (Fig. 1b). The SB belt is mainly composed of Precambrian metamorphic rocks, Neoproterozoic–Ordovician and Carboniferous-Permian granitic rocks, and Cambrian–Carboniferous dolomites-limestone and volcanic-clastic rocks. The Precambrian–Carboniferous rocks of the SB belt are intruded by the Permian–Triassic volcanic-plutonic rock complexes (Fig. 1b, e.g. Parfenov et al. 2009; Badarch 2005; Ruzhentsev et al. 2012; Donskaya et al. 2013). The SB belt is considered to be a collage of terranes that have been accreted to the SC, and behaved as a part of the continental margin of the SC (e.g. Parfenov et al. 2009; Bulgatov and Gordienko 2014). The rocks of the HD belt (Fig. 1b) can be divided

into the following two types: Cambrian–Ordovician proximal shallow-marine clastic rocks (Zag and Haraa terranes) and Paleozoic accretionary complexes (Tsetserleg, Harhorin, Asralt Hairhan, Daur, Aga, Onon, and Ulaanbaatar terranes; Tomurtogoo 2006, 2012; Kurihara et al. 2008). The Paleozoic accretionary complexes in the HD belt is considered to have been formed by the northward subduction of the oceanic plate of the Mongol–Okhotsk Ocean beneath the margin of the Siberian continent (Zorin 1999; Gordienko 2001; Kurihara et al. 2008; Tomurtogoo 2012; Donskaya et al. 2013; Ruppen et al. 2013). The Haraa terrane, which lies between the "Paleozoic continent" and the Paleozoic accretionary complex, is a key geologic unit to reveal the Paleozoic subduction process at the margin of the Siberian continent; however, little attention has been given to its tectonic significance.

A wide variety of ideas regarding the stratigraphy and geological structure of the Haraa terrane which were established independently with small respect to other studies, cause significant confusion (Fig. 2a; e.g. Tomur et al. 1994; Byamba and Binderya 1998; Purevsuren and Narantsetseg 1998; Tovuudorj et al. 2003). The Züünharaa area (type locality of the Haraa terrane) exposes Lower Cambrian (?) metamorphosed clastic rocks (Haraa Group), Lower Devonian volcanic rocks (Ulaan Öndör Formation), and Lower Carboniferous clastic rocks (Örmögtei Formation). For example, Byamba and Binderya (1998) regarded the rocks of Mt. Taijiin Gozgor (Fig. 2b) to be "Middle Cambrian – Lower Ordovician" metamorphosed clastic rocks of the Haraa Group; however, the geological map of the adjacent area to the west by Purevsuren and Narantsetseg (1998) includes significant amounts of Lower Devonian granitic rocks. The rocks at Mt. Dashdavaa (Fig. 2b) are assigned by Byamba and Binderya (1998) to the Lower Devonian Ulaan Öndör Formation, but are thought to be a part of the Cambrian–Ordovician Haraa Group by Tomur et al. (1994). Furthermore, the geological maps by Byamba and Binderya (1998), Purevsuren and Narantsetseg (1998), and Tomur et al. (1994) have significant contradiction in rock distribution and geological structure from the larger map by Tovuudorj et al. (2003); these maps are so different that it is difficult to find any similarities with

each other (Figs. 2b, c). Lithological, stratigraphical and structural interpretations based on geological maps are essential parts for establishing the tectonic setting. This means that the poor consistency of previously published geological maps is a significant obstruction to understanding the geological history of the entire Haraa terrane of the HD belt. This study describes lithology, stratigraphy, geological structure, geochemistry and detrital zircon U-Pb age of the Carboniferous sandstone, and magmatic zircon U-Pb age of granitic rock in the Züünharaa area to discuss the tectonic relationship between the SB and HD belts.

Geological setting of the Sayan-Baikal and Hangai-Daur belts

1. The Sayan-Baikal belt

The rocks of the Sayan-Baikal (SB) belt are divided into the following seven geological units: the Central Mongol and Tuva Mongol superterranes, the Dzhida, Khamar-Daban, Tunka, Ikat, and Eravna terranes (Fig. 1b; Parfenov et al. 2004a, 2009; Tomurtogoo 2006, 2012, 2014). Paleoproterozoic to Early Cambrian metamorphic rocks, ophiolitic rocks, and volcanic-clastic rocks are largely exposed in the Central Mongol and Tuva Mongol superterranes and in the Dzhida and Khamar-Daban terranes. The Central Mongol and Tuva Mongol superterranes are considered to be Precambrian continental fragments, while the Dzhida and Khamar-Daban terranes are regarded as Early Paleozoic accretion-collision orogens with a N-verging fold-thrust structure (Fig. 1b; e.g. Belichenko et al. 2003; Tomurtogoo 2006; Gordienko et al. 2007).

Paleozoic rocks occur in the Tunka, Ikat, and Eravna terranes (Parfenov et al. 2004a, 2009). The Tunka terrane, located on the southwest of the SC, consists mainly of Neoproterozoic–Lower Cambrian metamorphosed terrigenous rocks and limestone (Fig. 1b). These metamorphosed rocks are intruded by Tunka granite of the Sarkhoi plutonic complex, which gives a U-Pb age of 462.6 ± 7.8 Ma (Zhimulev et al. 2011). The Late Devonian–Early Carboniferous Sagan-Sair Formation overlies the Tunka granite and Neoproterozoic–Lower Cambrian metamorphosed rocks (Buslov et al. 2009; Zhimulev et al. 2011). The Neoproterozoic–Lower Cambrian metamorphosed rocks of the Tunka terrane take a N-verging fold-thrust structure (Buslov et al. 2009; Ryabinin et al. 2011; Zhimulev et al. 2011). The Ikat and Eravna terranes are primarily composed of Neoproterozoic–Carboniferous metamorphosed dolomite-limestone and terrigenous rocks with minor volcanic rocks (Mazukabzov et al. 2010). The Neoproterozoic–Carboniferous rocks of the Ikat and Eravna terranes take a N-verging fold-thrust structure (Ruzhentsev et al. 2006, 2012). The rocks in the southern part of the SB belt are intruded by the Permian–Triassic volcanic-plutonic rock complexes.

2. The Hangai-Daur belt

The rocks of the Hangai-Daur (HD) belt are divided into the following nine geologic units: Zag, Haraa, Tsetserleg, Harhorin, Asralt Hairhan, Daur, Aga, Onon, and Ulaanbaatar terranes (Fig. 1b; Bulgatov and Gordienko 1999, 2014; Tomurtogoo 2012, 2014). The HD belt is largely composed of accretionary complexes, except for the Zag and Haraa terranes which are dominated by Cambrian–Ordovician proximal shallow-marine clastic rocks. The Ulaanbaatar terrane (latest Devonian–Early Carboniferous accretionary complex) is composed of oceanic island alkaline basalt, Silurian–Devonian radiolarian chert, siliceous shale, mudstone, and sandstone, and the Harhorin and Tsetserleg terranes are equivalent to the Ulaanbaatar terrane (Kurihara et al. 2008; Tsukada 2010; Suzuki et al. 2012; Takeuchi et al. 2012; Nakane 2013; Purevjav et al. 2013; Ruppen et al. 2013; Tsukada et al. 2013). The Asralt Hairhan terrane is a metamorphic affinity of the Ulaanbaatar terrane (Tomurtogoo 2006, 2012; Gordienko et al. 2012). The Daur, Aga, and Onon terranes are accretionary complexes dominated by sandstone-mudstone with dismembered ophiolite and arc-related volcanic rocks with minor amounts of radiolarian chert and limestone (Bulgatov and Gordienko 1999; Zorin 1999; Badarch 2005; Tomurtogoo 2012).

The Zag terrane consists of pelitic-psammitic schist of the Zag Group which yields muscovite K-Ar ages of 453.9±9.1 Ma and 447.4±9.0 Ma (Kurimoto et al. 1998; Badarch 2005). The rocks of the Zag Group are intruded by Ordovician granite, and are overlain by Devonian–Permian clastic rocks (Badarch et al. 2002; Tomurtogoo 2006). The Haraa terrane is largely composed of Cambrian–Ordovician metamorphosed clastic rocks of the Haraa Group (Tomurtogoo 2006, 2012). The rocks of the Haraa Group are intruded by the Boroogol plutonic rock complex giving the U-Pb age of 460–440 Ma (Kröner et al. 2007; Hou et al. 2010). The Haraa Group and Boroogol plutonic rock complex are unconformably overlain by Devonian–Permian volcanic-clastic rocks (Badarch et al. 2002). The Late Paleozoic–Mesozoic plutonic rocks intrude into the older sedimentary and igneous rocks of the HD belt (Tomurtogoo 2006; Donskay et al. 2013).

The bedding and structural planes in the rocks of the Zag and Tsetserleg terranes generally trend northwest and steeply dip north- or southward when west of the HD belt, whereas those in the Haraa, Asralt Hairhan, Ulaanbaatar, Daur, and Aga terranes trend northeast and steeply dip northward in the east (e.g. Zorin 1999; Buchan et al. 2001; Badarch et al. 2002; Kurihara et al. 2008; Takeuchi et al. 2012; Purevjav et al. 2013; Tsukada et al. 2013). The rocks of the Harhorin terrane trend north-northwest and dip southwestward, and are in fault contact with the Tsetserleg terrane in the west (Tseden et al. 1992; Tsukada et al. 2010; Purevjav et al. 2013). The rocks of the Onon and Aga terranes trend northeast (Zorin 1999). The southeast-verging composite folds associated with northward-dipping thrusts are recognized in the rocks of the Asralt Hairhan and Ulaanbaatar terranes (Kurihara et al. 2008; Gordienko et al. 2012; Takeuchi et al. 2012).

Geological description of the Züünharaa area

The Züünharaa area (Fig. 1b) is located about 150 km north of Ulaanbaatar city, Mongolia. This area exposes metamorphosed clastic rocks of the Haraa Group, volcanic rocks of the Ulaan Öndör Formation, and clastic rocks of the Örmögtei Formation in ascending order (Figs. 3a, 4). The area includes the type localities of the Haraa Group and Örmögtei Formation (Bobrov et al. 1964; Amantov et al. 1966). The Haraa Group is intruded by granitic rocks. A part of the granitic rocks is monzogranite according to the I.U.G.S. classification of plutonic rocks (Streckeisen and Le Bas 1991). The granitic rocks gradually change into finer rhyolitic rocks in some places, and are intruded by later small dikes of diorite and dacite (Figs. 3a, 4). The volcanic rocks of the Ulaan Öndör Formation unconformably overlie the Haraa Group and the granitic rocks. The Haraa Group, granitic rocks and Ulaan Öndör Formation are cut by low-angle southward-dipping thrust throughout this area (Figs. 3a, b). The rocks along the thrust are fractured into the foliated and non-foliated cataclasites to form brittle shear zone up to ca. 40 m wide. The clastic rocks of the Örmögtei Formation unconformably overlie the granitic rocks and the brittle shear zone with basal conglomerate (Figs. 3a, b, 4). Younger NW-trending high-angle faults are recognized in the central and eastern parts of the study area. These high-angle fault cut the brittle shear zone near Mt. Ovoot and Mt. Zörüü (Fig. 3a). The newly established stratigraphy and structure in this area are described below.

1. Sedimentary rocks

1.1. Haraa Group

Definition: The metamorphosed clastic rocks in this area (Fig. 3) were initially assigned to the "greywacke" of the Proterozoic Bahar Formation (Usov 1916). Amantov (1966) redefined the Bahar Formation to the Haraa Group, and subsequently divided it into the lower unit (metasandstone–slate–quartzite), middle unit (sandstone-dominated), and upper unit (phyllitic sandstone–slate). The metamorphosed clastic rocks in the study area correspond to the middle unit of the Haraa Group (Tomur et al. 1994; Purevsuren and Narantsetseg 1998).

Distribution: The rocks of the Haraa Group are exposed in the western and eastern parts of the study area (Fig. 3a).

Lithology and stratigraphy: The rocks of the Haraa Group consist largely of metamorphosed sandstone, and are intruded by granitic rocks (Fig. 4). Sandstone is usually fine- to medium-grained, sub-angular, and well- to moderately-sorted. The sandstone intercalates mudstone layer to form the alternating beds of sandstone and mudstone. The alternating beds of sandstone and mudstone show graded bedding in some places (Fig. 5a). The thickness of a bed varies from several millimeters to several centimeters. Phyllitic sandstone, slate, and hornfels are commonly observed near the boundary with the granitic rocks.

Petrography: The sandstone commonly includes quartz, feldspar, sphene, zircon and opaque minerals (Figs. 6a, b). Epidote, biotite, actinolite and hornblende chiefly occur in the rocks of Haraa Group as metamorphic minerals. Hornblende and feldspar are partly altered to chlorite and muscovite. Opaque minerals are common, while sphene and zircon are rare.

Structure: The bedding planes trend northwest and steeply dip southward in the western part of the study area. In the eastern part, the rocks are homocline striking N 40°–60° E and dipping 40°–65° N at the southern side and are complexly folded with sub-horizontal axes at northern side (Figs. 3a, b). The folds are bent around an axis that plunges steeply northeast.

Thickness: The total thickness of the metamorphosed clastic rocks is more than 2000 m (Fig. 4).

1.2. Ulaan Öndör Formation

Definition: The volcanic rocks in and around the Züünharaa area were once defined as the Lower Permian “volcanic-terrigenous unit” by Khulesh and Gorokhov (1961). Campe et al. (1975) redefined it as the Devonian Ulaan Öndör Formation (volcanic rock dominant) and Ajnai Formation (clastic rock dominant) in ascending order in the Zuunmod area, 30 km southeast from the study area (Fig. 2a). The volcanic rocks in the study area are assigned to the Ulaan Öndör Formation (Purevsuren and Narantsetseg 1998).

Distribution: The rocks of the Ulaan Öndör Formation occur as small exposures in the central and western parts of the study area.

Lithology and stratigraphy: The Ulaan Öndör Formation unconformably overlie the Haraa Group and the granitic rocks (Figs. 3a, 4). This formation is composed mainly of rhyolitic–dacitic varicolored lava and felsic tuff breccia, in ascending order (Fig. 4). Tuffaceous sandstone-mudstone beds, up to 1 m thick, are rarely intercalated in the felsic tuff breccia. The rhyolitic to dacitic lava includes phenocrysts of quartz and feldspar in a microcrystalline groundmass with amygdules infilled by quartz and calcite. The felsic tuff breccia is yellowish green, clast-supported and poorly sorted (Fig. 5c). It includes abundant angular to sub-rounded clasts of rhyolitic–dacitic lava. Clasts of sandstone and mudstone are also rarely included. The clasts are up to 10 cm in size.

Petrography: The rhyolitic–dacitic lava chiefly has a porphyritic texture (Fig. 6c). Phenocrysts (ca. 40 vol%) of quartz, K-feldspar, and plagioclase in the lava are tabular and/or prismatic, and they are up to 3 mm in length along their major axis. Quartz shows clear undulose extinction, while, K-feldspar shows micro-perthitic texture. Accessory minerals such as muscovite and biotite occur as flakes or clots. Zircon, apatite, and sphene are rarely present. The felsic tuff breccia includes abundant rhyolitic-dacitic rock fragments, quartz and feldspar crystals and minor amounts of exotic clasts of sandstone. The size of the fragments in the felsic tuff breccia is up to 3 cm. Tuffaceous sandstone includes subangular felsic volcanic rock fragments, quartz, feldspar, and opaque minerals in a finer matrix (Fig. 6d).

Structure: The bedding planes generally trend N 60° E and dip 35°–70° N (Figs. 3a, b).

Thickness: The total thickness is more than 300 m (Fig. 4).

Age: Campe (1975) assigned the Ulaan Öndör Formation at the Zuunmod area to the Lower Devonian period in stratigraphic relationship with the Ajnai Formation, where a Givetian brachiopod fossil assemblage (e.g. *Atrypa* sp., cf. *Uncinulus* sp., *Productella* sp., *Stropheodonta*

sp.) is found. Therefore, the rocks of the Ulaan Öndör Formation in this area are inferred to be Lower Devonian, as well.

1.3. Örmögtei Formation

Definition: Obruchev (1893) first defined the clastic rocks at Mt. Örmögtei, 45 km north from the study area, as a "terrigenous basin", and Bobrov (1964) subsequently redefined it as the Lower Carboniferous Örmögtei Formation. Type section for this formation is divided into the lower (sandstone-conglomerate dominant) and upper members (sandstone-mudstone dominant) with a total thickness of 2500 m (Bobrov 1964). The clastic rocks covering the granitic rocks in the Züünharaa area are correlated to the Örmögtei Formation (Purevsuren and Narantsetseg 1998).

Distribution: The clastic rocks of the Örmögtei Formation occur at the central part of the study area (Figs. 3a, 7).

Stratigraphy and lithology: This formation unconformably overlies the granitic rocks and is subdivided into the lower and upper parts (Figs. 3a, b, 4, 5d). The lower part consists of clast-supported conglomerate (Fig. 4, h1 in Fig. 8), medium- to coarse-grained massive sandstone (h2 in Fig. 8), and mudstone (h3 in Fig. 8). The upper part consists of matrix-supported conglomerate (h4 and h7 in Fig. 8), alternating beds of sandstone and mudstone (h5, h8 and h10 in Fig. 8), and fine- to coarse-grained bedded sandstone (h6 and h9 in Figs. 4, 8).

The clast-supported conglomerate of the lower part includes abundant boulders, up to 3 m in size, derived from the basement granitic rocks. Massive sandstone is largely composed of quartz and feldspar grains and includes rounded cobbles and pebbles of porphyritic granite-rhyolite (Fig. 9a). Mudstone, which overlies massive sandstone, includes a few fragments of unidentified brachiopod and crinoid fossils (Figs. 8, 9b).

The matrix-supported conglomerate of the upper part conformably overlies the massive mudstone of the lower part (Fig. 8). This conglomerate includes abundant well-rounded clasts of porphyritic granite-rhyolite, up to 20 cm in size, and a minor amount of sub-rounded clasts of

mudstone in a fine- to medium-grained sandstone matrix (Fig. 9c). The alternating beds of sandstone and mudstone overlies the matrix-supported conglomerate (Fig. 8). The sandstone of the alternating beds is composed largely of plagioclase, K-feldspar, and volcanic rock fragments, and it includes a minor amount of quartz, muscovite, biotite, epidote, and chlorite. Sphene, apatite, and zircon are rarely included in the alternating beds of sandstone and mudstone. Each bed is several centimeters thick. Sedimentary structures such as graded bedding and cross lamina are observed in the alternating beds (Fig. 9d). Some mudstone layers in the alternating beds yield unidentified brachiopod and crinoid fossils (Figs. 8, 9b). The bedded sandstone overlies the alternating beds of mudstone and sandstone (Fig. 8). This sandstone is dominated by plagioclase, K-feldspar, and volcanic rock fragments, which is the same as the sandstone of the underlying alternating beds. Several well-rounded clasts of felsic volcanic rocks, up to 5 cm in size, are included in the bedded sandstone.

Petrography: Twelve representative samples of fine- to medium-grained sandstones from horizons h2, h5, h6, h8, h9, and h10 were taken for modal analysis (Fig. 8). 500 points were counted on each thin section using the Gazzi-Dickinson method (Ingersoll et al. 1984). The main framework constituents are monocrystalline quartz (Qm), polycrystalline quartz (Qp), K-feldspar (Kfs), plagioclase (Pl), lithic fragments (Lf), mica minerals (MM), other minerals (OM), and matrix (Mx) (Fig. 11a). Data were plotted on the Q-F-R diagram (Fig. 11b; Okada 1971).

Three samples from the horizon h2 of the lower part are moderately- to well-sorted and include sub-angular to angular grains of quartz, K-feldspar, plagioclase, and volcanic rock fragments embedded in a finer matrix (Figs. 10a, b). Quartz shows undulatory extinction. K-feldspar shows micro-perthite texture. Plagioclase is clear and shows twinning. Volcanic rock fragments are very rare. The matrix (up to 5 vol%) of massive sandstone from h2 includes microcrystalline chlorite, sericite, biotite, quartz, and feldspar. It also includes small amounts of monazite, apatite, zircon, and opaque minerals. Calcareous cement is not observed. The sandstone from h2 is more enriched in Qm (34 vol%) than Qp (4 vol%). Feldspar content (F=Kfs+Pl) ranges

from 45 to 52 vol% (average of 49 vol%), and Kfs is more common than Pl. Lithic fragment content ranges from 3 to 6 vol% (average of 4 vol%) (Fig. 11a).

Nine samples from the upper part (horizons h5, h6, h8, h9, and h10) are moderately- to poorly sorted and include abundant sub-angular to sub-rounded grains of K-feldspar, plagioclase, and volcanic rock fragments such as andesite, dacite, and rhyolite (Figs. 10c, d). Minor amounts of quartz and clast of mudstone and granite are also included in the all horizons of the upper part. The modal compositions of the samples from upper part are similar to each other (Figs. 11, 12a). The sandstone includes much more feldspar and lithic fragments (averages of 41 vol% and 33 vol%, respectively) than quartz (average of 11 vol%). The sandstone includes minor amounts of chlorite, biotite, and sericite, and lesser amounts of zircon, sphene, apatite, and opaque minerals. The matrix of sandstone is composed of 9 vol% of microcrystalline quartz, feldspar, and lithic fragments of igneous rocks (Figs. 10c, d, 11a). Calcareous cement is very rare.

The massive sandstone from h2 of the Örmögtei Formation has a significantly different modal composition from the other sandstones (Figs. 11a, b). The abundance of quartz and feldspar in h2 may be caused by significant inference of the underlying basement granitic rocks (Figs. 7, 8). The sandstones of the Örmögtei Formation are classified as feldspathic arenite in the Q-F-R diagram (Fig. 11b, Okada 1971).

Structure: The Örmögtei Formation is folded with a low-angle axis gently plunging westward (Figs. 3a, 7). The southern wing strikes N 30°–50° E and dips 15°–45° N, and the northern wing strikes N 45°–60° W and dips 15°–35° S to take a synclinal structure (Figs. 3a, 7). Bedding-parallel cleavages, developed in the alternating beds of sandstone-mudstone, strike N 70°–80° E and dip 45°–80° S (Fig. 7).

Thickness: The total thickness of this formation is more than 1700 m (Figs. 7, 8).

Age: Ariunchimeg (1992, 2011) reported Visean plant fossils (e.g. *Tomiodendron ex gr.kemerovience)* and bryozoans (e.g. *Sulcoretepora dichotoma minor*, *Dyscritella mergensis,*

Lanopora eximia) from the Örmögtei Formation in the type section. The formation in the Züünharaa area are thus assumed to be Visean.

2. Granitic rocks

Definition: The granitic rocks in the Züünharaa area were previously identified as "leucogranite" and "granite-rhyolite porphyry" by Byamba and Binderya (1998) and Purevsuren and Narantsetseg (1998). In this study, the granitic rocks are reclassified as the following two types based on their texture: (1) equigranular granite (monzogranite) and (2) porphyritic granite-rhyolite (Figs. 3, 4).

Distribution: The equigranular granite is exposed in the northern, southern, and western parts, and porphyritic granite-rhyolite occupies the central part of the study area (Fig. 3a).

Lithology and petrography: Xenoliths, which are derived from the metamorphosed clastic rocks of the Haraa Group, are contained in the granitic rocks (Fig. 5b). The equigranular granite generally includes quartz (40 vol%), K-feldspar (36 vol%), and plagioclase (18 vol%), and minor amounts of hornblende, biotite, apatite, zircon, and opaque minerals. The quartz, feldspar, and plagioclase are 1–3 mm in size (Fig. 12a). Euhedral quartz is clear and shows undulose extinction. Subhedral to euhedral crystals of K-feldspar (mainly orthoclase) show micro-perthite texture and/or twinning. Plagioclase shows stripe twining. K-feldspar and plagioclase both include microcrystalline sericite owing to alteration.

The porphyritic granite is inter-gradual with porphyritic rhyolite, and the boundary between them is obscure. Porphyries of quartz, K-feldspar, and plagioclase, up to 7 mm in size, are embedded in a finer groundmass (less than 0.1 mm in size) in the porphyritic granite (Fig. 12b). Minor amounts of biotite, hornblende and epidote are also included in the porphyritic granite. Some porphyritic granite contains abundant crystals of sphene, zircon, and opaque minerals. The porphyritic granite includes quartz (31 vol%), K-feldspar (51 vol%), plagioclase (12 vol%),

biotite-hornblende (3 vol%) and lesser amounts of apatite, zircon and opaque minerals. The porphyritic rhyolite includes phenocrysts of quartz, K-feldspar, plagioclase, minor amounts of biotite and hornblende, and lesser amounts of zircon and opaque minerals in a finer (up to 0.05 mm in size) groundmass (Fig. 12c). Phenocrysts are up to 3 mm in size and occupy ca. 30 vol% of the rhyolite. Some biotite and hornblende, up to 1 mm in size, occur as clots in a finer groundmass.

Age: The equigranular granite and porphyritic granite-rhyolite have magmatic ages of ca. 489 Ma and ca. 433–424 Ma, respectively. The details of the dating are described later.

3. Small dikes of diorite and dacite

Small dikes of diorite and dacite intrude into the equigranular and porphyritic granites (Figs. 3, 4, 5d). The diorite dike is composed of plagioclase (50 vol%) and hornblende (45 vol%) with small amounts of quartz, K-feldspar, biotite, sphene, and opaque minerals. Euhedral to subhedral plagioclase shows clear stripe and pericline twinning (Fig. 12d). The dacite dike includes abundant phenocrysts of plagioclase in a finer groundmass. Phenocrysts of plagioclase are euhedral to subhedral, elongated tabular laths up to 2 mm in size. The groundmass has abundant microcrystalline hornblende, biotite, and quartz and shows a hyalopilitic texture.

4. Low-angle southward-dipping thrust

The low-angle thrust, trending E–W and dipping gently southward, cuts all geologic units except for the Örmögtei Formation throughout this area (Figs. 3a, b, 7). The rocks in and around the thrust were intensely fractured to form cataclasite. The brittle shear zone composed of the cataclasite and fractured rocks has a maximum width of 40 m, and is exposed in places at 900 m to 1100 m elevations (Figs. 3b, 13a). The distribution of the brittle shear zone strongly suggests the sub-horizontal fault plane throughout the study area (Figs. 3a, 14a, b).

Abundant angular clasts derived from the host rocks such as meta-sandstone, porphyritic granite-rhyolite, volcanic rocks and others are included in a finer matrix, demonstrating random fabric in the cataclasite (Figs. 13b, c). The cataclasite is foliated in places but is generally non-foliated. The clasts are formless, lenticular, spherical or tabular, and vary in size from several millimeters to several centimeters (Fig. 13c). The cracks in the clasts are filled by grains fed from the matrix (Fig. 13d). Epidote, which suggests a formation temperature above ca. 200° C (Henley and Ellis 1983), is not observed in the matrix of the cataclasite. No evidence of ductile deformation such as grain boundary migration, sub-grain rotation, bulging, or undulose extinction, are observed in the matrix. The matrix occupies more than 40% of the total volume in the cataclasite part. According to the classification of fault rock by Woodcock and Mort (2008), the rocks in and around the thrust are protocataclasite. Experimental studies (e.g. Sibson 1983; Scholz 1988; Passchier and Trouw 1998) suggest that cataclasite in a brittle shear zone generally occur at conditions less than ca. 300° C and 4 kbar. Taking everything into considerations, the present cataclasite seems to have been formed under conditions of less than ca. 200 ° C and 4 kbar.

The foliated cataclasite shows composite planar structures such as R_1-, P- and Y- shears of subsidiary fractures or so-called Riedel shears (Riedel 1929). The respective spacing of the P- and Y- shears are ca. 10 cm and ca. 40 cm (Figs. 14c, 15a). Dip angle of P-shear is slightly higher than Y-shear (Fig. 15b). The Y-shears generally strike N 40° W to N 10° E (average of N 18° W) and dip 10° to 35° S (average of 9° S), and the P-shears strike N 50° W to N 30° E (average of N 76° E) and dip 30° to 60° S (average of 27° S) (Fig. 15c). The P-Y fabrics in the foliated cataclasite suggests top-to-the northward sense of shear (Figs. 14c, 15).

Zircon LA-ICP-MS U-Pb age determination

1. Samples and analytical procedures

Zircon U-Pb dating of the granitic rocks was carried out using Laser Ablation-Inductively Coupled Plasma-Mass Spectrometry (LA-ICP-MS); a sample from the equigranular granite (#12Hr1601) and two samples from the porphyritic granite-rhyolite (#11Hr54 and #12Hr1011) were analyzed to estimate the timing of the low-angle south-dipping thrust in the study area (Figs. 3, 7). Additionally, zircons from two sandstone samples (#12Hr0814 and #12Hr0819) from horizons h6 and h8 of the Örmögtei Formation were dated to discuss their provenance (Figs. 7, 8).

The zircons were concentrated using conventional mineral-separation techniques, which included crushing and pulverizing followed by hand-separation using magnets. These zircon grains were then mounted in an epoxy resin and diamond polished to expose the interior. In order to investigate the internal structure of the individual grains, a scanning electron microscope (SEM; Hitachi S-3400N equipped with Gatan MiniCL) installed at Nagoya University was used to obtain backscattered electron (BSE) and cathode luminescence (CL) images.

The zircons were analyzed by LA-ICP-MS (Agilent 7700x connected with the NWR-213 laser ablation system, Electro Scientific Industries, Inc.) installed at Nagoya University. The ablation pit size was 25 μm under conditions of 10 Hz repetition rates with energy densities of ~12 J/cm^2. Materials used for calibration were 91500 standard zircon (1062.4 Ma; Wiedenbeck et al. 1995) and silicate glass reference materials produced by the National Institute of Standards and Technology (NIST): SRM 610 (Horn and Von Blanckenburg 2007). Further details on accuracy and reproducibility can be found in Orihashi et al. (2008), Iwano et al. (2013) and Kouchi et al. (2015).

2. Zircon U-Pb age of the granitic rocks

The analyzed zircon grains are colorless to light brown, 50–200 μm in length along their major axes, and have a length-to-width ratio of 2:1. These zircon grains mostly occur as subhedral to euhedral prisms and contain inhered cores with mantle overgrowth showing concentric zoning (Figs. 16a–c). As a result of the BSE and CL examination, a total of 123 zircon grains from granitic rocks, with an exposure of more than 40 μm in diameter on the epoxy resin, were chosen for analysis from samples #12Hr1601 (equigranular granite), #11Hr54 (porphyritic granite) and #12Hr1011 (porphyritic rhyolite). Of these, 17 grains were ablated at their inherited core and oscillatory zoned rim. Data were obtained from a total of 140 analytical spots and plotted in a concordia diagram using Isoplot 3.75 software (Ludwig 2012). A total of 77 data points were excluded from examination for various reasons such as being discordant, having greater than 5.00 MSWD, less than 0.05 concordia age probability, or ages with an error of >100 m.y. The remaining 63 concordant data points (Table 1) were used in this study to calculate weighted mean ages of each sample (Figs. 17a, b, c). It is generally accepted that zircon grains with a high Th/U ratio (> 0.2) are of magmatic origin, whereas those with a low Th/U ratio (< 0.1) have undergone a secondary process such as metamorphism and hydrothermal alteration (Hartmann et al. 2000; Hartmann and Santos 2004). The zircons in the present study, showing a high Th/U ratio (0.21–0.79), are quite likely to have a magmatic origin (Table 1).

2.1. Sample #12Hr1601

This sample was collected from non-deformed equigranular granite, which is cut by low-angle south-dipping thrust (Fig. 3). It is coarse and holocrystalline, dominated by microcline, plagioclase, hornblende and biotite with minor amounts of zircon. The zircons from the sample are mostly light brown, subhedral to euhedral, semi-transparent, and up to 200 μm in length along their major axis. Most of the zircons have a few inclusions and cracks. Some zircons are dark and unzoned in CL (Fig. 16a).

The Th/U ratio is 0.21–0.50 (Table 1a). The ages from 31 concordant analyses are grouped at 541 ± 10 Ma (from 10 data points, MSWD = 2.60, probability = 0.005) and 498 ± 3 Ma (from 21 data points, MSWD = 1.20, probability = 0.21). The older age (ca. 541 Ma) was obtained from inherited cores within the zircon samples. The younger age (ca. 498 Ma) likely indicates the age of the magmatic event of the equigranular granite (Fig. 17a).

2.2. Sample #11Hr54

This sample was taken from fractured porphyritic granite near the low-angle south-dipping thrust (Fig. 3). It is coarse and holo- to hypocrystalline, dominated by quartz, K-feldspar, and plagioclase with minor quantities of sphene, zircon, and opaque minerals. The zircons from this sample are yellow to colorless, transparent, euhedral to subhedral, up to 150 μm in length along their major axis, and have a length-to-width ratio of 2:1. The zircons have irregular cracks, and commonly include apatite needles. Some zircons have inherited cores and mantle overgrowth showing concentric oscillatory zones in CL (Fig. 16b).

The Th/U ratio is 0.39–0.58 (Table 1b). The ages from 23 concordant analyses are grouped at 482 ± 6 Ma (from 6 data points, MSWD = 1.50, probability = 0.20), 458 ± 4 Ma (from 13 data points, MSWD = 1.90, probability = 0.03), and 433 ± 7 Ma (from 4 data points, MSWD = 0.02, probability = 1.00). The oldest group, mostly obtained from the inherited core of the grain, coincides to the magmatic age of equigranular granite. The weighted mean ages of ca. 458 Ma and ca. 433 Ma were obtained from the mantle part of zircons (Fig. 17b, Table 1b). The youngest age is 432 ± 13 Ma (MSWD = 1.05, probability = 0.31; Fig. 17b). The ca. 482 Ma and ca. 458 Ma are likely inherited ages and ca. 433 Ma likely corresponds to a magmatic event of the porphyritic granite (Fig. 17b).

2.3. Sample 12Hr1011

This sample is a clast in the cataclasite of the thrust. It is fine porphyritic rhyolite with phenocrysts of quartz, K-feldspar, and plagioclase. The zircons from this sample are commonly

needle-shaped, euhedral, transparent, and range from 50 to 150 μm in length along their major axis. The zircons have thin cracks and rarely include apatite needles. Most grains show concentric oscillatory zoning in CL (Fig. 16c).

The Th/U ratio is 0.35–0.79 (Table 1c). The 9 concordant data points were obtained from inherited cores and mantles of the 6 zircon grains (Fig. 17c). The mantles of zircons give a weighted mean age of 454 ± 7 Ma (MSWD = 0.20, probability = 0.96), and two inherited cores give 524 ± 16 Ma (MSWD = 0.28, probability = 0.10) and 484 ± 21 Ma (MSWD = 0.05, probability = 0.82; Fig. 16c). The youngest age, 424 ± 18 Ma (MSWD = 0.56, probability = 0.46), was obtained from an oscillatory zoned rim of a zircon grain (Fig. 16c). The ca. 454 Ma are likely inherited ages and ca. 424 Ma likely correspond to a magmatic event of the porphyritic rhyolite (Fig. 17c).

3. Zircon U-Pb age of the detrital zircons from sandstone of the Örmögtei Formation

The analyzed zircon grains are colorless to yellow, anhedral to subhedral, transparent, 50–100 μm in length along their major axes and have a length-to-width ratio of 2:1. As a result of the BSE and CL examination, a total of 172 zircon grains from samples #12Hr0814 and #12Hr0819, with an exposure of more than 40 μm in diameter on the epoxy resin, were chosen for analysis. Data were obtained from a total of 172 analytical spots and plotted in a concordia diagram using Isoplot 3.75 software (Ludwig 2012). A total of 77 data points were excluded from examination for various reasons such as being discordant, having greater than 5.00 MSWD, less than 0.05 concordia age probability, or ages with an error of >100 m.y. The remaining 95 concordant data points were used in this study (Table 2).

3.1. Sample #12Hr0814

Sample #12Hr0814 is moderately sorted and includes very coarse- to medium grained quartz, feldspar, and igneous rock fragments. It includes sphene, zircon, and opaque minerals. The detrital zircons show oscillatory zoning in CL and have small inclusions and thin cracks. The

Th/U ratio is 0.47–2.10 (Table 2a). The ages from 30 concordant analysis exhibit a significant age peak of 358 Ma in age probability (Fig. 18a). The oldest detrital zircon is 974 ± 17 Ma (MSWD = 0.14, probability = 0.71) and the youngest detrital zircon is 321 ± 10 Ma (MSWD = 3.8, probability = 0.05; Figs. 16d, 18a).

3.2. Sample #12Hr0819

The sample #12Hr0819 is composed mainly of plagioclase, volcanic rock fragments (felsic tuff, andesite, polycrystalline quartz), and minor amounts of K-feldspar and quartz. Lesser amounts of zircon, sphene, and opaque minerals are recognized. The modal composition of the sample #12Hr0819 is similar to that of sample #12Hr0814. Most zircons have inclusions and cracks and show oscillatory zoning in CL. The Th/U ratio of zircon ranges from 0.33 to 2.72 (Table 2b). The ages from 65 concordant analysis exhibit a significant age peak of 363 Ma in age probability (Fig. 18b). The oldest and youngest detrital zircons are 1003 ± 28 Ma (MSWD = 0.016, probability = 0.9) and 321 ± 17 Ma (MSWD = 2.5, probability = 0.11), respectively (Figs. 16e, 18b).

Chemical composition of the sandstone of the Örmögtei Formation

1. Samples and analytical procedures

The modal composition suggests that the massive sandstone from horizon h2 of the Örmögtei Formation has significant inference from the basement granitic rocks, and there is a possibility that the sandstone does not have the general features of this formation (Figs. 7, 8, 11). Therefore, nine sandstone samples from the upper part were used for analysis to infer the rock type exposed at the provenance area and tectonic environment of the time (Fig. 8, Table 3). The weathered surfaces and veins of the samples were removed. Samples were crushed and milled using the stamp and agate mills. Glass beads were prepared by fusing mixtures of 1.5 g of powdered sample with 6.0 g of lithium tetraborate. Major and trace elements were determined by X-ray fluorescence (XRF). The XRF analysis was carried out at Nagoya University, using a Rigaku ZSX Primus II-N equipped with a Rh X-ray tube (40kV, 70 mA). Calibration was carried out using standard rock samples issued by the Geological Survey of Japan and the composite standards prepared by Yamamoto and Morishita (1997) for the major and trace elements. Analytical precision of major elements was estimated to be <1% for Si and about 3% for most other elements; exceptions include TiO_2 and MnO, whose analytical precision is >3% when the measured level is <0.1% (Takebe and Yamamoto 2003), and trace elements were estimated to be <10% (Yamamoto and Morishita 1997).

2. Chemical description of the sandstone samples from the Örmögtei Formation

The data of the major and trace elements are given in Table 3. SiO_2 concentration of the samples ranges from 62 to 71 wt%, with an average of 66 wt%. The loss of ignition (LOI) of the samples is less than 2.5 wt%. In the other major element concentrations: TiO_2 is from 0.56 to 0.83 wt% (average 0.69 wt%); Al_2O_3 is from 15 to 18 wt% (average 17 wt%); Fe_2O_3 is from 3.0 to 5.2 wt% (average 4.4 wt%); MnO is from 0.036 to 0.091 wt% (average 0.059 wt%); MgO is from 0.76 to 1.9 wt% (average 1.3 wt%); CaO is from 0.86 to 3.3 wt% (average 1.8 wt%); Na_2O is

from 2.9 to 7.7 wt% (average 5.5 wt%); K_2O is from 1.28 to 3.79 wt% (average 1.98 wt%); P_2O_5 is from 0.14 to 0.21 wt% (average 0.18 wt%).

For trace element concentrations: Co is from 3 to 7 ppm (average 5 ppm); Cr is from 1 to 25 ppm (average 8 ppm); Ni is from 7 to 15 ppm (average 9 ppm); Cu is from 1 to 18 ppm (average 12 ppm); Zn is from 71 to 105 ppm (average 87 ppm); Ga is from 19 to 25 ppm (average 23 ppm); Rb is from 29 to 122 ppm (average 59 ppm); Sr is from 167 to 995 ppm (average 625 ppm); Y is from 16 to 39 ppm (average 22 ppm); Zr is from 211 to 278 ppm (average 241 ppm); Nb is from 5 to 12 ppm (average 7 ppm); Pb is from 20 to 48 ppm (average 32 ppm); Th is from 8 to 17 ppm (average 11 ppm).

Fig. 19 shows a diagram of the Upper Continental Crust (UCC)-normalized multi-element pattern. The diagram shows a great enrichment in Na_2O and depletion in MnO, MgO, CaO, and K_2O compared with a representative UCC composition, though SiO_2, TiO_2, Al_2O_3, Fe_2O_3, and P_2O_5 are nearly identical to the UCC.

Discussion

1. Regional correlation of the Haraa terrane

The terranes (e.g., Harhorin, Asralt Hairhan, and Ulaanbaatar terranes, Fig. 1b) composed of Paleozoic accretionary complexes (PAC) in the central part of the HD belt are largely composed of Carboniferous clastic rocks with Silurian–Devonian radiolarian chert, siliceous shale, and oceanic island basalt (Figs. 1b, 20; Tomurtogoo 2003, 2006, 2012; Kurihara et al. 2008; Bussien et al. 2011; Suzuki et al. 2012; Takeuchi et al. 2012; Hara et al. 2013; Nakane 2013; Purevjav et al. 2013; Ruppen et al. 2013; Tsukada et al. 2013). While, the Haraa terrane is largely composed of Lower Cambrian (?) metamorphosed clastic rocks and never includes radiolarian chert or oceanic island basalt (Fig. 20). The "geological division" is to identify the area having similar geologic characteristics (Tsukada et al. 2004). Although the Haraa terrane has been regarded as a northern constituent of the HD belt, the Haraa terrane has quite different lithology from the other terranes so is inappropriate to include it in the same geologic unit (Fig. 20).

On the other hand, the lithological and stratigraphical similarities between the rocks in the Haraa terrane and the terranes of the SB belt have been pointed out (e.g. Tomurtogoo et al. 1998; Parfenov et al. 2009). In the Haraa terrane, the Lower Cambrian (?) metamorphosed clastic rocks are intruded by Late Cambrian and Late Silurian granitic rocks and are unconformably overlain by Lower Devonian volcanic rocks and Lower Carboniferous clastic rocks. Similarly, the Proterozoic–Early Paleozoic metamorphosed clastic rocks are intruded by Neoproterozoic–Ordovician granitic rocks and are unconformably overlain by Middle–Late Paleozoic volcanic-clastic rocks in the SB belt (e.g. Ruzhentsev et al. 2006, 2007, 2012; Parfenov et al. 2009; Buslov et al. 2009; Ryabinin et al. 2011; Zhimulev et al. 2011; Buslov et al. 2013). Thus, the general Paleozoic stratigraphy of the Haraa terrane is substantially the same as that of the terranes of the SB belt. It seems reasonable to suppose that the Haraa terrane is excluded from the HD belt and is rather incorporated into the SB belt (Fig. 20). It is generally accepted that the SB belt was a

part of the “Siberian continent” during the Late Paleozoic (e.g. Parfenov et al. 2009; Donskaya et al. 2013, Petrov et al. 2014). Therefore, the rocks of the Haraa terrane may have composed a part of the SB belt during the Late Paleozoic.

2. Late Paleozoic relative position between the Haraa terrane and the Paleozoic accretionary complex of the Hangai-Daur belt

Having clarified the assignment of the Haraa terrane as part of a continent, the relative position between the Haraa terrane and the central part of the PAC of the HD belt in the Late Paleozoic will now be discussed in this section (Fig. 20). It is known that modal/chemical compositions and detrital zircon age distribution of sandstone are effective tools to estimate the geological environment of their provenance area. For instance, if the sandstones in the Haraa terrane and PAC have similar characteristics, they are presumed to have been formed in nearby areas which have the same provenance. Vice versa, if the characteristics of these sandstones are quite different, they have probably been formed in basins that are far from each other.

The youngest detrital zircon in the sandstones of the PAC of the Ulaanbaatar terrane has a U-Pb age of ca. 300 Ma (e.g. Hara et al. 2013), and the sandstones are unconformably overlain by a formation yielding Carboniferous bryozoans and brachiopods (Fig. 20; Minjin et al. 2006; Takeuchi et al. 2012). It was thus inferred from the detrital zircon and fossils that the sandstone of the PAC in the Ulaanbaatar terrane should be assigned to Carboniferous, while the Örmögtei Formation yields Visean bryozoans at its type locality (Ariunchimeg 1992, 2011). Therefore, these Carboniferous sandstones in the PAC of the Ulaanbaatar terrane and Örmögtei Formation of the Haraa terrane are compared in this study. In the Haraa terrane, detrital zircons of ca. 851–319 Ma with age peak of 349 Ma were reported from sandstone of the Örmögtei Formation in the Zaamar area, 150 km southwest of study area (Fig. 21a; Kelty et al. 2008). The sandstone of the Örmögtei Formation in the Züünharaa area have detrital zircons ranging from 1003 Ma to 321 Ma, with age peaks of 358 Ma and 363 Ma (Figs. 18a, b, 21b, c). Kelty et al. (2008), Hara et al.

(2013), and Ruppen et al. (2013) reported that the detrital zircons from Carboniferous sandstone in the PAC yield U-Pb ages of ca. 919–300 Ma with peak ages of 350–320 Ma (Figs. 21d, e, f). Thus, the age distribution of detrital zircon from the sandstones in both the Ulaanbaatar and Haraa terranes are very similar each other (Figs. 21a–f). This fact strongly suggests that the provenance area of these terranes had exposed rocks having nearly identical zircon age distributions.

The sandstones of the Carboniferous formations (e.g. Gorkhi Formation and Altan-Ovoo & Orgioch-Uul Formation) of the PAC in the Ulaanbaatar terrane are classified as feldspathic arenite, which are similar to those of the sandstones in the Örmögtei Formation (Fig. 22; e.g. Bussien et al. 2011; Suzuki et al. 2012; Hara et al. 2013; Nakane 2013; Ruppen et al. 2013). This fact is evidence that the provenance areas of these terranes had exposed the same type of rocks.

The Carboniferous sandstones of the Ulaanbaatar and Haraa terranes are also closely similar in chemical composition (Fig. 23a). In the UCC-normalized multi-element pattern, both sandstones of the Ulaanbaatar and Haraa terranes are enriched in Na_2O and depleted in MnO, MgO and CaO compared with a representative UCC composition. The chemical similarity between the Ulaanbaatar and Haraa terranes implies that the rocks exposed at the provenance areas of these terranes likely have the same chemical characteristics.

Bhatia (1983) proposed discriminant diagrams to identify the tectonic settings of sandstone. According to the definitions of Bhatia (1983) and Bhatia and Crook (1986), the “Continental Island Arc” represents sedimentary basins adjacent to island arcs on well-developed continental crust or on thin continental margins (e.g. Lau Basin, Sea of Japan, Cascades-Western USA); and the “Active Continental Margin” includes sedimentary basins of the Andean-type thick continental margin or crystalline basement (e.g. North Chile, Peru, South California borderland). In the diagrams, the data from the study area and the Ulaanbaatar terrane fall within the fields of “Continental Island Arc” and “Active Continental Margin” (Figs. 23b, c). This fact suggests that both sandstones were formed near an active continental margin.

It follows from what has been mentioned thus far that the Carboniferous sandstone of the Haraa terrane is quite similar to that of the Ulaanbaatar terrane in detrital zircon age distribution, modal composition and chemical composition. Additionally, chemical data suggests that the sedimentary basins of these sandstones were at/near an active continental margin. Therefore, it is reasonable to suppose that the Haraa and Ulaanbaatar terranes had been located close together at/near an active continental margin during Carboniferous (Figs. 20–23).

3. Timing of the low-angle southward-dipping thrusting in the Züünharaa area

The low-angle southward-dipping thrust in this area clearly cut the Haraa Group, the granitic rocks, and the Ulaan Öndör Formation (Fig. 3). The rocks of the Haraa Group are intruded by the granitic rocks and are covered by the Ulaan Öndör and Örmögtei Formations (Fig. 4). The equigranular granite has a U-Pb age of ca. 489 Ma and porphyritic granite-rhyolite has U-Pb ages of ca. 433–424 Ma (Figs. 17a–c, Table 1). The youngest magmatic zircon from the clast of porphyritic granite-rhyolite in the cataclasite of this thrust has an age of ca. 424 Ma (Figs. 16c, 17c). The type section of the Örmögtei Formation, 45 km north of the study area yields Visean bryozoans. These facts suggest that the low-angle south-dipping thrust occurred after the intrusion of the porphyritic granite-rhyolite and before the formation of the Örmögtei Formation. The thrusting can thus be considered to have occurred between the latest Silurian and Lower Carboniferous (Visean).

4. Distribution of the low-angle southward-dipping thrust

Several studies from other areas have reported low-angle faults, similar to the low-angle southward-dipping thrust of this study (L.2–L.4 in Fig. 24; e.g. Dejidmaa 2003; Kelty et al. 2008; Altanzul and Baasandolgor 2014). The metamorphosed sandstone of the Lower Cambrian (?) Haraa Group thrusts over Middle-Late Ordovician porphyritic rhyolite in the Zuunmod area, 30 km southeast of the Züünharaa area (Fig. 2a, L.2 in Fig. 23; Altanzul and Baasandolgor 2014). The thrust plane strikes N 20° E and gently dips southward (Altanzul and Baasandolgor 2014).

Dejidmaa (2003) reported sub-horizontal top-to-the northward fault cut volcanic rocks of the Lower Devonian Ulaan Öndör Formations in the Bayangol area, 40 km west of the study area (Fig. 2a, L.3 in Fig. 24). Kelty et al. (2008) suggested that the Lower Carboniferous Örmögtei Formation is exposed as a tectonic window below the Lower Cambrian (?) Haraa Group in the Zaamar area, 150 km southwest of the study area (L.4 in Fig. 24). Although details of the ages of the faults remains unknown, they were likely formed during the Late Paleozoic because it is generally hard to recognize low-angle faults in the Triassic/Jurassic granites throughout the Haraa terrane (Tomurtogoo et al. 1998, Tomurtogoo 2003).

Late Paleozoic low-angle southward-dipping thrusts are also recognized in the SB belt (L.5–L.7 in Fig. 24; e.g. Zorin 1999; Ruzhentsev et al. 2006, 2007, 2012; Buslov et al. 2009; Ryabinin et al. 2011; Zhimulev et al. 2011). Buslov et al. (2009) and Zhimulev et al. (2011) reported that the Neoproterozoic–Cambrian formations overthrust upon the Middle Ordovician Tunka granite and the Upper Devonian–Lower Carboniferous Sagan-Sair Formation with a plane trending E–W and dipping less than 30° southward in the Tunka area (L.5 in Fig. 24). Amphibole, biotite, and muscovite at the bottom of the tectonic sheet of the Neoproterozoic–Cambrian formations yield Ar-Ar ages of 316–303 Ma (Buslov et al. 2009; Ryabinin et al. 2011; Zhimulev et al. 2011). Ryabinin et al. (2011) and Zhimulev et al. (2011) interpreted these ages as the timing of the thrust.

Several examples of Late Paleozoic low-angle south-dipping thrusts can be seen in the Ul'zutui, Oldynda, and Kydzhimit areas of the Eravna terrane, SB belt (L.6 in Fig. 24). The andesite dated as ca. 310 Ma and felsite dated as ca. 297 Ma occur as a series of tectonic sheets alternating with slices of Lower Paleozoic rocks along low-angle south-dipping planes in the Ul'zutui, Oldynda, and Kydzhimit areas of the Eravna terrane (Ruzhentsev et al. 2012). Another example of Late Paleozoic thrust is found in the Bagdarin area of the Ikat terrane (L.7 in Fig. 24). The Neoproterozoic to Middle Paleozoic formation thrusts onto the Upper Devonian–Lower Carboniferous Bagdarin Formation along low-angle south-dipping planes in this area (Ruzhentsev

et al. 2007, 2012). The Usoi granitic rocks (ca. 288 Ma) of the Angara-Vitim batholith cut both the hanging-wall and footwall of the low-angle south-dipping thrust in the Bagdarin area (Ruzhentsev et al. 2007; Mazukabzov et al. 2010). It can thus be concluded that the thrusts in the Ul'zutui, Oldynda, Kydzhimit and Bagdarin areas (L.6, L.7 in Fig 24) were formed after the Early Carboniferous and before the Early Permian. The above observations make it clear that the Late Paleozoic low-angle southward-dipping thrust is widely recognized in both the HD and SB belts.

5. Tectonic implication of the low-angle southward-dipping thrust

Late Paleozoic low-angle southward-dipping thrusts are dominant in the Tunka, Ikat and Eravna terranes of the SB belt and the Haraa terrane (L.1–L.7 in Fig. 24). Also, several studies described contemporaneous southeast-verging composite folds and northward-dipping thrusts from the Asralt Hairhan and Ulaanbaatar terranes (L.8, L.9 in Fig. 24; e.g. Kurihara et al. 2008; Gordienko et al. 2012; Suzuki et al. 2012; Takeuchi et al. 2012). Takeuchi et al. (2012) revealed that the southeast-verging composite folds and northward-dipping thrusts are developed in the PAC of the Ulaanbaatar terrane (L.8 in Fig. 24). Northward-dipping thrusts are also recognized in the accretionary complex of the Asralt Hairhan terrane in the Tünhel area (Fig. 2a, L.9 in Fig. 24; Gordienko et al. 2012).

It is interpreted that the folds and thrusts in these terranes were formed in relation to northward subduction of the previous oceanic plate beneath the continental crust (e.g. Kurihara et al. 2008; Gordienko et al. 2012; Takeuchi et al. 2012; Ruppen et al. 2013). Kurihara et al. (2008) mentioned that the accretion process may have taken place from the latest Devonian to Early Carboniferous, and Hara et al. (2013) inferred, based on the U-Pb age of detrital zircon in the Ulaanbaatar terrane, that the accretion age of the clastic rocks is Early Carboniferous. Early Permian mafic to felsic dikes cut the folded Carboniferous clastic rocks in the PAC of the Ulaanbaatar terrane (Khishigsuren 2009). Hence, the southeast-verging folds and northward-dipping thrusts are considered to have been formed in the Early Carboniferous to Early Permian.

Simultaneously formed doubly-vergent (or bivergent) structures, similar to that in the HD and SB belt, have been illustrated in the Alps, the Andes, and in other locations (e.g. Willett et al. 1993; Storti et al. 2000; Naylor and Sinclair 2007; Mukherjee 2013b; Bose and Mukherjee 2015). For example, the Taranaki Fault in the northern part of New Zealand is considered to be a back thrust antithetic to the Hikurangi margin subduction thrusts. The Taranaki Fault has accommodated at least 12–15 km of dip-slip displacement since the middle Eocene (ca. 40–43 Ma) (e.g. Stern et al. 2006; Nicol et al. 2007; Stagpoole and Nicol 2008).

The doubly-verging character of the Eastern Alps architecture is evident from the predominant crisscross reflection pattern at ca. 10 km depth in a 150-220 km interval of a ca. 300 km seismic section (Gebrande et al. 2006), along which giant crustal wedges which have been upthrust since the Miocene (Pfiffner et al. 2000). The southward- and northward-dipping thrusts are exposed at the Inn Valley and the Valsugana-Agordo areas in the Eastern Alps, respectively (Slejko et al. 1989).

Another example can be seen in France and Spain. The doubly-vergent structure characterizes a ca. 150-km-wide surface expression with a central zone dominated by Hercynian basement flanked by fold-thrust belts, which shown by the 250-km-long deep seismic survey (ECORS Pyrenees profile; Choukroune 1989), from the Aquitaine basin to the Ebro basin of the Pyrenees (Sinclair et al. 2005). This structure is considered to have been formed in the Pyrenees as a result of northward subduction of the Iberian plate beneath the East European craton during the Late Cretaceous to early Miocene times (Roest and Srivastava 1991; Sinclair et al. 2005).

As shown in the above examples, the doubly-vergent structure is common in the plate convergence fields, i.e. subduction and collision zones. The oceanward-verging folds and thrusts are developed in accretionary complexes whereas the landward-verging thrusts are formed on the continental side under the Alpine-type compressional orogen such as the Alps and Himalaya (e.g. Beaumont et al. 1996; Poblet and Lisle 2011; Mukherjee et al. 2013). In the HD and SB belts, the

area of Late Paleozoic southeastwardly-verging composite folds and northward-dipping thrusts exposes PAC (e.g. Asralt Hairhan and Ulaanbaatar terranes; L.8, L.9 in Fig. 24); in contrast, the areas dominated by contemporaneous southward-dipping thrusts and folds are assigned to a part of the continental margin with Siberian craton (L.1–L.7 in Fig. 24).

It is considered that the southeastwardly-verging composite folds and northward-dipping thrusts in accretionary complex was attributed to the northward subduction of the Mongol-Okhotsk oceanic plate beneath the Siberian continent (Zorin 1999; Bussien et al. 2011; Gordienko et al. 2012; Takeuchi et al. 2012; Donskaya et al. 2013). The similarity of the Carboniferous sandstone in the Haraa terrane (continental affinity) and Ulaanbaatar terrane (accretionary complex) suggest that these terranes were closely placed areas during the Carboniferous, and this supports the above view (Figs. 20–23). The northward and southward-dipping thrusts are presently separated by the Late Mesozoic fault (Fig. 25). The Permian–Triassic volcanic-plutonic rock complexes in the north of the HD belt suggest subduction-related magmatic activity along the Paleozoic continental margin of the Siberian craton and the Permian adakitic rocks in the southern SB belt give concrete evidence to the northward subduction model (e.g. Morozumi 2003; Munkhtsengel et al. 2007; Donskaya et al. 2013; Nemekhbayar 2017). Thus, it seems reasonable to conclude that the doubly-vergent structure in the SB and HD belts (Fig. 25) was formed by the northward subduction of the Mongol–Okhotsk oceanic plate, which had been presented between SC and NCB/TB in the Late Paleozoic period (Fig. 1a).

Conclusion

- The Haraa terrane is composed largely of metamorphosed clastic rocks of the Haraa Group. The Haraa Group is intruded by Late Cambrian equigranular granite (ca. 489 Ma with an inherited age of ca. 541 Ma) and Late Silurian porphyritic granite-rhyolite (ca. 458–424 Ma with inherited ages of ca. 482 Ma and ca. 524 Ma), and unconformably covered by Lower Devonian volcanic rocks of the Ulaan Öndör Formation and Lower Carboniferous clastic rocks of the Örmögtei Formation in the Züünharaa area.
- Although the Haraa terrane has been assigned to the HD belt, which is mainly composed of Carboniferous accretionary complexes, it can rather be incorporated into the SB belt as a part of the continent from the view point of litho-stratigraphy.
- The detrital zircon age distribution and sandstone modal/chemical compositions of the Haraa and Ulaanbaatar terranes suggest that these terranes were located close together during the Carboniferous.
- Late Paleozoic low-angle southward-dipping thrust with a top-to-the northward sense of shear occurs in the Züünharaa area.
- The Late Paleozoic low-angle southward-dipping thrusts, similar to that in the Züünharaa area, are widely recognized in the Haraa terrane and SB belt, while the Late Paleozoic composite southward-dipping folds with northward-dipping thrust are dominant in the HD belt. The structural contrast of the SB belt + Haraa terrane (continental affinity) versus the HD belt (accretionary complex) corresponds to the doubly-vergent structure in the active continental margin, which was probably caused by the Late Paleozoic northward subduction of the Mongol–Okhotsk oceanic plate beneath the margin of the Siberian continent.

Acknowledgements

I would like to express my thanks to the Associate Professor Kazuhiro Tsukada for his helpful criticism of this thesis. Special thanks go to Mr. Oyunbold for helpful assist to carry out the field survey and sandstone sample preparations. I would also like to thank Professor Makoto Takeuchi, Professor Hidekazu Yoshida, Professor Yuhei Takahashi and Professor Koshi Yamamoto at Nagoya University for their insightful comments and discussion on this study. I am grateful to Mr. Setsuo Yogo and Ms. Masumi Nozaki at Nagoya University, Dr. Yuji Orihashi at University of Tokyo and Mr. Yoshiyuki Kouchi at University of Toyama, who gave access to the laboratory and research facilities and for their technical support. I wish to thank to the Mongolian Ministry of Education, Culture, Science, and Sports (MECSS) for the grant of the Educational Loan Fund (ELF); to Associate Prof. Munkhtsetseg Oidov, Dr. Sersmaa Gonchigdorj and Dr. Manchuk Nuramkhaan at Mongolian University of Science and Technology for valuable discussion and comments. I thank to the staffs and students of the Nagoya University Museum and Graduate School of Environmental Studies for supporting.

References

Altanzul, Ch., Baasandolgor, L., 2014. Gold mineralization feature and its origin in the Zuunmod district, Mongolia. Haiguulchin 50, 155–165 (in Mongolia).

Altanzul, Ch., Delgertsog, B., 2010. Structural features of the Gatsuurt gold deposit, Mongolia. Haiguulchin 46, 169–182 (in Mongolia).

Amantov, V.A., 1966. First finding of Lower Cambrian deposits in Eastern Mongolia. "In: Marinov N.A., (eds), Materials on the Geology of Mongolian People's Republic, Book I, Stratigraphy. Nedra press, Moscow, Russia, 13–20 (in Russian).

Ariunchimeg, Y., 2011. Carboniferous system. "In: Byamba, J., (eds.), Geology and Mineral Resource of Mongolia, Book I, Stratigraphy. Soyombo printing, Ulaanbaatar, 271–334 (in Mongolia).

Ariunchimeg, Y., 1992. New Paleozoic bryozoans of Mongolia. "In: Grunt T.A., (eds) New taxa of fossil invertebrates of Mongolia. The joint Russian-Mongolian paleontological expedition, Transactions 41. Nauka press, Moscow, Russia, 75–84 (in Russian).

Badarch, G., 2005. Tectonic overview of Mongolia. Mongolian Geoscientist 27, 1–7.

Badarch, G., Cunningham, W.D., Windley, B.F. 2002. A new terrane subdivision for Mongolia: implication for the Phanerozoic crustal growth of Central Asia. Journal of Asian Earth Science 21, 87–110.

Beaumont, C., Ellis, S., Hamilton, J., Fullsack, P., 1996. Mechanical model for subduction-collision tectonics of Alpine-type compressional orogens. Geology 24, 675–678.

Belichenko, V.G., Reznitskii, L.Z., Geletii, N.K., Barash, I.G., 2003. Tuva–Mongolia terrane (in the context of microcontinents in the Paleoasian ocean). Russian Geology and Geophysics 6, 531–541.

Bhatia, M.R., 1983. Plate tectonics and geochemical composition of sandstones. Journal of Geology 91, 611–627.

Bhatia, M.R., Crook, K.A.W., 1986. Trace elements characteristics of greywacke and tectonic setting discrimination of sedimentary basins. Contributions to Mineralogy and Petrology 92, 181–193.

Bobrov, V.A., Modzalevskya, E.A., 1964. New results of the Middle Devonian rocks in the Eastern Mongolia. Academy of Science, USSR, Report# 159 (4), 793–795 (in Russian).

Bose, N., Mukherjee, S., 2015. Back structures (back-faults and back-folds) from collisional orogen: field findings from Lesser Himalaya, Sikkim, India. 30th Himalaya-Karakoram-Tibet Workshop, Wadia Institute of Himalayan Geology, 06-08 Oct, Dehradun, India, 13–14.

Bulgatov, A.N., Gordienko, I.V., 1999. Terranes, synaccretionary, and postaccretionary complexes of the Transbaikalia and southeastern part of Eastern Sayn Regions, Siberia. "In: Nokleberg, W.J., Naumova, V.V., Kuzmin, M.I., Bounaeva, T.V., (eds.), Preliminary publications book 1 from project on mineral resources, metallogenesis, and tectonics of Northeast Asia U.S. Geological Survey Open-File Report 99-16, 1–9.

Bulgatov, A.N., Gordienko, I.V., 2014. Fold systems of the Sayan-Baikal mountain area. "In: Petrov, O.V., Leonov, Y.G., Pospelov, I.I., (eds.) Tectonics of Northern, Central and Eastern Asia. Explanatory Note to the Tectonic map of Northern–Central–Eastern Asia and Adjacent Areas at scale 1:2 500 000. –SPb.: VSEGEI Printing House, 53–58.

Buslov, M.M., Geng, H., Travin, A.V., Otgonbaatar, D., Kulikova, A.V., Chen Ming, Stijn, G., Semakov, N.N., Rubanova, E.S., Abildaeva, M.A., Voitishek, E.E., Trofimova, D.A., 2013. Tectonics and geodynamics of Gorny Altai and adjacent structures of the Altai–Sayan folded area. Russian Geology and Geophysics 54 (10), 1250–1271.

Buslov, M.M., Ryabinin, A.B., Zhimulev, F.I., Travin, A.V., 2009. Manifestations of the Late Carboniferous and Early Permian stages of formation of nappe–fold structures in the southern framework of the Siberian platform (East Sayany, South Siberia). Dokl. Earth Sci. 428 (7), 1105–1108.

Bussien, D., Gombojav, N., Winkler, W., Quadt, A., 2011. The Mongol-Okhotsk Belt in Mongolia - An appraisal of the geodynamic development by the study of sandstone provenance and detrital zircons. Tectonophysics 510, 132–150.

Byamba, B., Binderya, T., 1998. Geological sheet maps M-48-106-D, M-48-107-C; M-48-118-A, B at the scale of 1:50 000 with explanatory report. Geological Information Center, Mineral Resource Authority of Mongolia, Ulaanbaatar, Report #5029, 21–121 (in Mongolia).

Campe, A., Kraft, M., Pelihen, V., 1975. Geological sheet maps M-48-XXVIII, XXIX, XXXIII, XXXIV, XXXV, L-48-III, IV at the scale of 1:200 000 with explanatory report. Geological Information Center, Mineral Resource Authority of Mongolia, Ulaanbaatar, Report #2097, 1–171 (in Russian).

Choukroune, P., 1989. The ECORS Pyrenean deep seismic profile reflection data and the overall structure of an orogenic belt. Tectonics 8, 23–39.

Dejidmaa, G., 2003. Geological sheet map M-48-XXXIV at the scale of 1:200 000 with brief legend description. Geological Information Center, Mineral Resource Authority of Mongolia. Ulaanbaatar, Report #5565, 1–17 (in Mongolia).

Donskaya, T.V., Gladkochub, D.P., Mazukabzov, A.M., Ivanov, A.V., 2013. Late Paleozoic-Mesozoic subduction-related magmatism at the southern margin of the Siberian continent and the 150 million-year history of the Mongol-Okhotsk Ocean. Journal of Asian Earth Sciences 62, 79–97.

Gebrande, H., Lüschen, E., Bopp, M., Bleibinhaus, F., Lammerer, B., Oncken, O., Stiller, M., Kummerow, J., Kind, R., Millahn, K., Grassl, H., Neubauer, F., Bertelli, L., Borrini, D., Fantoni, R., Pessina, C., Sella, S., Castellarin, A., Nicolich, R., Mazzotti, A., Bernabini, M., 2006. First deep seismic reflection images of the Eastern Alps reveal giant crustal wedges and transcrustal ramps. Geophysical Research Letters 29 (10), doi: 10.1029/2006GL026618.

Gordienko, I.V., 2001. Geodynamic evolution of the Central-Asian and Mongol-Okhotsk fold belts and formation of the endogenic deposits. Geoscience Journal 5, 233–241.

Gordienko, I.V., Filimonov, A.V., Minina, O.R. 2007. The Dzhida island arc system in the Paleoasian Ocean: structure and main stages of Vendian–Paleozoic geodynamic evolution. Russian Geology and Geophysics 48 (1), 91–106.

Gordienko, I.V., Medvedev, A.Y., Gornova, M.A., Tomurtogoo, O., Goneger, T.A., 2012. The Haraa Gol terrane in the western Hentiyn Mountains (northern Mongolia): geochemistry, geochronology, and geodynamics. Russian Geology and Geophysics 53, 281–292.

Hara, H., Kurihara, T., Tsukada, K., Kon, Y., Uchino, T., Suzuki, T., Takeuchi, M., Nakane, Y., Nuramkhaan, M., Chuluun, M., 2013. Provenance and origins of a Late Paleozoic accretionary complex within the Khangai-Khentei belt in the Central Asian Orogenic Belt, central Mongolia. Journal of Southeast Asian Earth Sciences 75, 141–157. doi:10.1016/j.jseaes.2013.07.019

Hartmann, L.A., Leite, J.A.D., Silva, L.C., Remus, M.V.D., McNaughton, N.J., Groves, D.I., Fletcher, I.R., Santos, J.O.S., Vasconcellos, M.A.Z., 2000. Advances in SHRIMP geochronology and their impact on understanding the tectonic and metallogenic evolution of southern Brazil. Australian Journal of Earth Science 47, 829–844.

Hartmann, L.A., Santos J.O.S., 2004. Predominance of high Th/U, magmatic zircon in Brazilian shield sandstone. Geology 32, 73–76.

Henley, R.W., Ellis, A.J., 1983. Geothermal systems ancient and modern: a geochemical review. Earth-Sci.Rev. 19, 1–50.

Horn, I., Blanckenburg, F.V., 2007. Investigation on elemental and isotopic fractionation during 196 nm femtosecond laser ablation multiple collector inductively coupled plasma mass spectrometry. Spectrochimica Acta B62, 410–422.

Hou, W., Nie, F., Jiang, S., Bai, D., Liu, Y., Yun, F., Liu, Y., 2010. SHRIMP Zircon U-Pb Dating of Ore-bearing Granite in the Boroo Large-size Gold Deposit, Mongolia and Its Geological Significance. Acta Geoscientica Sinica 31 (3), 331–342. (in Chinese with English abstract). http://en.cnki.com.cn/Article_en/CJFDTotal-DQXB201003009.htm

Iwano, H., Oshihashi, Y., Hirata, T., 2013. An interlaboratory evaluation of OD-3 zircon for use as a secondary U–Pb dating standard. Island Arc 22, 382–394. doi:10.1111/iar.12038.

Jahn, B.M., Wu, F.Y., Chen, B., 2000a. Granitoids of the Central Asian Orogenic Belt and continental growth in the Phanerozoic. Transactions Royal Society of Edinburgh: Earth Sciences 91, 181–193.

Kelty, T., Yin, A., Dash, B., Gehrels, G.E., Ribeiro, A.E., 2008. Detrital-Zircon geochronology of Paleozoic sedimentary rocks in the Hangay-Hentey basin, north-central Mongolia: Implications for the tectonic evolution of the Mongol–Okhotsk Ocean in central Asia. Tectonophysics 451, 290–311.

Khishigsuren, S., Otoh, S., Munkhbat, B., Ohto, Y., 2009. New age data and tectonic setting of igneous rocks in the Ulaanbaatar area. Mongolian Geoscientist 35, 51–57.

Khulesh. A.A., Gorokhov V.A., 1961. Geological sheet map M-47-XXVIII at the scale of 1:200 000 with explanatory report. Geological Information Center, Mineral Resource Authority of Mongolia, Ulaanbaatar, Report #1510, 10–70 (in Russian).

Kotlyar, B., Drown, T., Tungalag, F., Gantsetseg, O., 1998. Two types of mineralization in the North Khentei gold tend. Mongolian Geoscientist 11, 10–13.

Kouchi, Y., Orihashi, Y., Obara, H., Fujimoto, T., Haruta, Y., Yamamoto, K., 2015. Zircon U–Pb dating by 213 nm Nd: YAG laser ablation inductively coupled plasma mass spectrometry: Optimization of the analytical condition to use NIST SRM 610 for Pb/U fractionation correction. Chikyukagaku (Geochemistry) 49, 19–35 (in Japanese with English abstract) doi:10.14934/chikyukagaku.49.19

Kovalenko, V.I., Yarmolyuk, V.V., Kovach, V.P., Kotov, A.B., Kozakov, I.K., Salnikova, E.B., Larin, A.M., 2004. Isotope provinces, mechanisms of generation and sources of the continental crust in the Central Asian mobile belt: geological and isotopic evidence. Journal of Asian Earth Sciences 23, 605–627.

Kröner, A., Windley, B.F., Badarch, G., Tomurtogoo, O., Hegner, E., Jahn, B.M., Gruschka, S., Khain, E.V., Demoux, A., Wingate, M.T.D., 2007. Accretionary growth and crust-formation in the Central Asian Orogenic Belt and comparison with the Arabian-Nubian shield. “In: Hatcher, Jr R.D., Carlson, M.P., McBride, J.H., Martínez Catalán, J.R., (eds.), the 4-D Framework of the Continental Crust. Geological Society of America Memoir 200, pp 181–209. doi:10.1130/2007.1200(11)

Kurihara, T., Tsukada, K., Otoh, S., Kashiwagi, K., Minjin, C., Dorjsuren, B., Bujinlkham, B., Sersmaa, G., Manchuk, N., Niwa, M., Tokiwa, T., Hikichi, G., Kozuka, T., 2008. Upper Silurian and Devonian pelagic deep-water radiolarian chert from the Khangai–Khentei belt of Central Mongolia: evidence for Middle Paleozoic subduction–accretion activity in the Central Asian Orogenic Belt. Journal of Asian Earth Sciences 34, 209–225.

Kurimoto, Ch., Tungalag, F., Bayarmandal, L., Ichinnorov, N., 1998. K-Ar ages of white micas from pelitic schists of the Bayanhongor area, west Mongolia. Bulletin of the Geological Survey of Japan 49 (1), 19–23.

Ludwig, K.R., 2012. User's Manual for Isoplot 3.75. A Geochronological Toolkit for Microsoft Excel. Berkeley Geochronology Center Special Publication No. 5, 1–75.

Mazukabsov, A.M., Donskaya, T.V., Gladkochub, D.P., Paderian, I.P., 2010. The Late Paleozoic geodynamics of the West Transbaikalian segment of the Central Asian fold belt. Russian Geology and Geophysics 51 (5), 482–491.

Minjin, Ch., Tomurtogoo, O., Dorjsuren, B., 2006. Devonian-Carboniferous accretionary complex of the Ulaanbaatar terrane. "In: Tomurhuu, D., Natal'in, B.A., Ariunchimeg, Y., Khishigsuren, S., Erdenesaikhan G., (eds.), Structural and Tectonic Correlation across the Central Asia Orogenic Collage: Implications for Continental Growth and Intracontinental Deformation (second international workshop and field excursions for IGC Project 480), abstract and excursion guidebook, Mongolian University of Science and Technology Press, Ulaanbaatar, 100–106.

Morozumi, H., 2003. Geochemical characteristics of granitoids of the Erdenet porphyry copper deposit, Mongolia. Resourse Geology 53, 311–316.

Mukherjee, S., 2013b. Higher Himalaya in the Bhagirathi section (NW Himalaya, India): its structures, backthrusts and extrusion mechanism by both channel flow and critical taper mechanisms. Int J Earth Sci (Geol Rundsch) 102 (7), 1851–1870. doi:10.1007/s00531-012-0861-5

Mukherjee, S., Mukherjee, B., Thiede, R., 2013. Geosciences of the Himalaya–Karakoram–Tibet orogen. Int J Earth Sci (Geol Rundsch) 102 (7), 1757–1758. doi:10.1007/s00531-013-0934-0

Munkhtsengel, B., Gerel, O., Tsuchiya, N., Ohara, M., 2007. Petrochemistry of igneous rocks in area of the Erdenetiin Ovoo porphyry Cu-Mo mineralized district, Northern Mongolia. "In: Tohji, K., Tsuchiya, N., Jeyadevan, B., (eds.), Water Dynamics: 4th International Workshop on Water Dynamics, Sendai, Japan, November 7-8, 2007, Proceedings: American Institute of Physics, 63–65.

Nakane, Y., 2013. MS. Geological division of the rocks at southeast of Ulaanbaatar (Gachuurt–Nalaikh), central Mongolia. Master thesis. Graduate School of Environmental Studies, Nagoya University.

Naylor, M., Sinclair, H.D., 2007. Punctuated thrust deformation in the context of doubly vergent thrust wedge: Implications for the localization of uplift and exhumation. Geology 35, 559–562.

Nicol, A., Mazengarb, C., Chanier, F., Rait, G., Uruski, C., Wallace, L., 2007. Tectonic evolution of the active Hikurangi subduction margin, New Zealand, since the Oligocene. Tectonics 26, TC4002, doi:10.1029/ 2006TC002090

Nemekhbayar, P., 2017. MS. Stratigraphy, structure, and geochemistry of Selenge complex in the Bulgan area, Mongolia. Master thesis. Graduate School of Environmental Studies, Nagoya University.

Obruchev., V.A., 1893. A few word about the geological structures of Eastern Mongolia along the expedition from Kyakhta to Kalgan. Imperial Russian Geographical Society, Irkutsk, News of Eastern Siberia, Notebook 24 (3-4), 104–108.

Okada, H., 1971. Classification of Sandstone: Analysis and Proposal. The Journal of Geology 79, 509–525.

Orihashi, Y., Nakai, S., Hirata, T., 2008. U-Pb age determination for seven standard zircons using Inductively Coupled Plasma-Mass Spectrometry Coupled with Frequency Quintupled Nd-

YAG (λ＝213 nm) Laser Ablation System: Comparison with LA-ICP-MS zircon analyses with a NIST glass reference material. Resource Geology 58, 101–123.

Parfenov, L.M., Khanchuk, A.I., Badarch, G., Berzin, N.A., Hwang, D.H., Miller, R.J., Naumova, V.V., Nokleberg, W.J., Ogasawara, M., Prokopiev, A.V., and Yan, H., 2004a. Generalized Northeast Asia geodynamics map. "In: Nokleberg, W.J., et al. (eds.), Digital files for Northeast Asia Geodynamics, Mineral Deposit Location, and Metallogenic Belt Maps, Stratigraphic Columns, Descriptions of Map Units, and Descriptions of Metallogenic Belts, US Geological Survey Open-File Report 2004-1252, CD-ROM, at scale 1:15 000 000

Parfenov, L.M., Badarch, G., Berzin, N.A., Berzin, N.A., Khanchuk, A.I., Kuzmin, M.I., Nokleberg, W.J., Prokopiev, A.V., Ogasawara, M., Yan, H., 2009. Summary of Northeast Asia geodynamics and tectonics. Stephan Mueller Spec Publ Ser 4, 11–33.

Passchier, C.W., Trouw, R.A.J., 1998. Micro-tectonics. Springer. Germany

Petrov, O.V., Pospelov, I.I., Shokalsky, S.P., 2014. Legend and tectonic zoning of Northern, Central and Eastern Asia (Central Asian fold belt and adjacent tectonic structures). "In: Petrov, O.V., Leonov, Y.G., Pospelov, I.I., Tectonics of Northern, Central and Eastern Asia. Explanatory Note to the Tectonic map of Northern–Central–Eastern Asia and Adjacent Areas at scale 1:2 500 000. – SPb.: VSEGEI Printing House, 18–32.

Pfiffner, O.A., Ellis, S., Beaumont, C., 2000. Collision tectonics in the Swiss Alps: Insight from geodynamic modelling, Tectonics 19, 1065–1094.

Poblet, J., Lisle, R.J., 2011. Kinematic Evolution and Structural Styles of Fold-and-Thrust Belts. Geological Society, London, Special Publications 349, 1–24. doi: 10.1144/SP349.1

Purevjav, N., Roser, B., 2013. Geochemistry of Silurian–Carboniferous sedimentary rocks of the Ulaanbaatar terrane, Hangay-Hentey belt, central Mongolia: Provenance, paleoweathering,

tectonic setting, and relationship with the neighbouring Tsetserleg terrane. Chemie de Erde 73 (4), 481–493. doi: 10.1016/j.chemer.2013.03.003

Purevsuren, B., Narantsetseg, O., 1998. Geological sheet maps M-48-105-C, D; M-48-106-C; M-48-117-A, B at the scale of 1:50 000 with explanatory report. Geological Information Center, Mineral Resource Authority of Mongolia, Ulaanbaatar, Report #5157, 12–44 (in Mongolia).

Riedel, W., 1929. Mechanics of rupture phenomenon. Central Journal for Mineralogy, Geology, and Paleontology B, 354–368 (in German)

Roest, W.R., Srivastava, S.P., 1991. Kinematics of the plate boundaries between Eurasia, Iberia and Africa in the North Atlantic from the late Cretaceous to the present. Geology 19, 613–616.

Rudnick, R.L., Gao, S., 2003. Composition of the Continental Crust. Treatise on Geochemistry 3, 1–64. doi.org/10.1016/B0-08-043751-6/03016-4

Ruppen, D., Knaf, A., Bussein, D., Winkler, W., Chimedtseren, A., Quadt, A., 2013. Restoring the Silurian to Carboniferous northern active continental margin of the Mongol-Okhotsk Ocean in Mongolia: Hangay-Hentey accretionary wedge and seamount collision. Gondwana Research 25 (4), 1517–1534.

Ruzhentsev, S.V., Minina, O.R., Nekrasov, G.E., Aristov, V.A., Golionko, B.G., Doronina, N.A., Lykhin, D.A., 2012. The Baikal–Vitim Fold System: Structure and Geodynamic Evolution. Geotectonics 46 (2), 87–110.

Ruzhentsev, S.V., Aristov, V.A., Minina, O.R., Golionko, B.G., Nekrasov, G.E., 2007. Hercynides of the Ikat-Bagdarin Zone in Transbaikalia. Dokl. Earth Sci. 417 (8), 1198–1201.

Ruzhentsev, S.V., Minina, O.R., Aristov, V.A., Katyukha, Y.P., 2006. Hercynian structural features in the West Transbaikalia region. Russian Journal of Earth Sciences 8, ES2001. doi:10.2205/2006ES000192

Ryabinin, A.B., Buslov, M.M., Zhimulev, F.I., Travin, A.V., 2011. The Late Paleozoic fold-thrust structure of the Tunka bald mountains, East Sayan (southern framing of the Siberian Platform). Russian Geology and Geophysics (Geologiya i Geofizika) 52 (12), 1605–1623.

Schönberg, T., Pasotti, M., 2016. Innstereo Documentation.

Sengör, A.M.C., Natal'in, B.A., Burtman, V.S., 1993. Evolution of the Altaid tectonic collage and Paleozoic crustal growth in Eurasia. Nature 364, 299–307.

Sengör, A.M.C., Natal'in, B.A., 1996. Turkin-type orogeny and its role in the making of the continental crust. Annual Review of Earth and Planetary Sciences 24, 263–337.

Sibson, R.H., 1983. Continental fault structure and the shallow earthquake source. Journal of Geological Society of London 140, 741–767.

Sinclair, H.D., Gibson, M., Naylor, M., Morris, R.G., 2005. Asymmetric growth of the Pyrenees revealed though measurement and modeling of orogenic fluxes. American Journal of Science 305, 369–406.

Slejko, D., Carulli, G.B., Nicolich, R., Rebez, A., Zanferrari, A., Cavallin, A., Doglioni, C., Carraro, F., Castaldini, D., Iliceto, V., Semenza, E., Zanolla, C., 1989. Seismotectonics of the eastern Southern Alps: A review, Bollettino di Geofisica Teorica ed Applicata 31 (122), 109–136.

Stacey, J.S., Kramers, J.D., 1975. Approximation of terrestrial lead isotope evolution by a 2-stage model. Earth and Planetary Science Letters 26 (2), 207–221.

Stagpoole, V., Nicol, A., 2008. Regional structure and kinematic history of a large subduction back thrust: Taranaki Fault, New Zealand. Journal of Geophysical research 113, B01403. doi:10.1029/2007JB005170

Stern, T.A., Stratford, W.R., Salmon, M.L., 2006. Subduction evolution and mantle dynamics at a continental margin: Central North Island, New Zealand. Reviews of Geophysics 44, RG4002. doi:10.1029/2005RG000171

Storti, F., Salvini, F., McClay, K., 2000. Synchronous and velocity-partitioned thrusting and thrust polarity reversal in experimentally produced, doubly-vergent thrust wedges: Implications for natural orogens. Tectonics 19 (2), 378–396. doi:10.1029/1998TC001079

Streckeisen, A.L., Le Bas, M.J., 1991. The IUGS systemic of igneous rocks. Journal of the Geological Society 148, 825–833.

Suzuki, T., Nakane, Y., Bakhat, N., Takeuchi, M., Tsukada, K., Sersmaa, G., Khishigsuren, S., Manchuk, N., 2012. Description of sandstones in the Ulaanbaatar area, Mongolia. Bulletin of the Nagoya University Museum 28, 27–38. http://www.num.nagoya-u.ac.jp/outline/report/pdf/028_03.pdf

Takebe, M., Yamamoto, K., 2003. Geochemical fractionation between porcellanite and host sediment. Journal of Geology 111, 301–312.

Takeuchi, M., Tsukada, K., Suzuki, T., Nakane, Y., Sersmaa, G., Manchuk, N., Kondo, T., Matsuzawa, N., Bakhat, N., Khishigsuren, S., Onon, G., Katsurada, Y., Hashimoto, M., Yamasaki, S., Matsumoto, A., Oyu-Erdene, B., Bulgantsengel, M., Kundyz, S., Enkhchimeg, L., Ganzoring, R., Myagmarsuren, G., Jamiyandagva, O., Molomjamts, M., 2012. Stratigraphy and geological structure of the Paleozoic system around Ulaanbaatar, Mongolia. Bulletin of the Nagoya University Museum 28, 1–18. doi:10.18999/bulnum.028.01

Tomur, S., Lhavgasuren, J., Gerelmaa, N., 1994. Geological sheet maps M-48-117-C, D; M-48-118-C, M-48-129-A, B, C, D; M-48-130-A at the scale of 1:50 000 with explanatory report. Geological Information Center, Mineral Resource Authority of Mongolia, Ulaanbaatar, Report #4859, 22–81 (in Mongolia).

Tomurtogoo, O., 2014. Tectonics of Mongolia. "In: Petrov, O.V., Leonov, Y.G., Pospelov, I.I., (eds.), Tectonics of Northern, Central and Eastern Asia. Explanatory Note to the Tectonic map of Northern–Central–Eastern Asia and Adjacent Areas at scale 1:2 500 000. –SPb.: VSEGEI Printing House, 110–126.

Tomurtogoo, O., 2012. Tectonic subdivision of Mongolian orogenic belts. Haiguulchin Journal 46, 20–35 (in Mongolia).

Tomurtogoo, O., 2006. Tectonic framework of Mongolia. "In: Tomurhuu, D., Natal'in, B.A., Ariunchimeg, Y., Khishigsuren, S., Erdenesaihan, G., (eds.), Structural and Tectonic Correlation across the Central Asian Orogenic Collage: Implications for Continental Growth and Intracontinental Deformation (second international workshop and field excursions for IGC Project 480), abstract and excursion guidebook, Mongolian University of Science and Technology Press, Ulaanbaatar, 18–20.

Tomurtogoo, O., 2003. Tectonic map of Mongolia at the scale of 1:1 000 000 and tectonics of Mongolia (brief explanatory notes of the map). Mineral Resources Authority of Mongolia, Ulaanbaatar

Tomurtogoo, O., Byamba, J., Badarch, G., Minjin, Ch., Orolmaa, D., Khosbayar, P., Chuluun, D., 1998. Geologic map of Mongolia at the scale of 1:1 000 000 and Summary (explanatory notes of the map). Mineral Resources Authority of Mongolia, Ulaanbaatar

Tolokonnikova, Z., Ernst, A., Wyse Jackson, P.N., 2014. Palaeobiogeography and diversification of Tournaisian–Viséan bryozoans (lower–middle Mississippian, Carboniferous) from

Eurasia. Palaeogeography, Palaeoclimatology, Palaeoecology 414, 200–211. doi:10.1016/j.palaeo.2014.08.023

Tovuudorj, D., 2003. Geological sheet map M-48-XXIX at the scale of 1:200 000 with brief legend description. Geological Information Center, Mineral Resource Authority of Mongolia. Ulaanbaatar, Report #5566, 1–66 (in Mongolia).

Tseden, Ts., Murao, S., Dorjgotov, D., 1992. Introduction of Geology of Mongolia. Bulletin of the Geological Survey of Japan 43 (12), 735–744. https://www.gsj.jp/data/bull-gsj/43-12_01.pdf

Tsukada, K., Nakane, Y., Yamamoto, K., Kurihara, T., Otoh, S., Kashiwagi, K., Minjin, Ch., Sersmaa, G., Manchuk, N., Niwa, M., Tokiwa, T., 2013. Geological setting of basaltic rocks in an accretionary complex, Khangai–Khentei belt, Mongolia. Island Arc 22, 227–241. https://www.gsj.jp/data/bull-gsj/43-12_01.pdf

Tsukada, K., Otoh, S., Kurihara, T., Bayambadash, D., Chuluun, M., Gochigdorj, S., Nuramkhaan, M., 2010. Structure of the eastern Khangai-Khentei belt, Mongolia. “In: 117th Annual Meeting of the Geological Society of Japan Abstract O-59. doi:10.14863/geosocabst.2010.0.124.0

Tsukada, K., Takeuchi, M., Kojima, S., 2004. Redefinition of the Hida Gaien belt. Journal of Geological Society of Japan 110, 640–658 (in Japanese).

Usov., M.A., 1916. Orography and geology of the Hentii mountain range in Mongolia. News of the geological committee 34, seperate print 297, 889–998 (in Russian).

Vernikovsky, V.A., Vernikovsky A.E., Kotov A.B., Sal’nikova E.B., Kovach V.P., 2003. Neoproterozoic accretionary and collisional events on the western margin of the Siberian craton: new geological and geochronological evidence from the Yenisey Ridge. Tectonophysics 375, 147–168.

Wiedenbeck, M., Alle, P., Corfu, F., Griffin, W.L., Meier, M., Oberili, F., Quadt, A.V., Roddick, J.C., Spiegel, W., 1995. Three natural zircon standards for U-Th-Pb, Lu-Hf, trace element and REE analyses. Geostandards Newsletter 19, 1–23.

Windley, B.F., Alexeiev, D., Xiao, W., Kröner, A., Badarch, G., 2007. Tectonic models for accretion of the Central Asian Orogenic Belt. Journal of the Geological Society of London 164, 31–47.

Willett, S., Beaumont, C., Fullsack, P., 1993. Mechanical model for the tectonics of doubly vergent compressional orogens. Geology 21, 371–374.

Woodcock, N.H., Mort, K., 2008. Classification of fault breccias and related fault rocks. Geol. Mag. 145 (3), 435–440. doi:10.1017/S0016756808004883

Xiao, W., Windley, B.F., Hao, J., Zhai, M., 2003. Accretion leading to collision and the Permian Solonker suture, Inner Mongolia, China: Termination of the central Asian orogenic belt. Tectonics 22 (6), 1069. doi:10.1029/2002TC001484

Yamamoto, K., Morishita, T., 1997. Preparation of standard composites for the trace element analysis by X-ray fluorescence. Journal of the Geological Society of Japan 103 (11), 1037–1045.

Zhimulev, F.I., Buslov, M.M., Glorie, S., De Grave, J., Fidler, M.A., Izmer, A., 2011. Relationship between the Ordovician and Carboniferous–Permian collisional events in the southeastern Tunka bald mountains, East Sayan (southwestern framing of the Siberian Platform). Russian Geology and Geophysics 52, 1634–1642.

Zhimulev, F.I., Safonova, I., Ryabinin, A., Buslov, M., 2010. An Early Proterozoic metamorphic basement of the Tuva–Mongolia microcontinent as a part of the Tunka fold–nappe terrane (South Siberia): constraints from U/Pb geochronology. EGU General Assembly

Conference Abstracts 12, 2285. ftp://ftp.gfz-potsdam.de/home/cegit/egu/pdf/EGU2010-2285.pdf

Zorin, Yu. A., (1999) Geodynamics of the western part of the Mongolia-Okhotsk collisional belt, Transbaikal region (Russia) and Mongolia. Tectonophysics 306, 33–56.

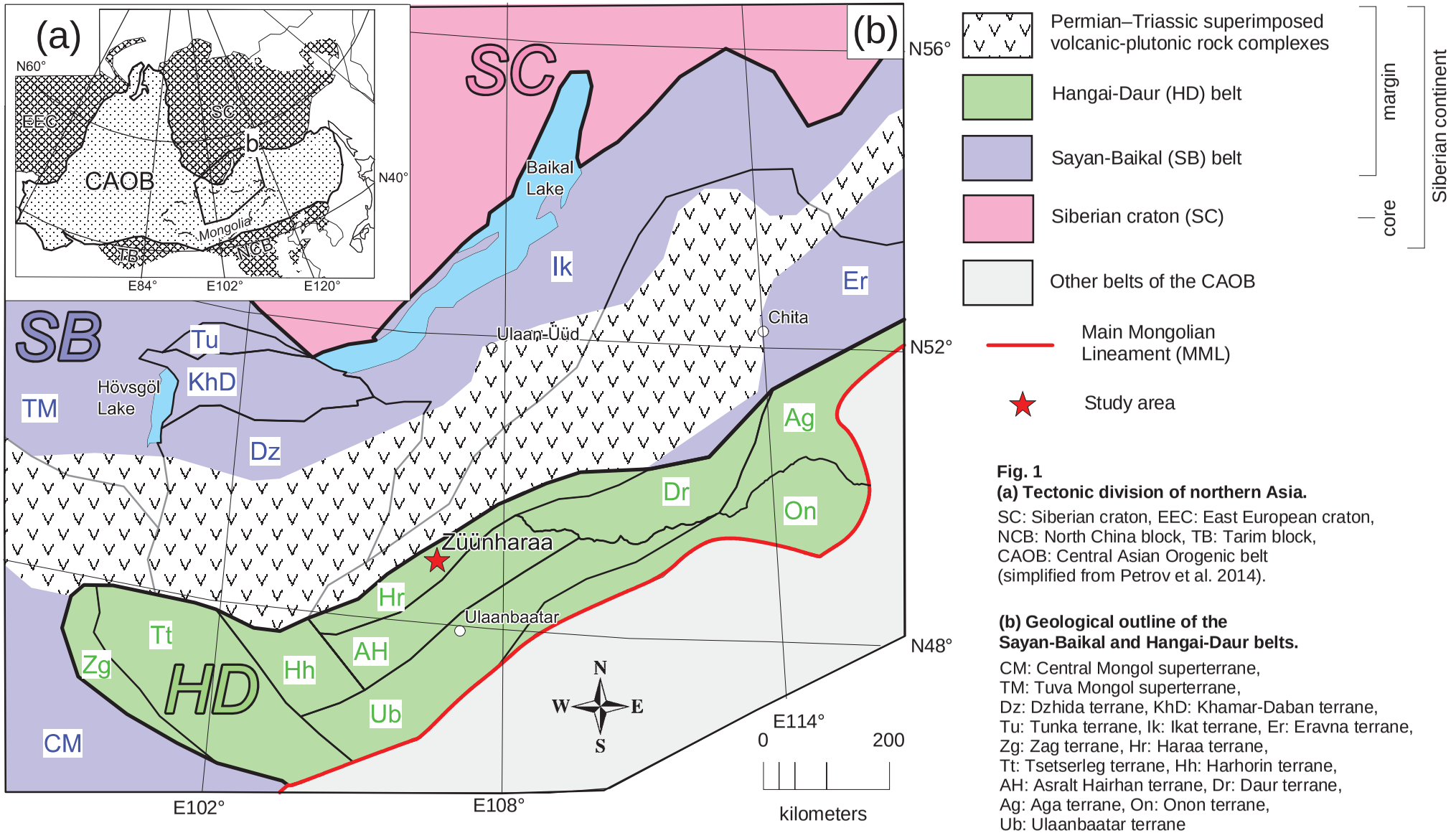

Fig. 1
(a) Tectonic division of northern Asia.

SC: Siberian craton, EEC: East European craton, NCB: North China block, TB: Tarim block, CAOB: Central Asian Orogenic belt (simplified from Petrov et al. 2014).

(b) Geological outline of the Sayan-Baikal and Hangai-Daur belts.

CM: Central Mongol superterrane,
TM: Tuva Mongol superterrane,
Dz: Dzhida terrane, KhD: Khamar-Daban terrane,
Tu: Tunka terrane, Ik: Ikat terrane, Er: Eravna terrane,
Zg: Zag terrane, Hr: Haraa terrane,
Tt: Tsetserleg terrane, Hh: Harhorin terrane,
AH: Asralt Hairhan terrane, Dr: Daur terrane,
Ag: Aga terrane, On: Onon terrane,
Ub: Ulaanbaatar terrane
(after Bulgatov and Gordienko 1999; Tomurtogoo 2012; Petrov et al. 2014).

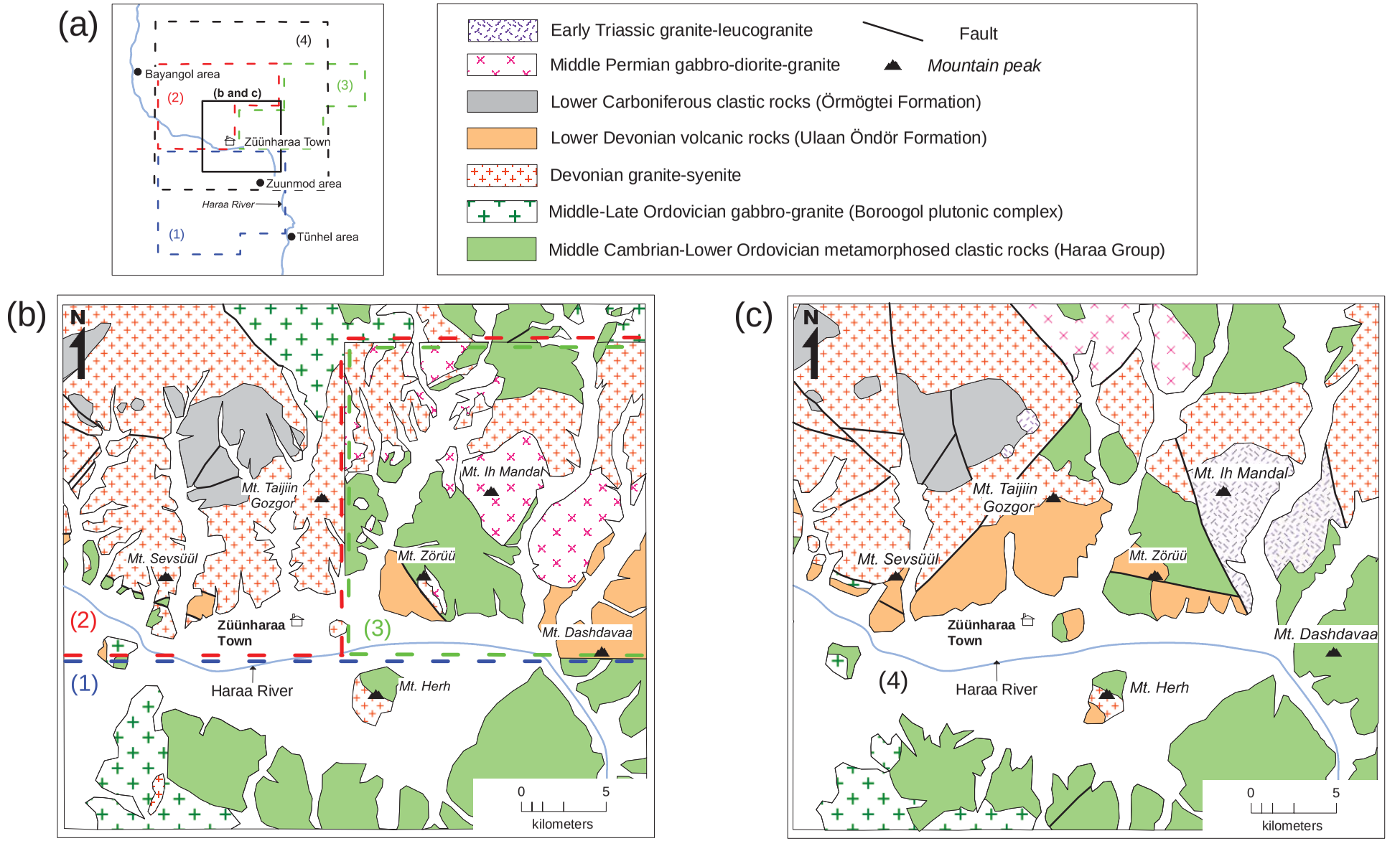

Fig. 2 (a) An index map of the previous geological maps published by (1) Tomur et al. (1994), (2) Purevsuren and Narantsetseg (1998) (3) Byamba and Binderya (1998) and (4) Tovuudorj et al. (2003). **(b) and (c)** Simplified previous geological maps.

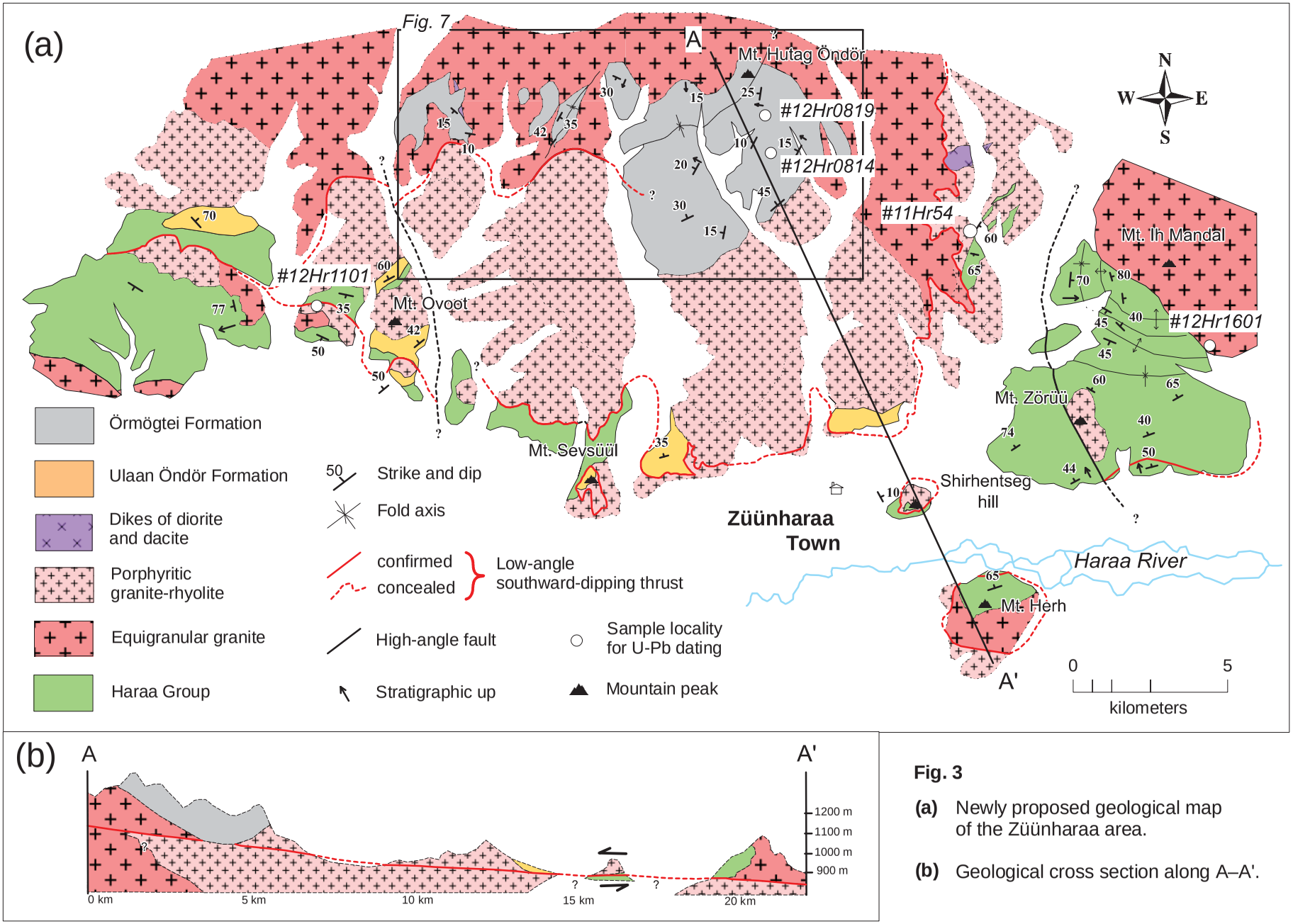

Fig. 3

(a) Newly proposed geological map of the Züünharaa area.

(b) Geological cross section along A–A'.

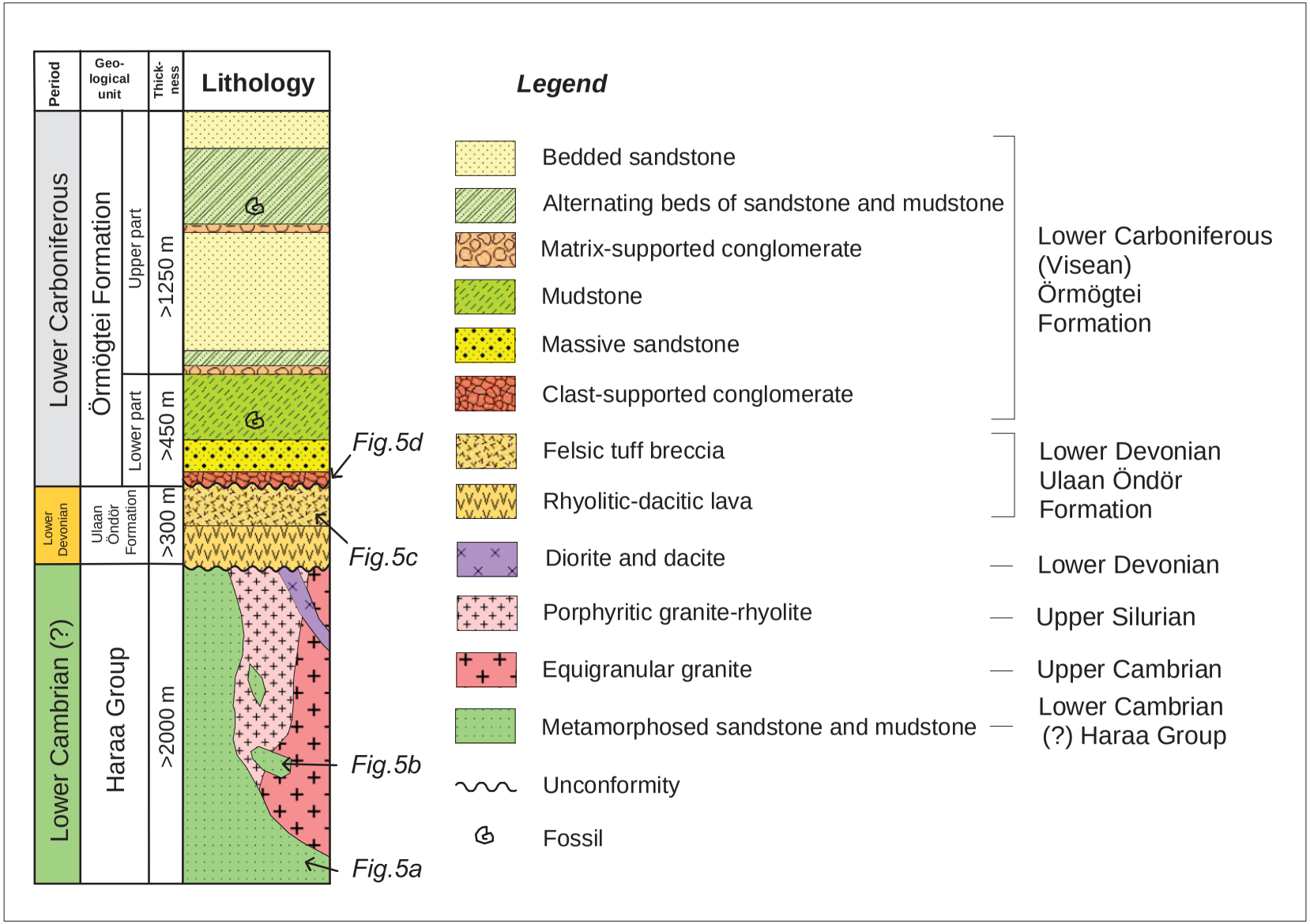

Fig. 4 General stratigraphy in the Züünharaa area.

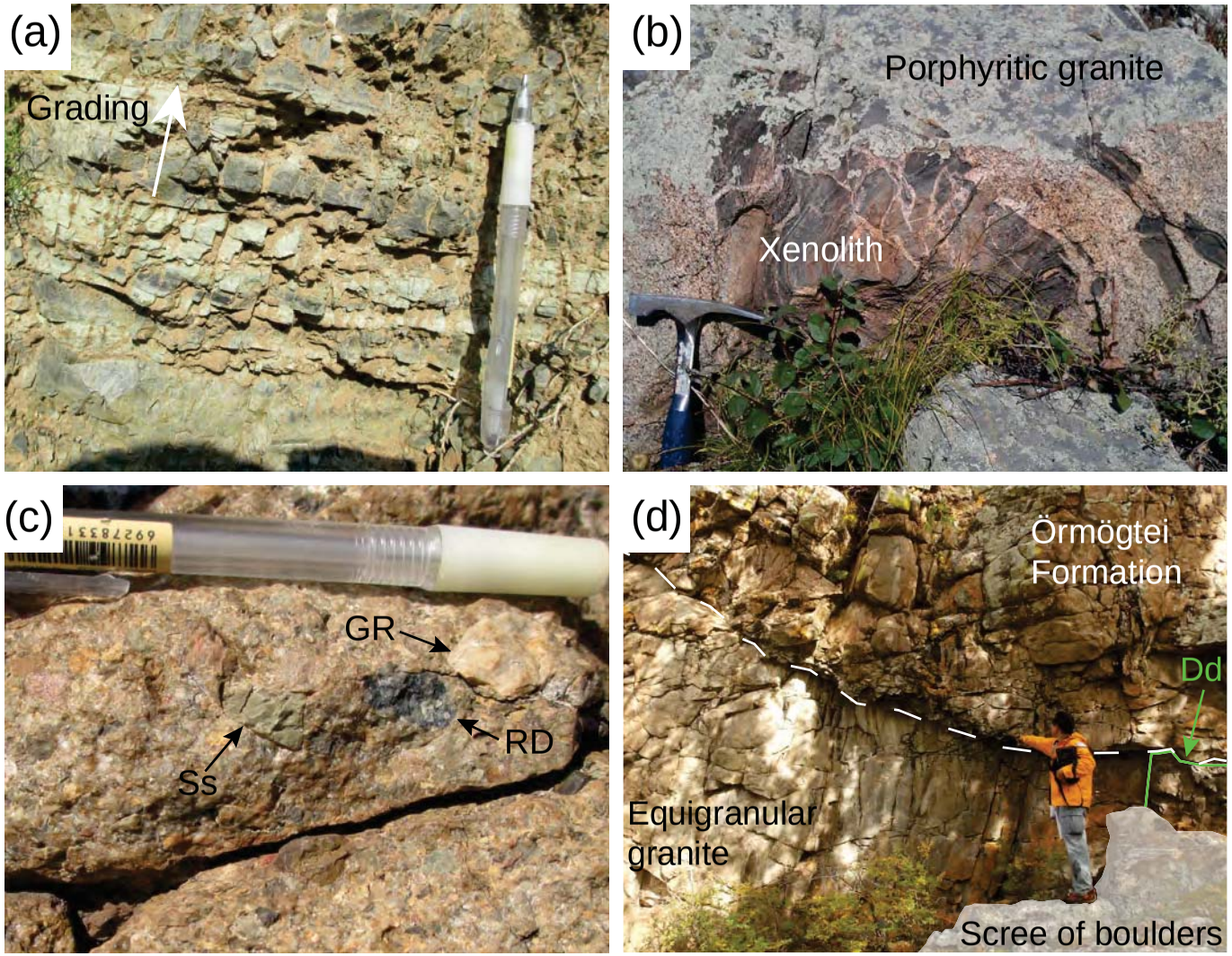

Fig. 5 Photographs showing the field occurence of the Haraa Group, Ulaan Öndör Formation, Örmögtei Formation and granitic rocks in the Züünharaa area. **(a)** Metamorphosed mudstone-sandstone of the Haraa Group showing graded bedding. White arrow shows stratigraphic up. **(b)** Xenolith derived from the Haraa Group in the porphyritic granite. **(c)** Felsic tuff breccia of the Ulaan Öndör Formation including angular to sub-rounded clasts of rhyolitic to dacitic lava (RD), porphyritic granite-rhyolite (GR), and metamorphosed sandstone (Ss). **(d)** Unconformity between the equigranular granite and Örmögtei Formation. Dacite dike (Dd) intrudes into the equigranular granite. Dashed line shows the boundary between equigranular granite and basal conglomerate of the Örmögtei Formation.

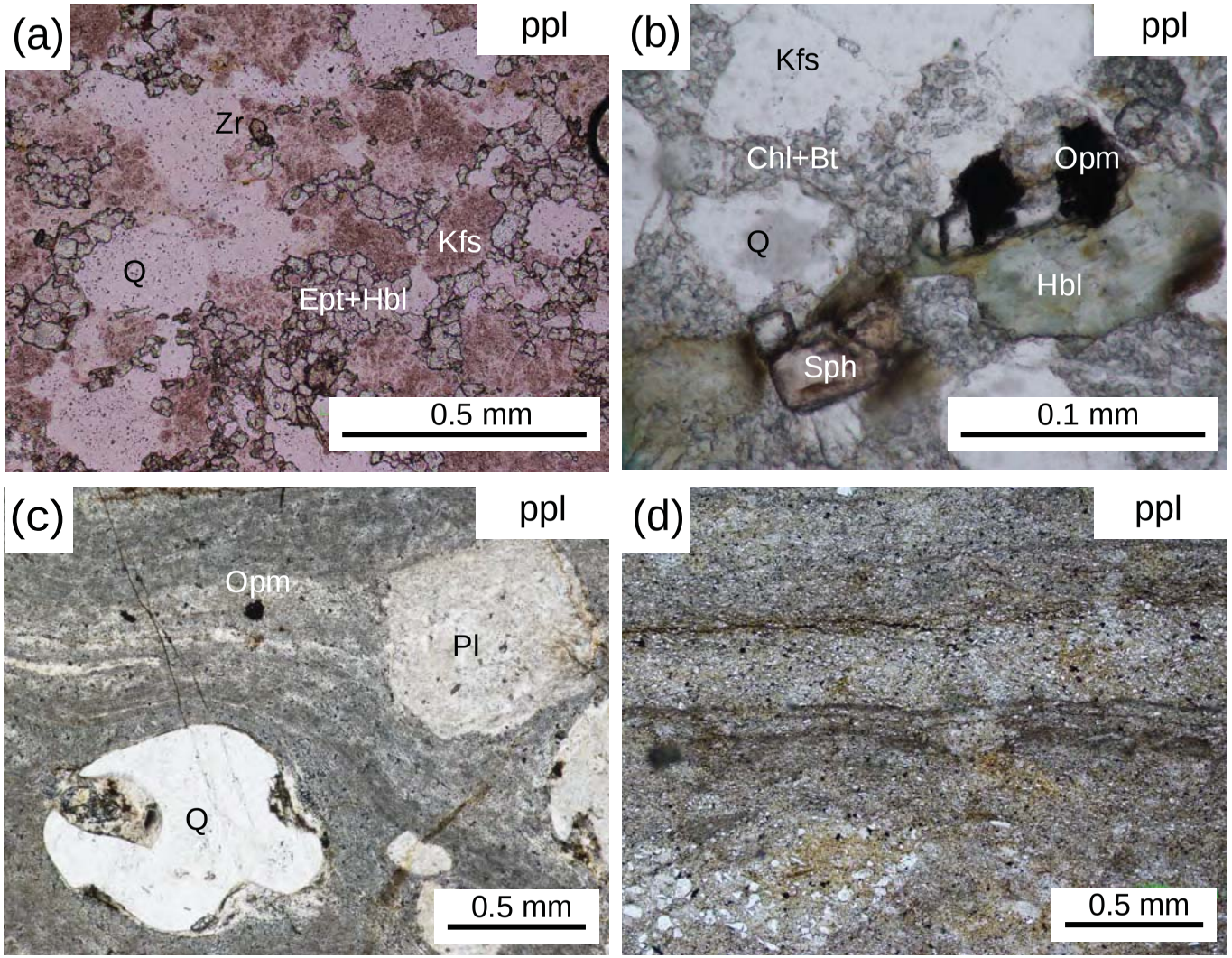

Fig. 6 Photomicrographs of the Haraa Group and Ulaan Öndör Formation in the Züünharaa area. (a) Metamorphosed sandstone from the Haraa Group. The rock includes abundant epidote and hornblende as metamorphic mineral. **(b)** Abundant chlorite and biotite in a finer matrix of the metarmorphosed sandstone suggests a later alteration. **(c)** Dacitic lava from the Ulaan Öndör Formation. The groundmass of the dacitic lava shows flow banding and includes phenocryst of plagioclase with amygdules infilled by quartz. **(d)** Fine-grained tuffaceous sandstone from the Ulaan Öndör Formation. Tuffaceous sandstone shows lamina and includes subangular felsic volcanic rock fragments, quartz, feldspar and opaque minerals in a finer matrix. Q: quartz, Kfs: K-feldspar, Pl: Plagioclase, Hbl: hornblende, Bt: biotite, Ep: epidote, Zr: zircon, Opm: opaque minerals, ppl: plane-polarized light.

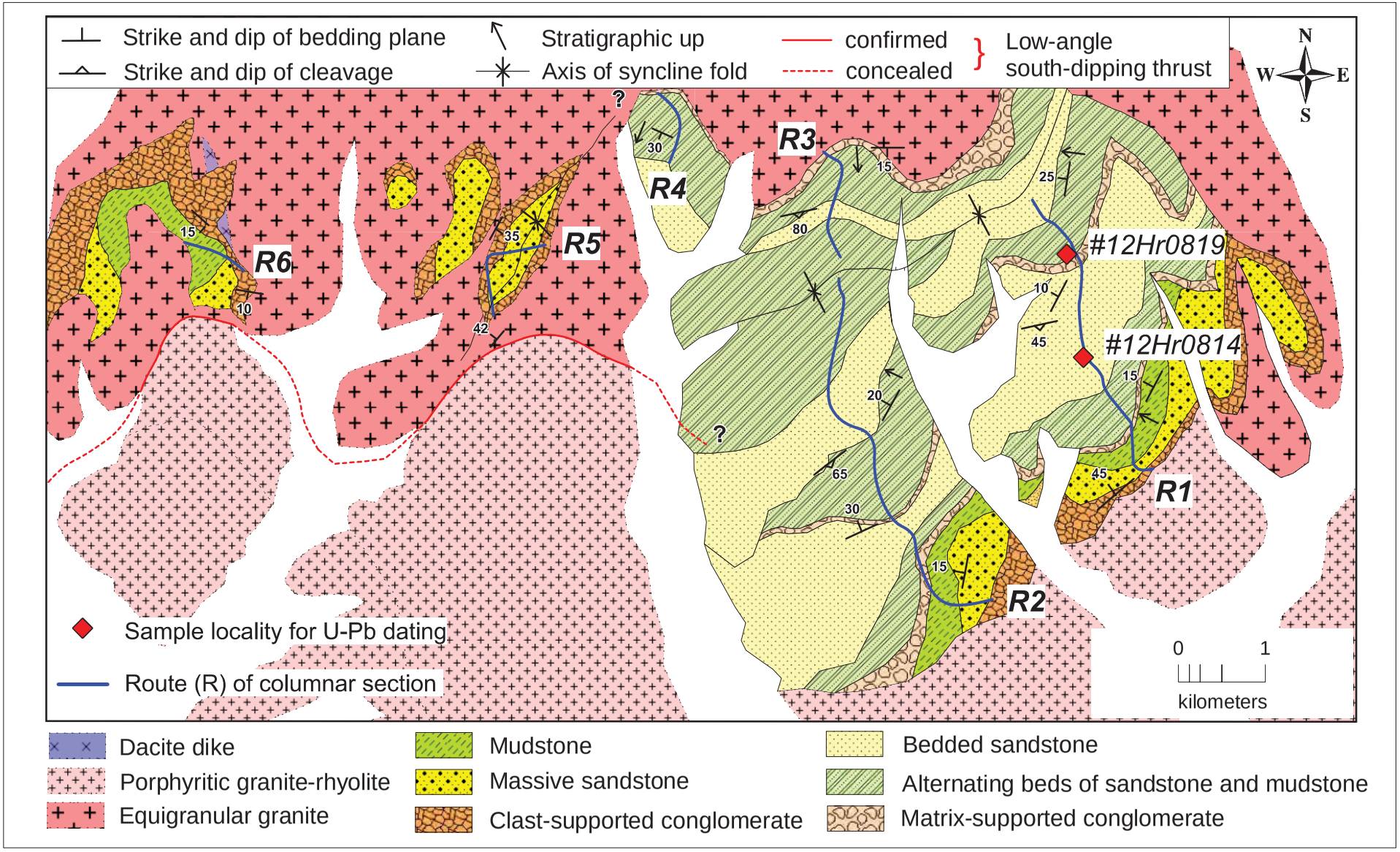

Fig. 7 Geological map of the northern part of the study area. See Fig. 3 for the locality.

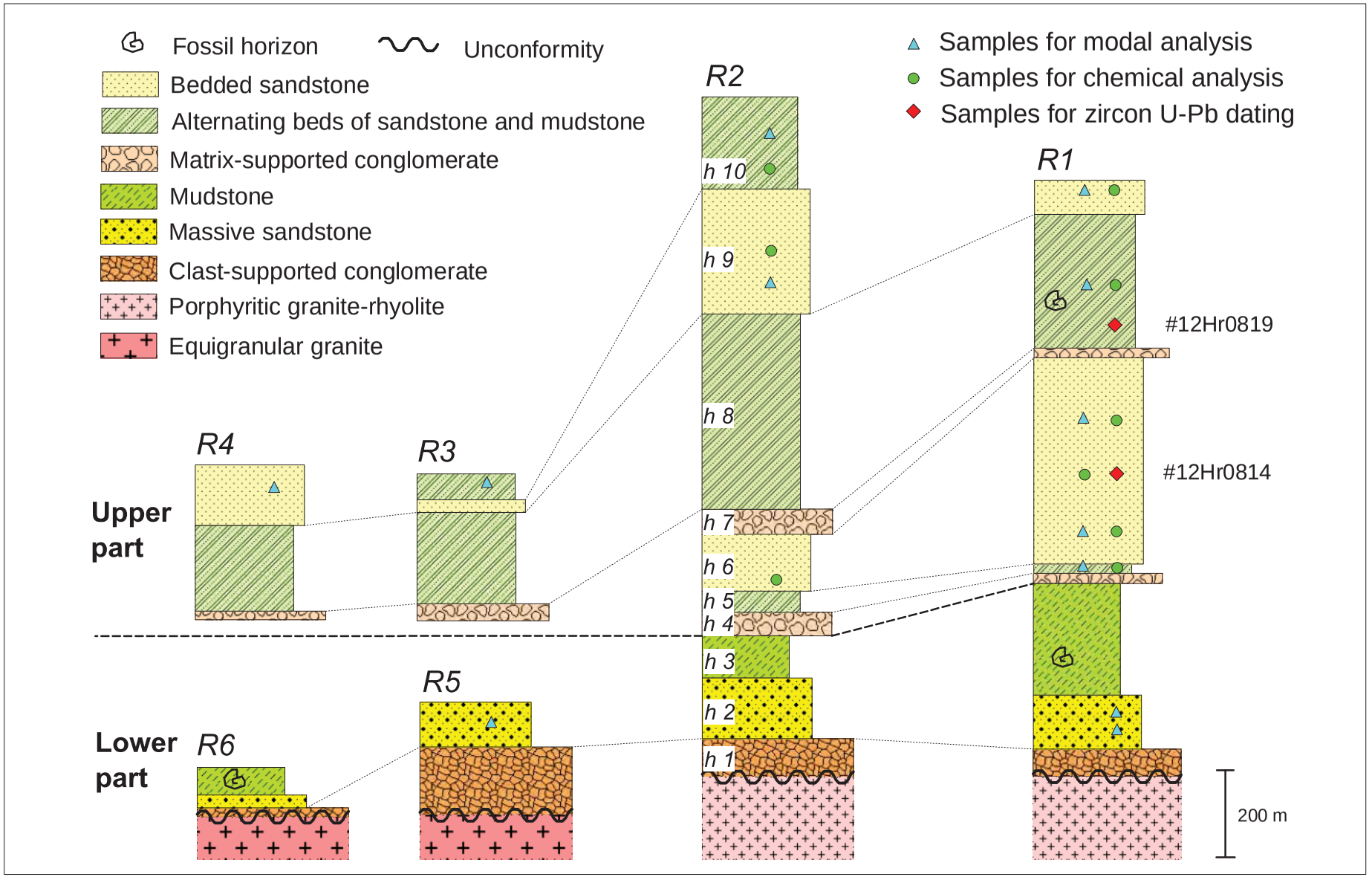

Fig. 8 Columnar sections of the Örmögtei Formation. See Fig. 7 for the locality of the columnar sections.

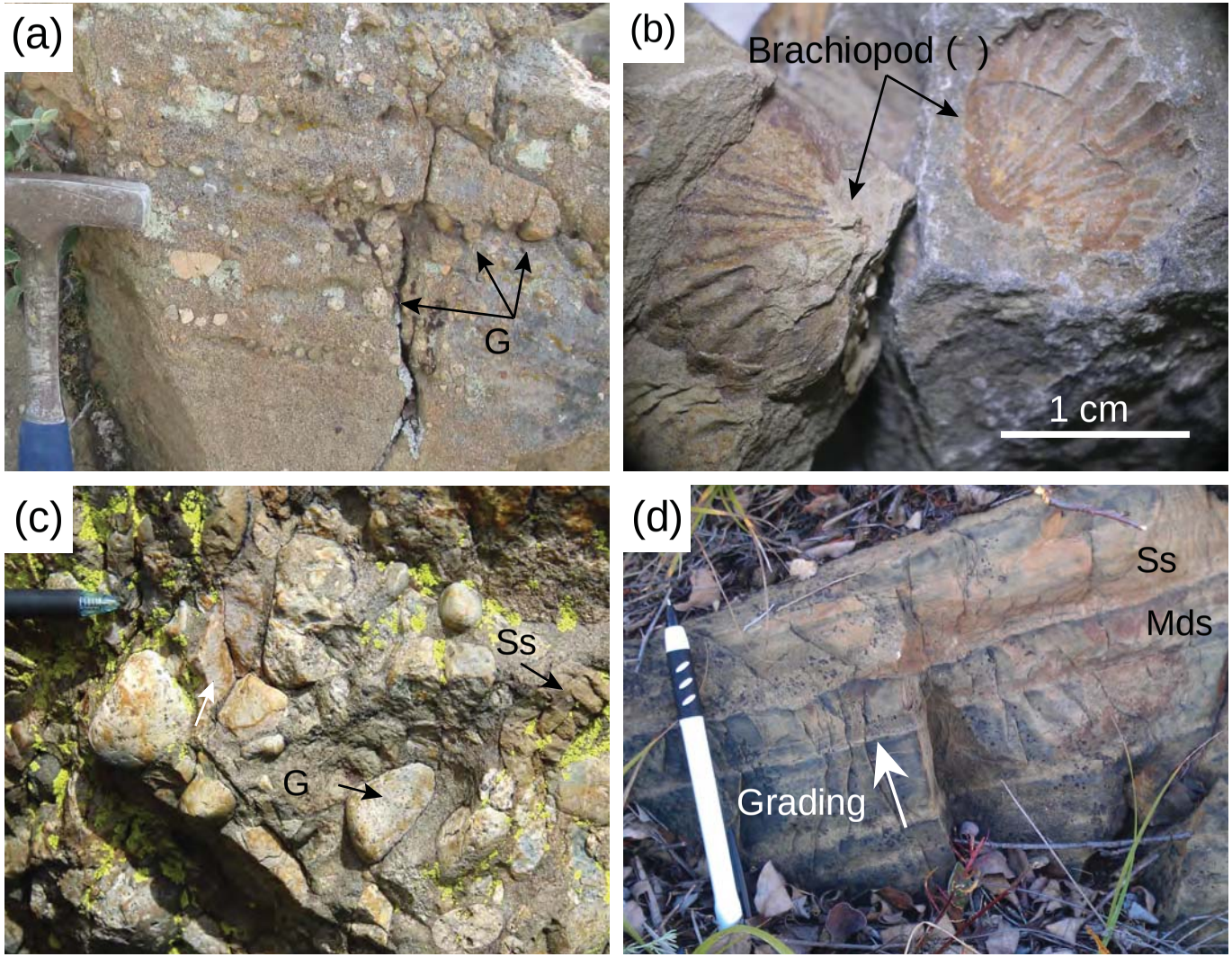

Fig. Field occurences of the Örmögtei Formation. (a) Massive sandstone of the ower part including abundant granule- to cobble-sized clasts of porphyritic granite-rhyolite (G) (h in Fig.). **(b)** mpression of the brachiopod ( ) fossil from the alternating beds of sandstone-mudstone of the Upper part (h and h in Fig.). **(c)** Matrix-supported conglomerate including rounded clasts of porphyritic granite-rhyolite (G) and sandstone (Ss) (h in Fig.). **(d)** Alternating beds of sandstone (Ss) and mudstone (Mds) showing graded bedding (h in Fig.). hite arrow shows stratigraphic up.

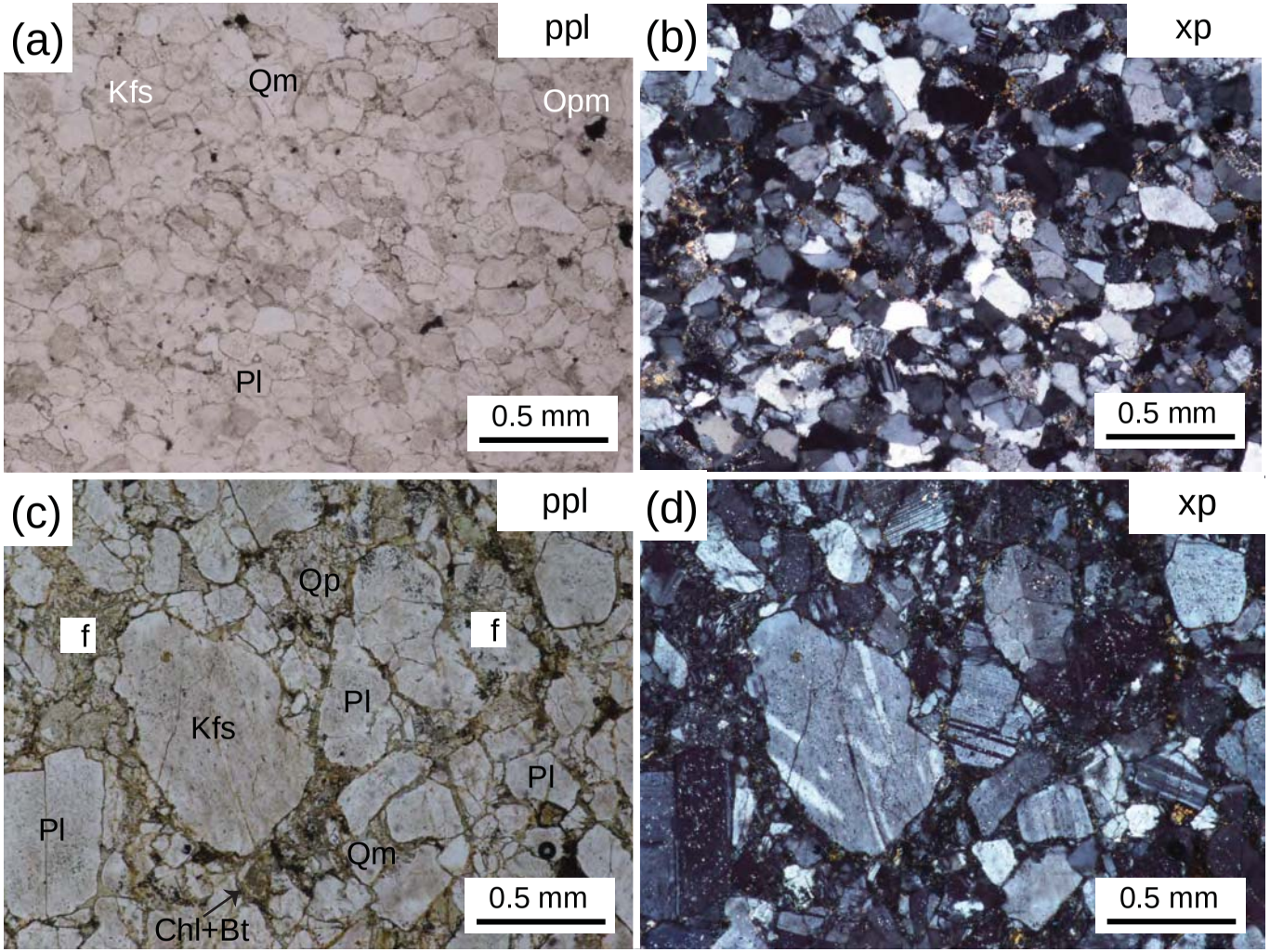

Fig. Photomicrographs of the sandstones of the Örmögtei Formation. (a) and **(b)** Massive sandstone from the horizon h including abundant grains of quartz and feldspar. **(c)** and **(d)** Bedded sandstone from the horizon h including abundant grains of feldspar and volcanic rock fragments in a finer matrix. Qm: monocrystalline quartz, Qp: polycrystalline quartz, Kfs: K-feldspar, Pl: plagioclase, Chl: chlorite, Bt: biotite, Zr: zircon, Opm: opaque minerals, f: lithic fragment, ppl: plane-polarized light, xp: crossed polar.

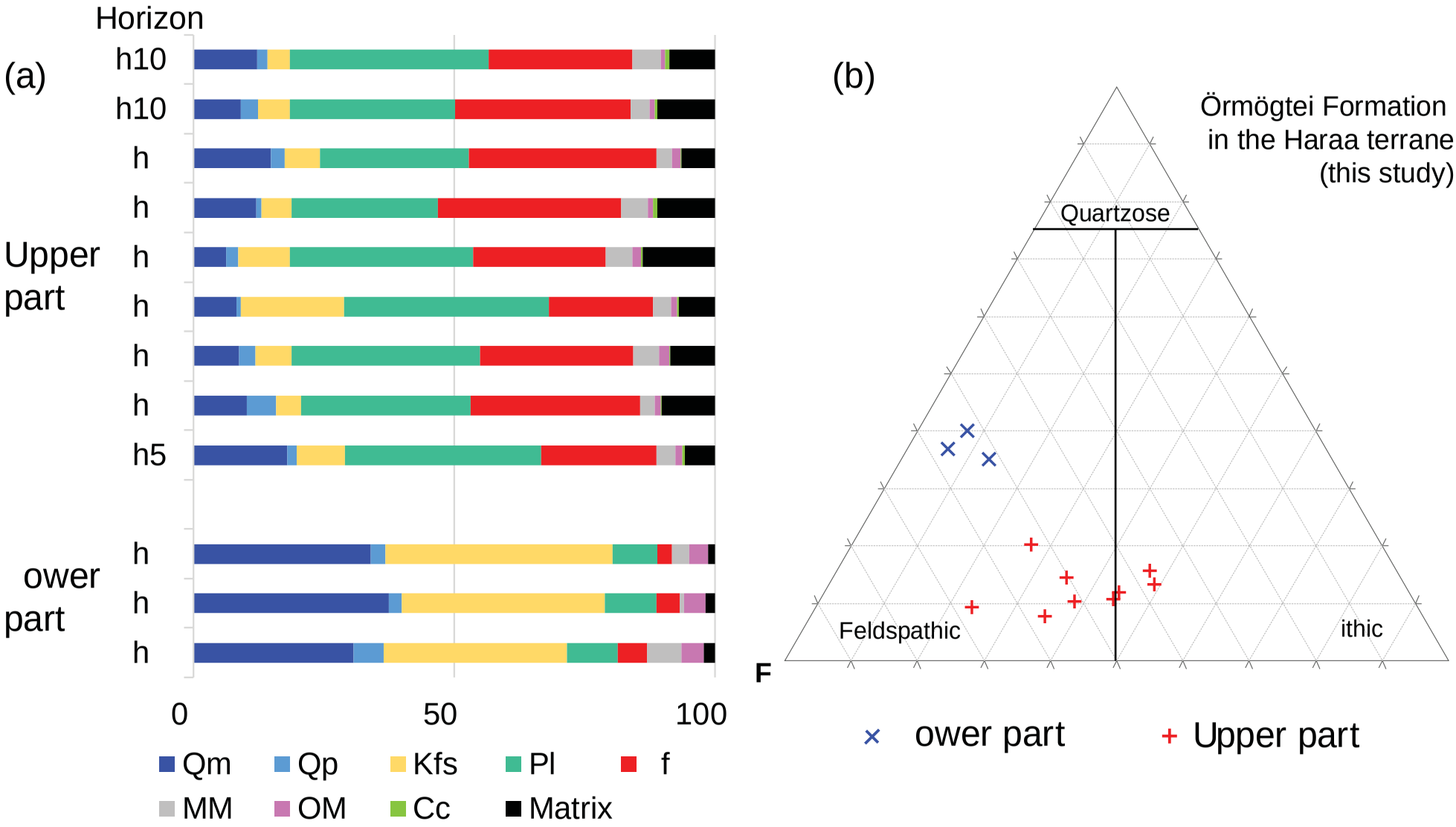

Fig. **(a)** Modal composition of sandtones from the Örmögtei Formation. See Fig. for the sample horizons. Qm: monocrystalline quartz, Qp: polycrystalline quartz, Kfs: K-feldspar, Pl: plagioclase, f: lithic fragments, MM: mica minerals, OM: other minerals such as chlorite, sphene, zircon, apatite and opaque minerals, Cc: calcareous cement. **(b)** Petrographic classification of sandstones from the Örmögtei Formation by Q-F- diagram (Okada 1 1)**.** Q: monocrystalline quartz, F: K-feldspar + plagioclase, : lithic fragments + polycrystalline quartz.

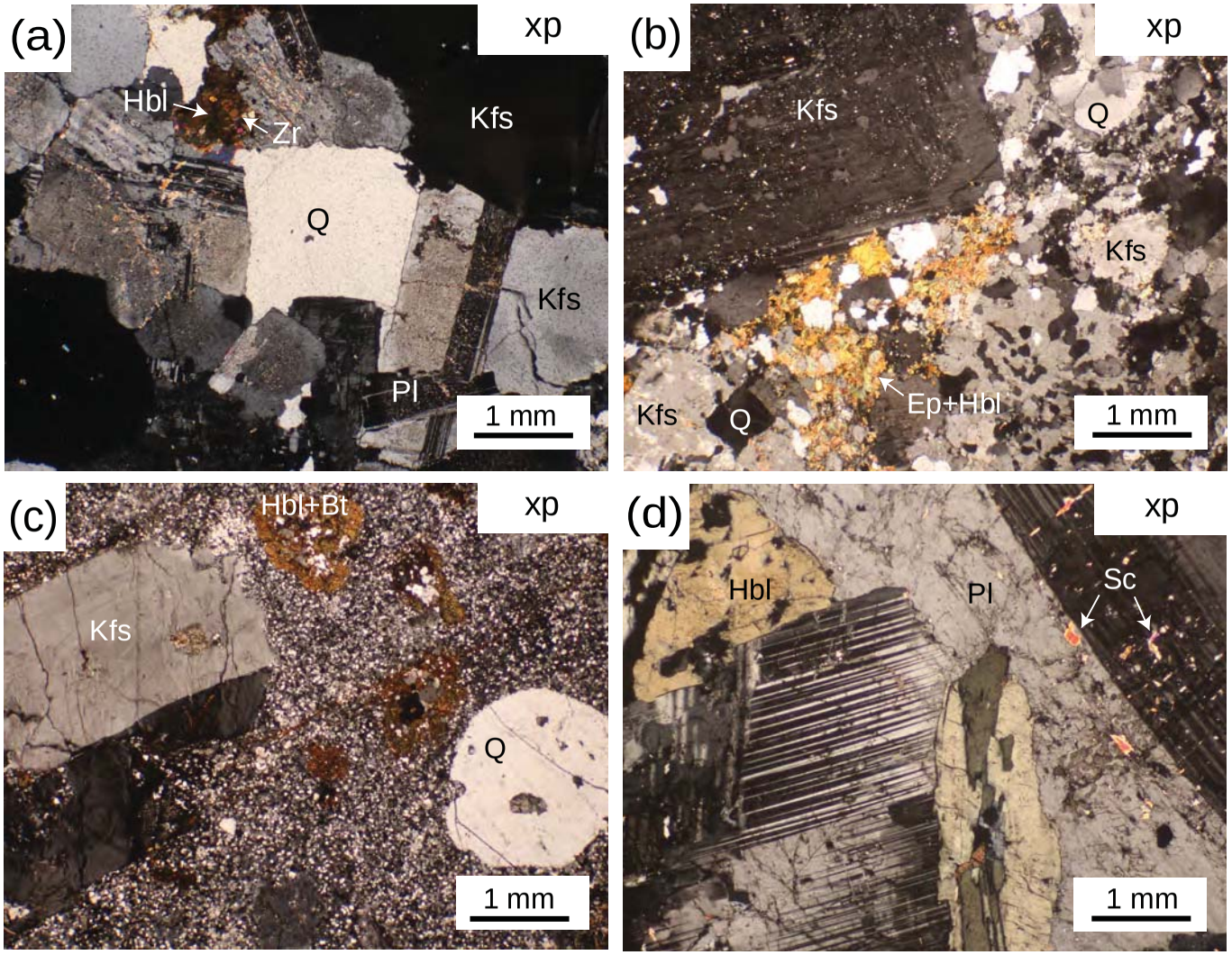

Fig. Photomicrographs of the granitic roc s and diorite di e in the Züünharaa area. (a) Equigranular granite composed of quartz, K-feldspar and plagioclase. Minor amounts of hornblende, biotite, apatite, zircon and opaque minerals are also included. **(b)** Porphyritic granite. Quartz, K-feldspar and plagioclase are embedded in a finer groundmass. **(c)** Porphyritic rhyolite including clots of hornblende and biotite up to 1 mm in size. The rock includes abundant quartz and K-feldspar phenocrysts. **(d)** Dike of diorite composed of plagioclase and hornblende. Q: quartz, Kfs: K-feldspar, Pl: plagioclase, Hbl: hornblende, Bt: biotite, Zr: zircon, Sc: sericite, Ep: epidote, xp: crossed polar.

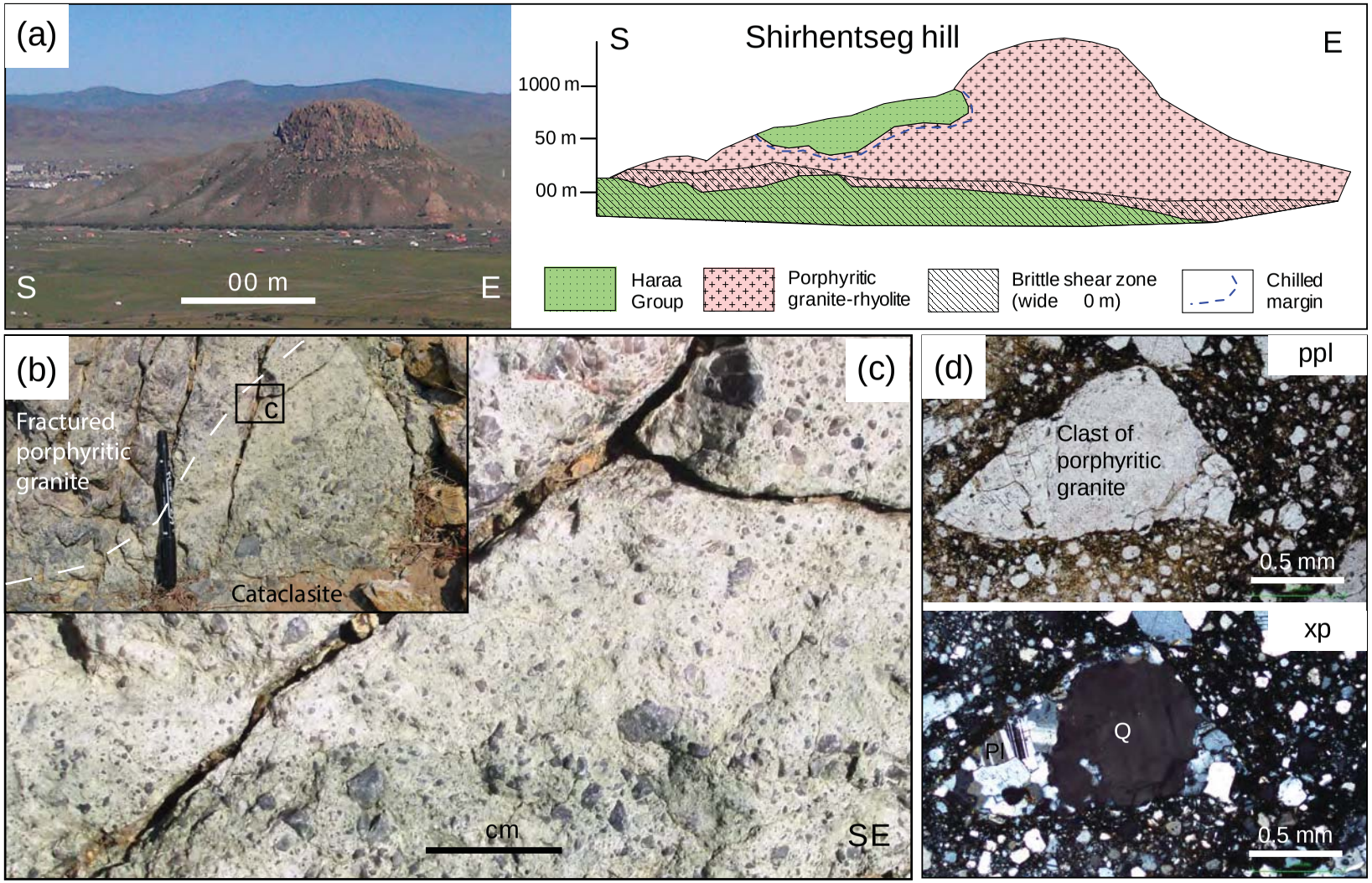

Fig. ode of occurrence of cataclasite in and around the lo angle south ard dipping thrust. (a) Overview of the Shirhentseg hill and its sketch. The porphyritic granite-rhyolite overthrusts onto the Haraa Group to form brittle shear zone up to ca. 0 m wide. **(b)** Field occurrence of the brittle shear zone. The rocks were intensely fractured, and form cataclasite bands in some places. **(c)** Close up view of the cataclasite in Fig. 1 b. Angular clasts derived from porphyritic granite are scattered in a clayey matrix to show random fabric. **(d)** Photomicrographs showing a clast of cataclasite derived from porphyritic granite. Q: quartz, Pl: plagioclase, ppl: plane-polarized light, xp: crossed polar.

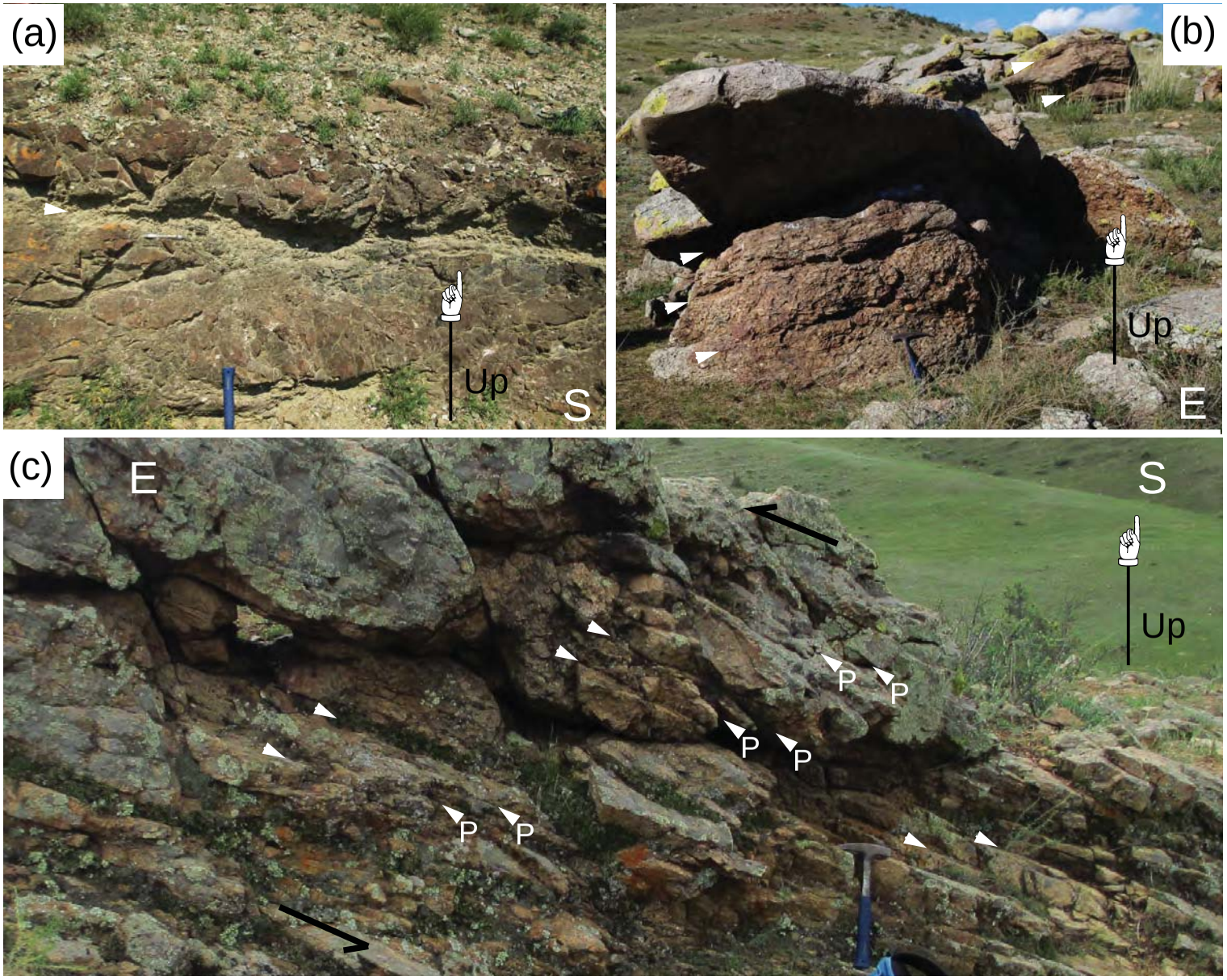

Fig. Photographs sho ing the field occurrence of foliated cataclasites.

(a) Photograph of sheared metamorphosed sandstone of the Haraa Group with sub-horizontal -shear (white arrow).

(b) Foliated cataclasite derived from tuff breccia of the Ulaan Öndör Formation with sub-horizontal -shears.

(c) Photograph of the foliated cataclasite derived from porphyritic granite-rhyolite. P- fabric (white arrows) indicates top-to-the northward sense of shear (black arrows).

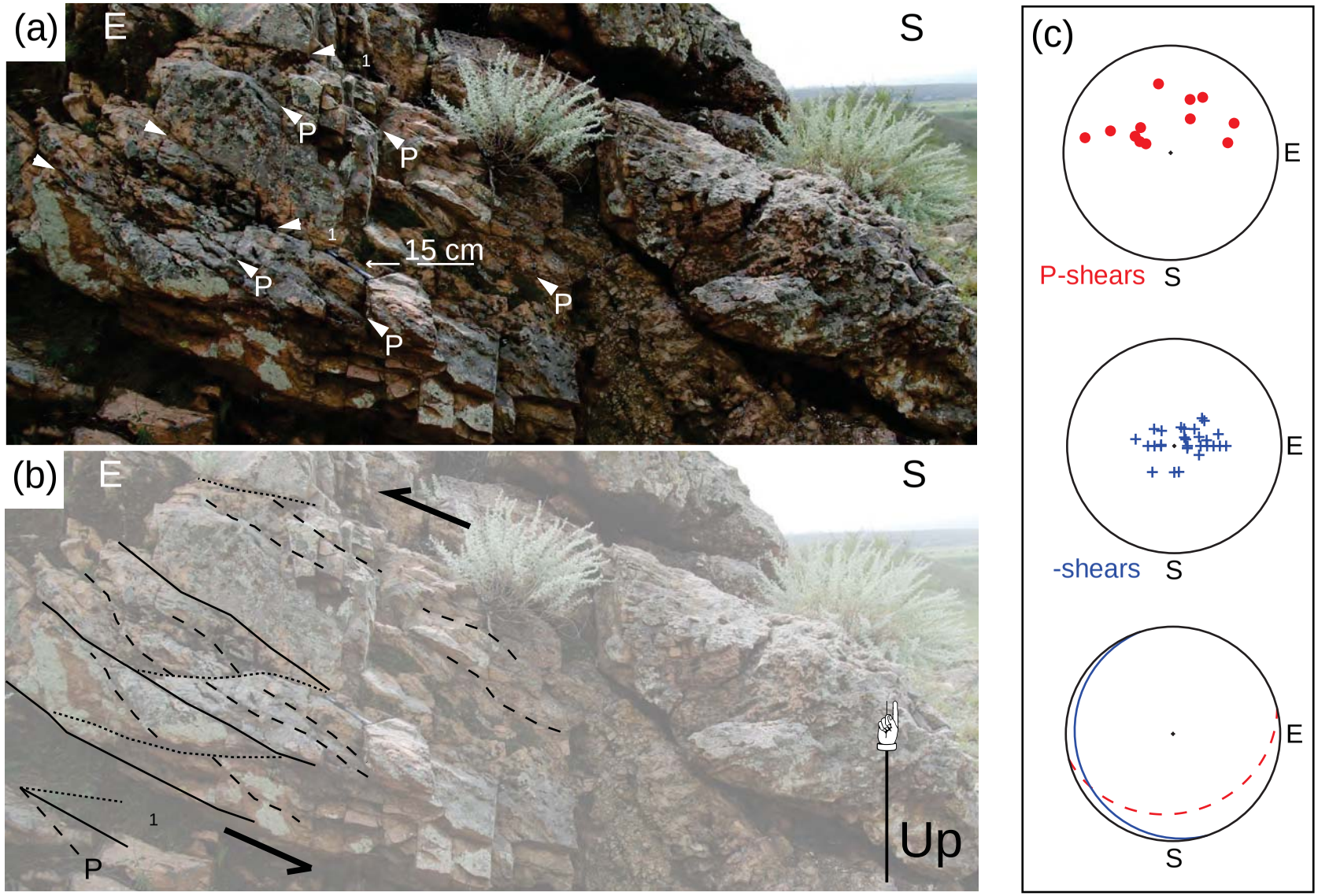

Fig. **(a)** Photograph of the foliated cataclasite derived from porphyritic granite-rhyolite show iedel shears (white arrows). A pen denotes 15 cm. **(b)** A sketch of $_1$-, P- and -shears of Fig. 1 a. $_1$ shear is terminated by -shear and terminates P-shear. P- fabric suggests top-to-the northward sense of shear (black arrows). **(c)** Equal-area lower hemisphere pro ections of P- and -shears in the study area. The great blue circle (solid) is the average plane of -fabric and the great red circle (dashed) is the average plane of P-fabric. P-shears trend to E and dip to S, while, -shears show subhorizontal planes with gentle dips.

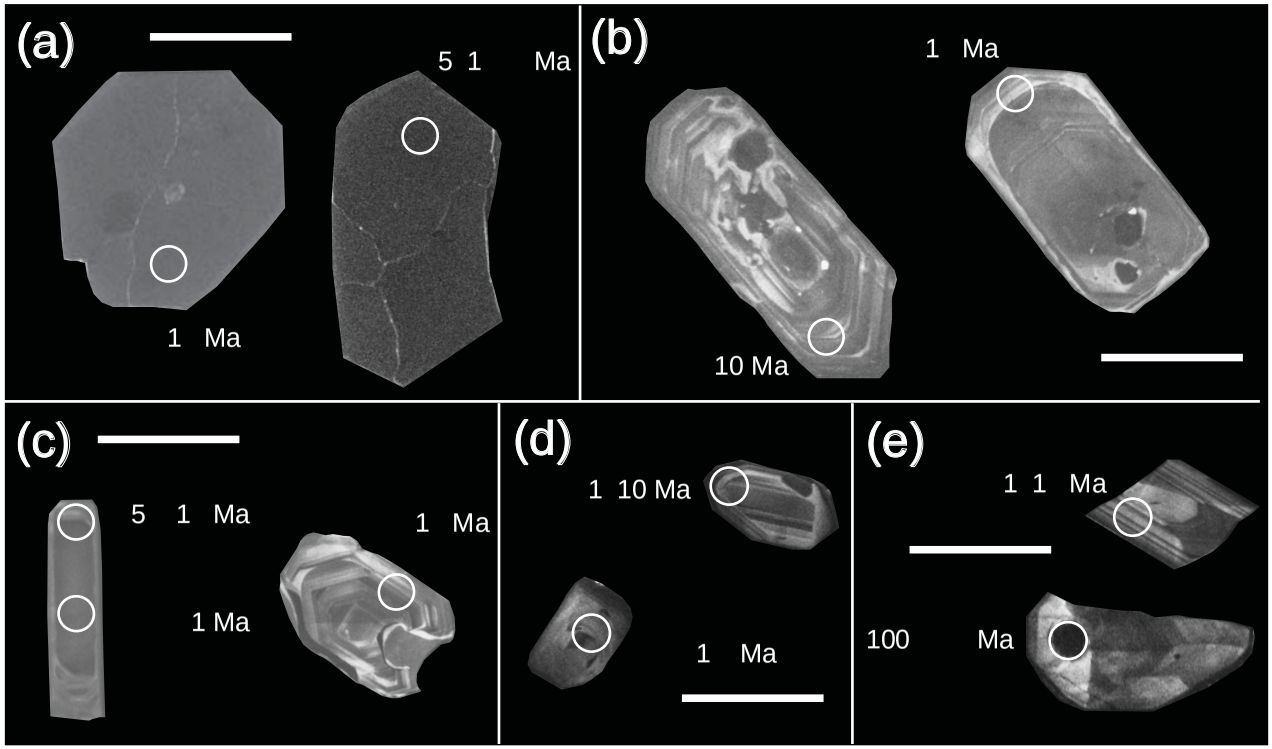

Fig. 6 epresentati e cathodoluminescence ( ) images of ircon grains from granitic roc s and sandstones of the Örmögtei Formation. **(a)** Zircons from non-deformed equigranular granite (1 Hr1 01). **(b)** Zircons from fractured porphyritic granite (11Hr5). **(c)** Zircons from a clast in the cataclasite derived from the porphyritic rhyolite (1 Hr1011). **(d)** Zircons from bedded sandstone (1 Hr0 1). **(e)** Zircons from sandstone of alternating beds of sandstone and mudstone (1 Hr0 1). Analytical spots (white circle) are shown together with concordia ages. hite lines denote 100 m.

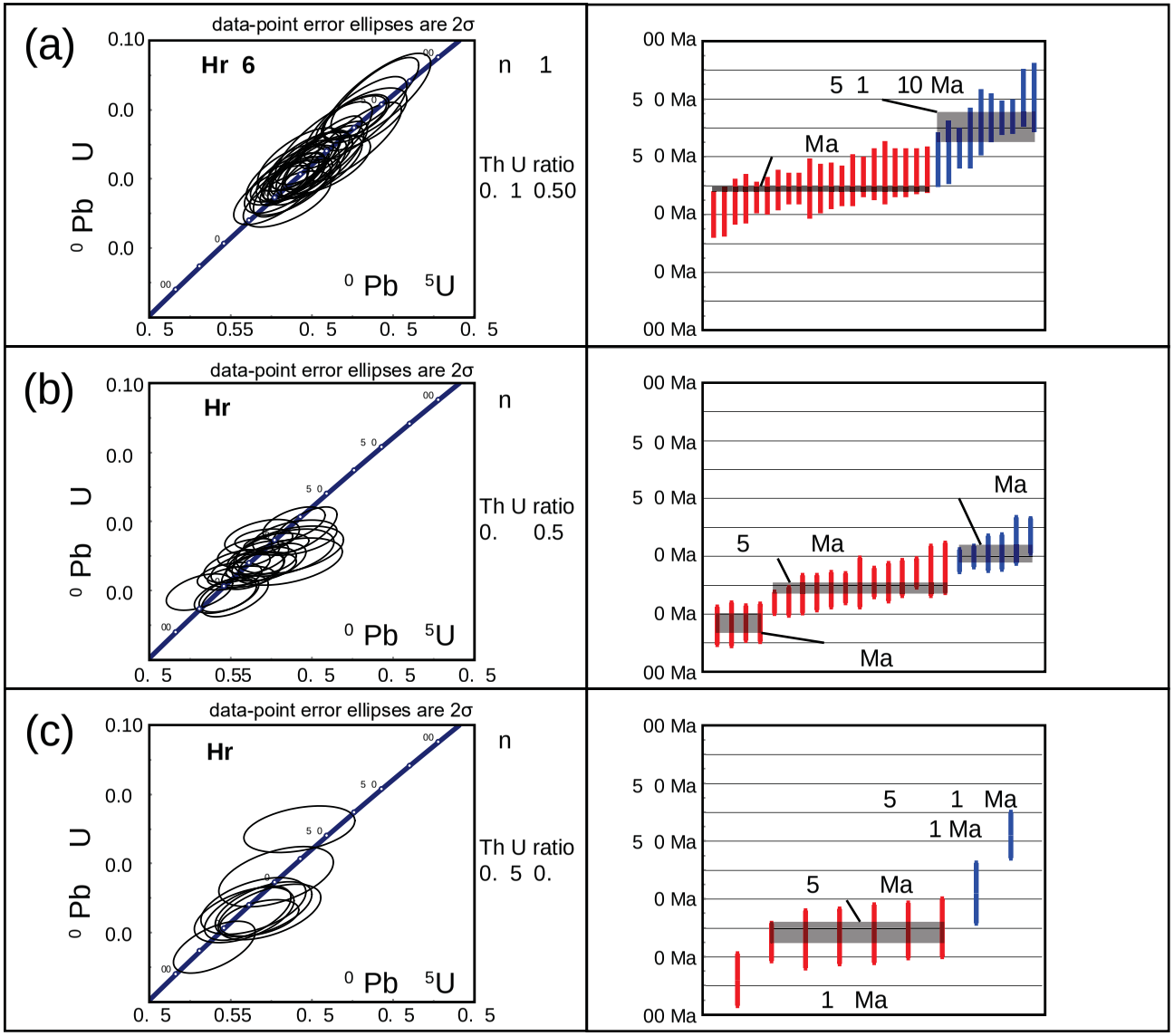

Fig. oncordia diagrams and eighted mean diagrams of the ircon U Pb ages from the granitic roc s. The error ellipses in the concordia diagrams and the vertical error bars in the weighted mean diagrams are 2σ error. The blue and red error bars denote ages from inherited cores and mantle parts of zircons, respectively. The weighted mean ages (shaded) were calculated using Isoplot/Ex program (Ludwig 2012). n: a total number of concordant data points.

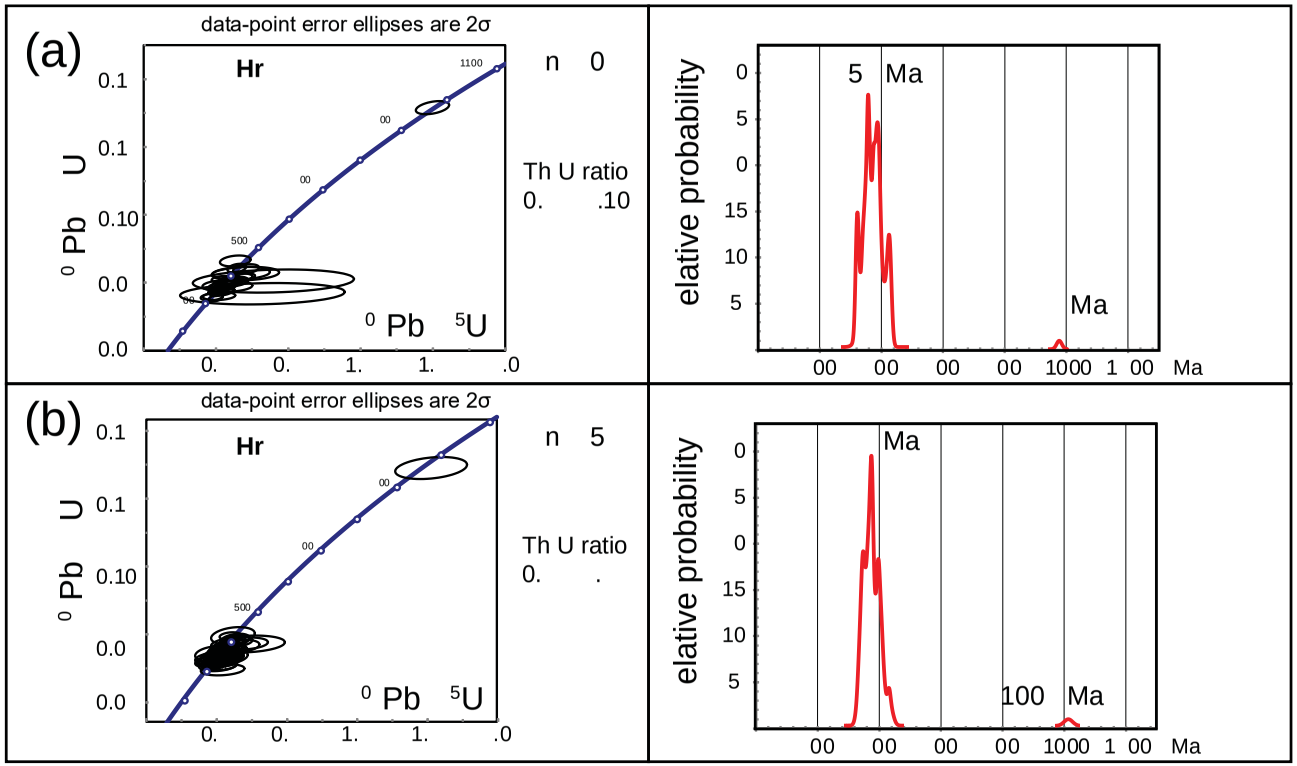

Fig. oncordia diagrams and relati e probabilit plots of the detrital ircon ages from the sandstones of the Örmögtei Formation. The age peak were calculated using soplot Ex program (udwig 01). n: a total number of concordant data points.

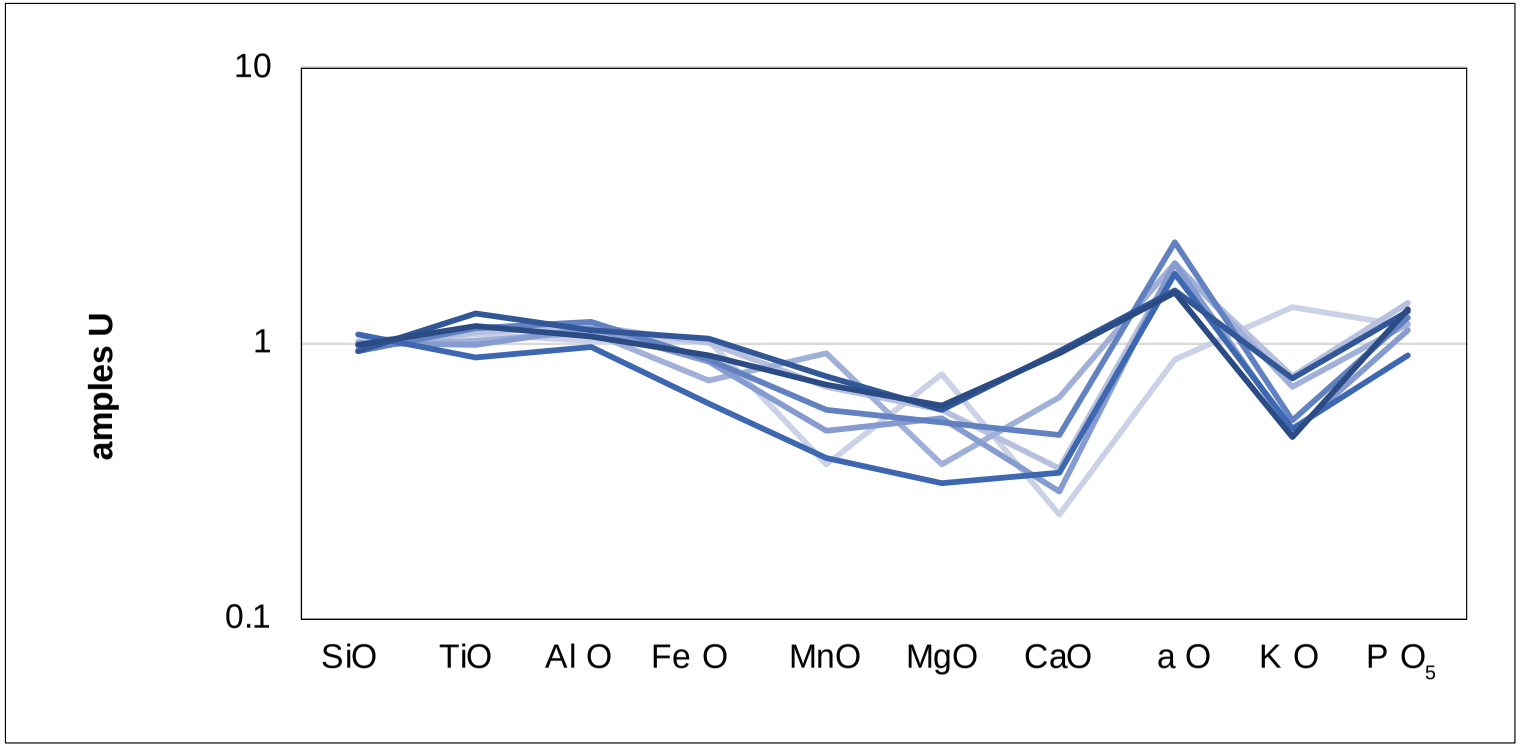

Fig. UCC-normalized multi-element patterns of the sandstone of the Örmögtei Formation. UCC composition by udnick and Gao (00) is used. Fe O : total iron as Fe O .

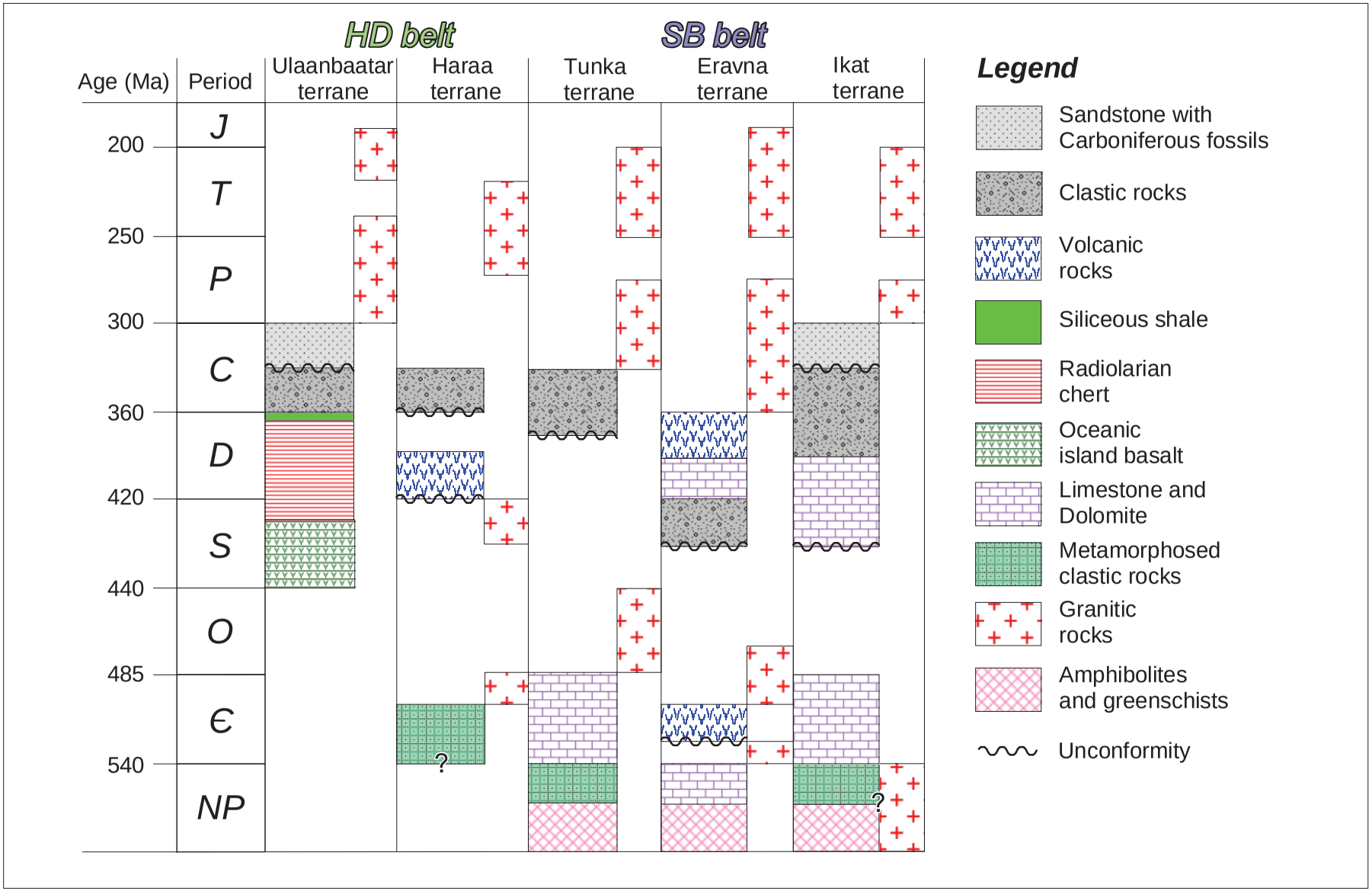

Fig. 20 General stratigraphies of the terranes in the Hangai-Daur (HD) and Sayan-Baikal (SB) belts. Compiled with Kurihara et al. (2008), Tomurtogoo (2012), Takeuchi et al. (2012), Tsukada et al. (2013), Ruzhentsev et al. (2007, 2012), Ryabinin et al. (2011), and Zhimulev et al. (2011).

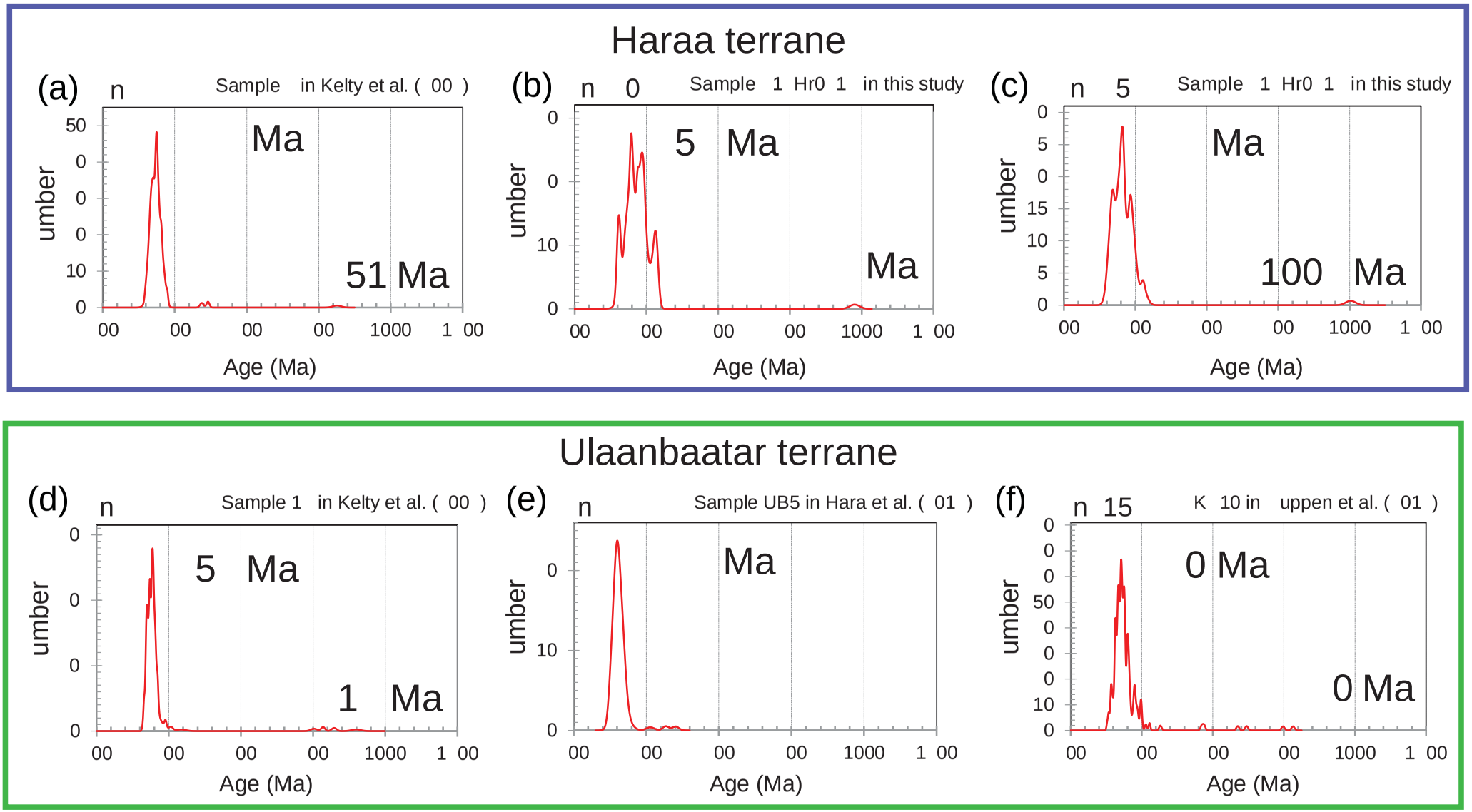

Fig. elati e probabilit plots of the detrital ircons from the arboniferous sandstones in the Ulaanbaatar and Haraa terranes.
n: a total number of concordant data points.

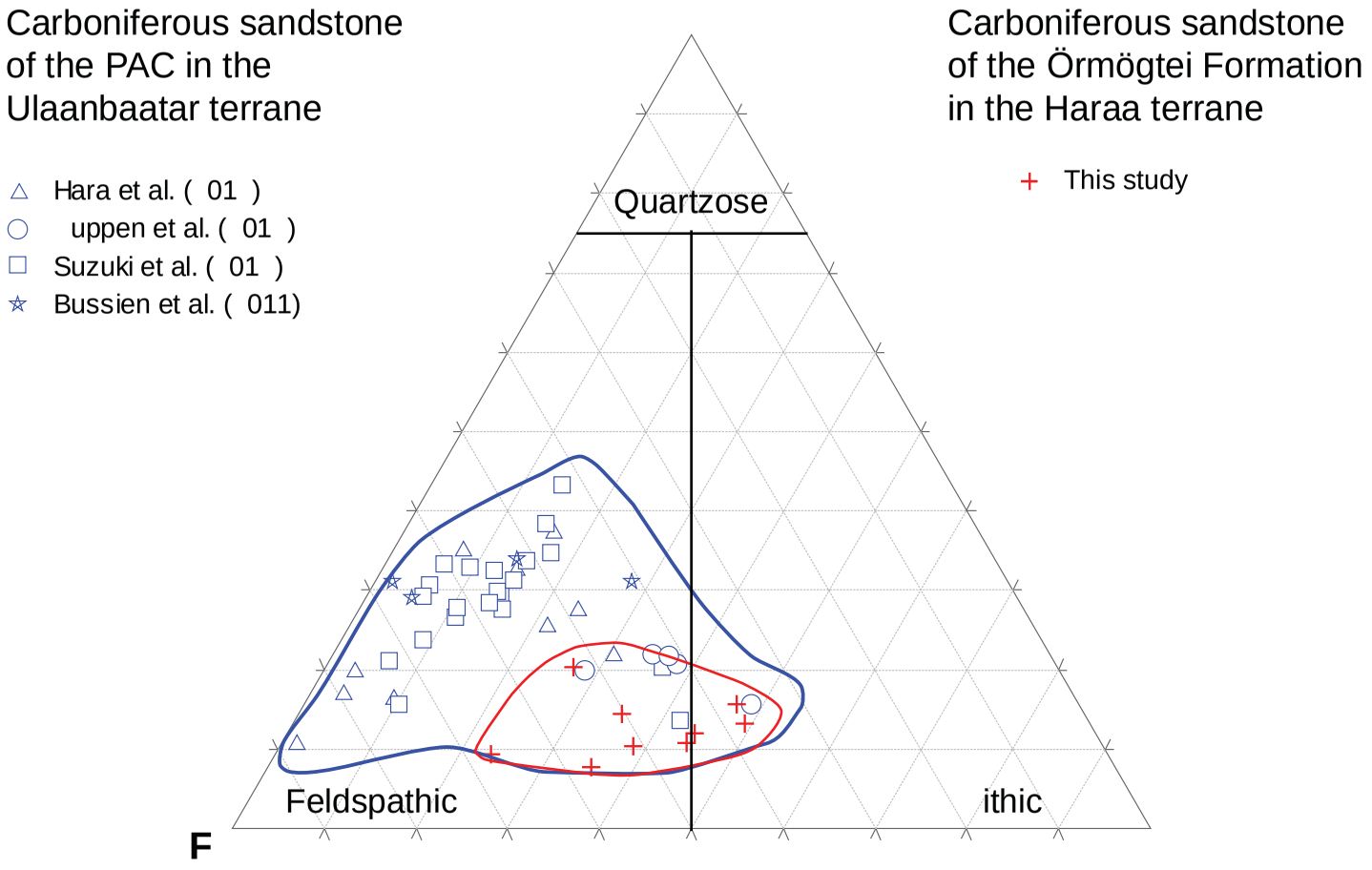

Fig. Petrographic classification of arboniferous sandstones from the Haraa and Ulaanbaatar terranes b F diagram (ada).
The sandstone is classified as feldspathic arenite. Data source is Bussien et al. (011), Suzuki et al. (01), Hara et al. (01) and uppen et al. (01).
Q: monocrystalline quartz, F: K-feldspar + plagioclase, : lithic fragments + polycrystalline quartz.

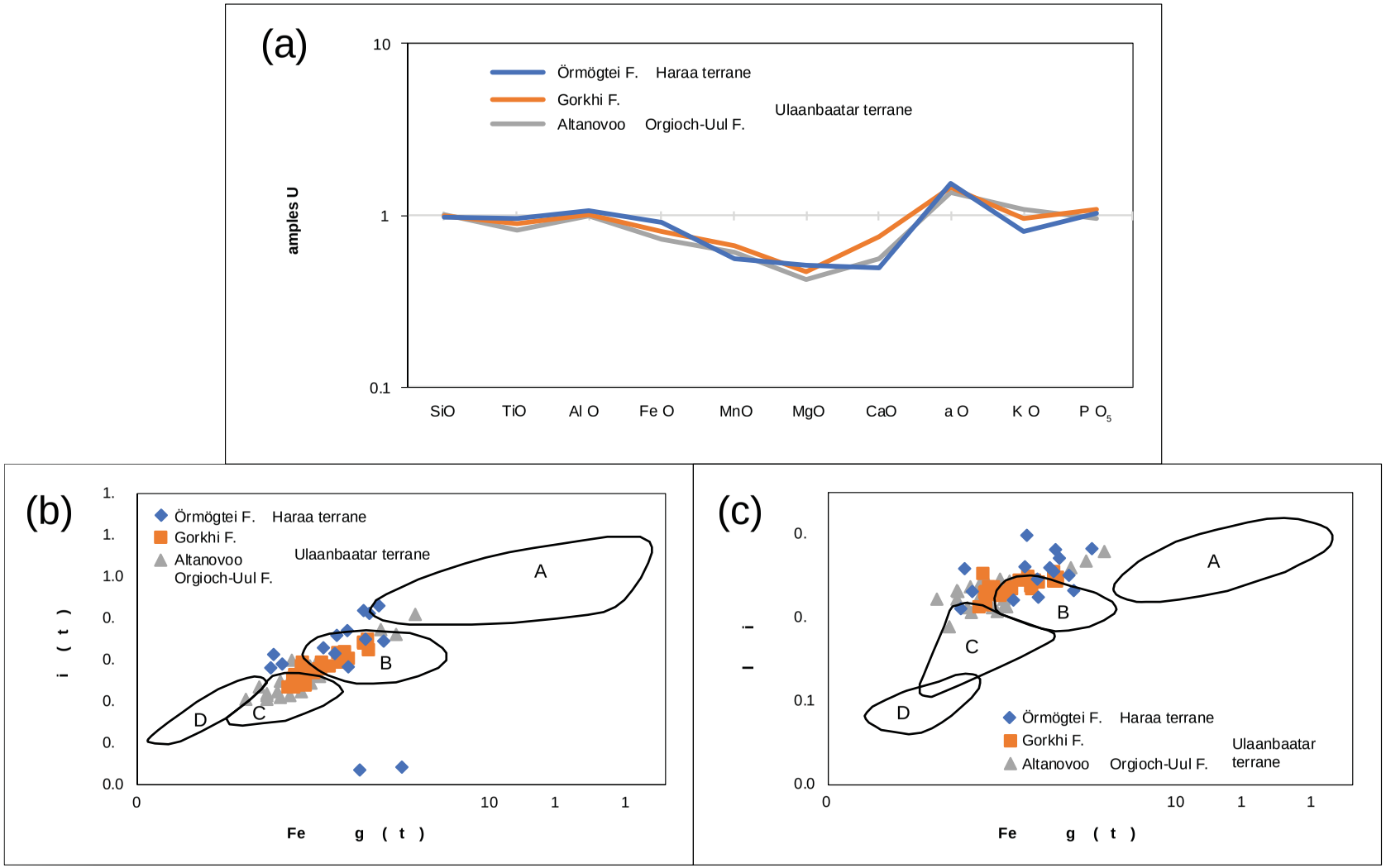

Fig. **(a)** UCC-normalized multi-element patterns of the mean concentrations of the sandstones from the Örmögtei Formation in the Haraa terrane (this study), Gorkhi Formation and Altan-Ovoo Orgioch-Uul Formation in the Ulaanbaatar terrane (Hara et al. 01 akane 01 Purev av et al. 01). UCC composition by udnick and Gao (00) is used. F.: Formation, Fe O : total iron as Fe O . Discriminant diagrams of **(b)** TiO vs. Fe O +MgO and **(c)** Al O SiO vs. Fe O +MgO (Bhatia 1). A: oceanic island arc, B: continental island arc, C: active continental margin, D: passive margin.

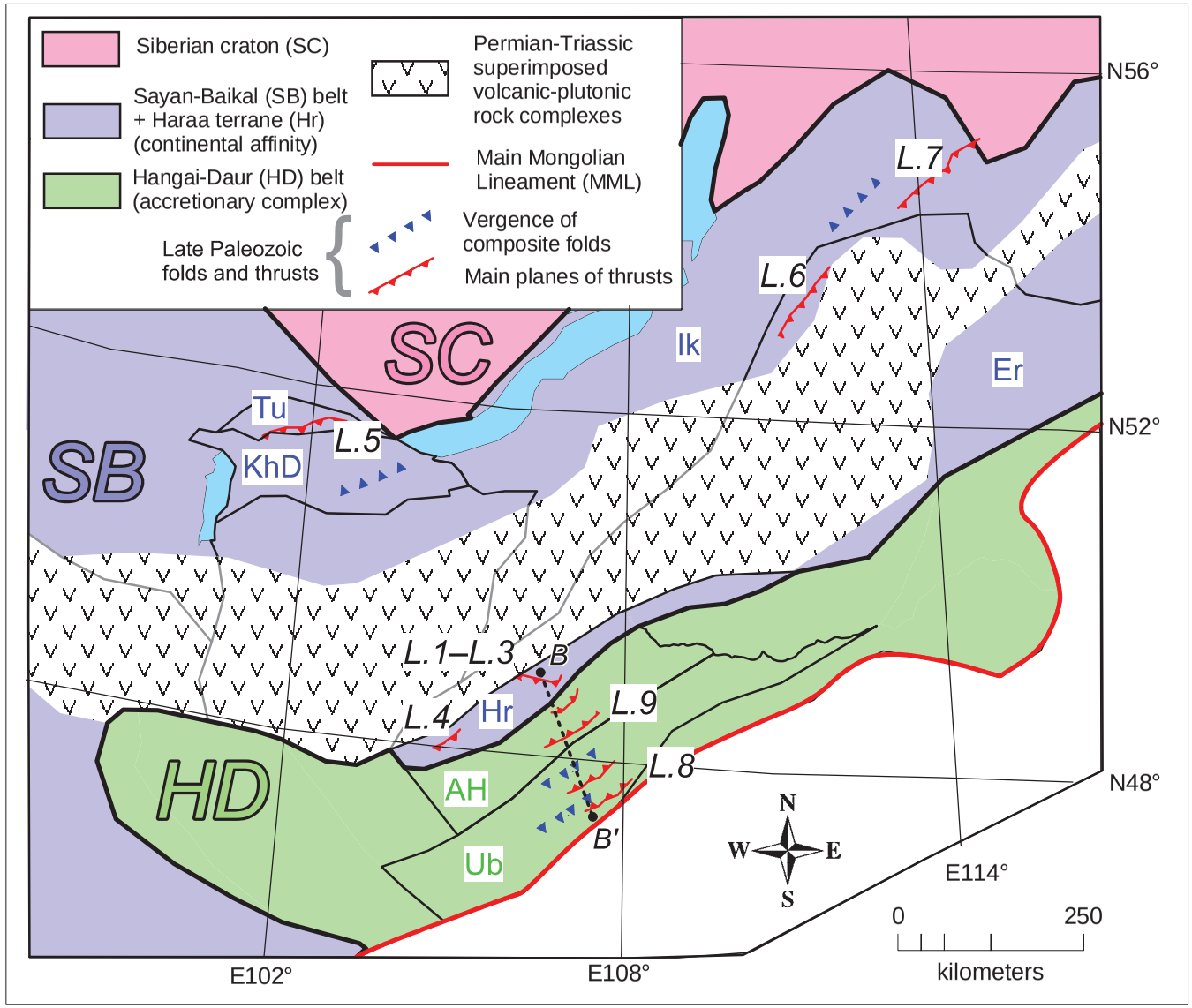

Fig. 24 Distribution of the Late Paleozoic folds and thrusts in the Hangai-Daur and Sayan-Baikal belts.

L.1: Züünharaa area, L.2: Zuunmod area, L.3: Bayangol area, L.4: Zaamar area, L.5: Tunka area, L.6: Ul`zutui, Oldynda and Kydzhimit areas, L.7: Bagdarin area, L.8: Ulaanbaatar area, L.9: Tunhel area.

Tu: Tunka terrane, KhD: Khamar-Daban, Ik: Ikat terrane, Er: Eravna terrane, Hr: Haraa terrane, AH: Asralt Hairhan terrane, Ub: Ulaanbaatar terrane.

Black dashed line is schematic cross section along B–B'.

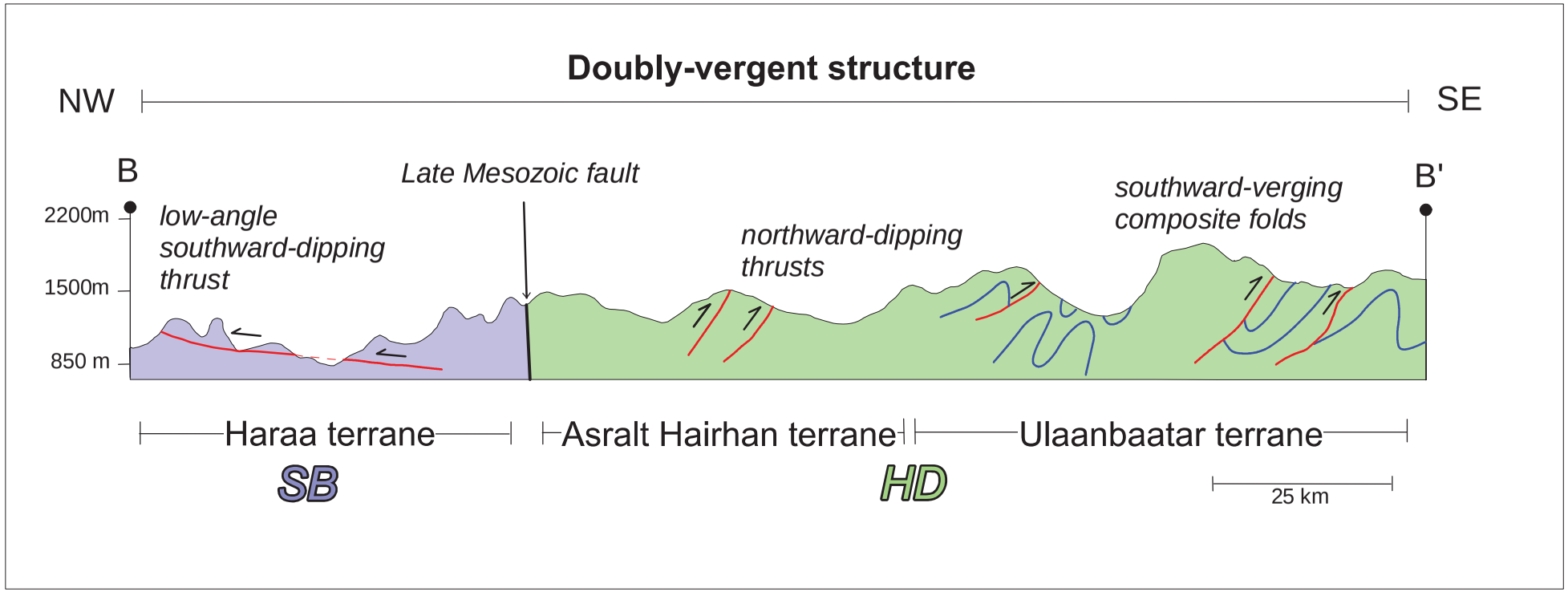

Fig. 25 Schematic cross section shows present tectonic setting of the Late Paleozoic doubly-vergent structure in the Sayan-Baikal (SB) and Hangai-Daur (HD) belts along B–B' in Fig. 24.

Table 1

Rock type and sample number	Grain number and spot location	Th/U	Isotope ratios						Apparent ages (Ma)						^{206}Pbc* (%)	Concordia age (Ma)		MSWD	Probability
			^{207}Pb/^{206}Pb	Error (±2σ)	^{206}Pb/^{238}U	Error (±2σ)	^{207}Pb/^{235}U	Error (±2σ)	^{207}Pb-^{206}Pb age	Error (±2σ)	^{238}U-^{206}Pb age	Error (±2σ)	^{235}U-^{207}Pb age	Error (±2σ)		Conc. age (Ma)	Error (±2σ)		
(a) Equigranular granite, #12Hr1601	1-C	0.47	0.058	0.0023	0.089	0.0030	0.71	0.037	537	21	545	28	547	18	0.14	547	17	0.055	0.81
	2-R	0.34	0.059	0.0024	0.082	0.0028	0.67	0.036	568	23	520	28	509	17	0.27	510	16	1.6	0.20
	3-R	0.32	0.057	0.0023	0.079	0.0026	0.62	0.033	507	21	492	26	489	16	0.040	489	16	0.15	0.70
	4-R	0.29	0.057	0.0023	0.081	0.0027	0.63	0.034	485	20	498	26	501	17	n.d	500	16	0.12	0.73
	7-R	0.25	0.057	0.0023	0.083	0.0028	0.65	0.034	489	20	508	27	512	17	0.10	511	16	0.26	0.61
	8-R	0.34	0.058	0.0027	0.077	0.0027	0.62	0.036	542	25	490	28	479	17	0.31	480	16	1.5	0.22
	9-R	0.34	0.057	0.00085	0.081	0.0027	0.64	0.023	502	7.5	500	18	499	17	0.089	500	14	0.011	0.92
	11-C	0.39	0.060	0.0019	0.085	0.0038	0.70	0.038	592	19	540	29	528	23	0.43	533	21	2.9	0.090
	20-R	0.21	0.057	0.0018	0.082	0.0032	0.65	0.033	497	16	507	26	509	20	n.d	508	18	0.12	0.73
	23-R	0.38	0.056	0.0017	0.082	0.0032	0.64	0.032	468	14	500	25	507	20	0.038	504	18	1.2	0.27
	25-C	0.46	0.057	0.0017	0.092	0.0036	0.73	0.036	503	15	555	27	568	22	0.051	561	20	3.6	0.057
	27-C	0.25	0.058	0.0018	0.083	0.0033	0.67	0.033	532	17	519	26	517	20	0.23	518	19	0.18	0.67
	28-R	0.30	0.057	0.0014	0.080	0.0023	0.62	0.024	479	12	491	19	494	14	0.23	493	13	0.29	0.59
	32-R	0.31	0.057	0.0015	0.080	0.0023	0.63	0.025	481	13	495	20	498	15	n.d	497	14	0.33	0.56
	33-C	0.49	0.057	0.0014	0.085	0.0025	0.67	0.025	503	12	523	20	528	15	n.d	526	14	0.81	0.36
	34-R	0.34	0.056	0.0014	0.082	0.0024	0.64	0.025	473	12	502	19	508	15	n.d	506	14	1.5	0.21
	37-C	0.31	0.057	0.0017	0.089	0.0021	0.70	0.027	507	15	541	21	549	13	0.037	548	12	1.6	0.20
	38-C	0.43	0.057	0.0017	0.089	0.0021	0.70	0.027	504	15	540	20	549	13	0.17	547	12	1.9	0.16
	39-R	0.38	0.059	0.0017	0.080	0.0019	0.65	0.024	559	16	508	19	497	12	0.39	498	11	3.6	0.059
	40-R	0.34	0.056	0.0017	0.080	0.0019	0.61	0.024	440	14	484	19	493	12	n.d	492	11	2.5	0.12
	45-R	0.36	0.058	0.0018	0.080	0.0019	0.64	0.025	511	16	500	20	498	12	n.d	498	11	0.13	0.72
	46-C	0.37	0.058	0.0022	0.092	0.0042	0.73	0.044	520	20	557	33	566	26	n.d	561	24	1.1	0.29
	50-R	0.35	0.057	0.0021	0.080	0.0037	0.64	0.038	511	19	500	30	497	23	0.088	498	21	0.10	0.75
	51-C	0.50	0.058	0.0021	0.089	0.0041	0.70	0.042	516	19	541	32	547	25	0.11	544	23	0.56	0.45
	53-C	0.27	0.057	0.0021	0.085	0.0039	0.66	0.039	475	18	517	31	527	24	0.083	523	22	1.5	0.22
	54-R	0.32	0.058	0.0022	0.082	0.0038	0.65	0.039	527	20	511	31	508	24	0.014	509	22	0.19	0.66
	55-R	0.31	0.056	0.0022	0.083	0.0030	0.63	0.034	436	17	499	27	513	19	0.043	509	17	3.0	0.083
	56-R	0.35	0.056	0.0022	0.081	0.0029	0.62	0.034	444	18	490	27	500	18	n.d	498	17	1.6	0.21
	57-R	0.27	0.056	0.0022	0.079	0.0029	0.62	0.033	468	18	488	26	492	18	0.049	491	17	0.31	0.58
	61-R	0.33	0.058	0.0023	0.082	0.0030	0.66	0.035	545	21	514	27	507	18	0.52	509	17	0.73	0.39
	62-R	0.37	0.056	0.0023	0.078	0.0028	0.60	0.033	468	19	479	26	482	18	0.089	482	17	0.10	0.75

* Percentage of ^{206}Pb contributed by common Pb on the basis of ^{204}Pb. The data are displayed to 2 significant digits.

Value of common Pb was assumed by Stacey and Kramers (1975) model. n.d. : no detection of ^{204}Pb, C: core, R: rim.

Table 1

Rock type and sample number	Grain number and spot location	Th/U	Isotope ratios						Apparent ages (Ma)						^{206}Pbc* (%)	Concordia age (Ma)		MSWD	Probability
			^{207}Pb/^{206}Pb	Error (±2σ)	^{206}Pb/^{238}U	Error (±2σ)	^{207}Pb/^{235}U	Error (±2σ)	^{207}Pb-^{206}Pb age	Error (±2σ)	^{238}U-^{206}Pb age	Error (±2σ)	^{235}U-^{207}Pb age	Error (±2σ)		Conc. age (Ma)	Error (±2σ)		
(b) Porphyritic granite, #11Hr54	1-C	0.58	0.057	0.0024	0.080	0.0020	0.63	0.031	500	21	494	13	495	25	0.40	494	12	0.013	0.91
	6-R	0.45	0.055	0.0030	0.074	0.0019	0.56	0.033	414	22	457	12	450	27	n.d	457	12	0.54	0.46
	7-C	0.42	0.055	0.0032	0.078	0.0021	0.59	0.038	411	24	483	13	470	30	n.d	482	12	1.3	0.25
	9-R	0.53	0.057	0.0026	0.075	0.0020	0.58	0.031	477	22	465	12	467	25	0.024	465	12	0.054	0.82
	11-R	0.47	0.058	0.0029	0.069	0.0024	0.56	0.034	539	27	431	15	449	27	n.d	433	15	3.6	0.057
	13-R	0.44	0.061	0.0049	0.074	0.0028	0.62	0.056	623	51	462	17	490	44	n.d	462	17	3.0	0.083
	14-C	0.54	0.059	0.0023	0.079	0.0027	0.64	0.033	565	22	489	17	503	26	0.35	491	16	3.0	0.082
	16-R	0.46	0.059	0.0043	0.075	0.0028	0.62	0.050	572	42	469	17	487	40	n.d	470	17	1.6	0.21
	16-R	0.47	0.059	0.0047	0.076	0.0028	0.62	0.054	586	46	472	18	492	43	n.d	472	17	1.7	0.20
	19-R	0.37	0.057	0.0032	0.072	0.0012	0.56	0.034	479	27	448	7.8	453	27	n.d	448	7.5	0.23	0.63
	25-C	0.45	0.055	0.0026	0.077	0.0012	0.59	0.029	427	20	481	7.5	471	23	1.0	480	7.2	1.1	0.30
	26-C	0.39	0.057	0.0030	0.077	0.0013	0.61	0.033	503	26	477	7.8	481	26	0.53	477	7.6	0.20	0.65
	28-R	0.40	0.058	0.0031	0.074	0.0017	0.59	0.034	515	27	462	10	471	27	n.d	462	10	0.78	0.38
	31-R	0.48	0.058	0.0032	0.073	0.0017	0.59	0.036	531	30	457	10	469	28	n.d	458	10	1.4	0.25
	32-R	0.46	0.055	0.0028	0.075	0.0017	0.57	0.031	413	21	469	10	460	25	n.d	469	10	1.1	0.30
	36-R	0.50	0.055	0.0030	0.072	0.0016	0.55	0.032	419	23	449	10	444	26	n.d	449	10	0.25	0.62
	37-R	0.38	0.057	0.0028	0.069	0.0021	0.54	0.031	488	24	432	13	441	25	0.85	432	13	1.1	0.31
	38-R	0.49	0.057	0.0026	0.069	0.0021	0.55	0.030	502	23	433	13	444	24	1.5	434	12	1.7	0.19
	40-C	0.42	0.059	0.0028	0.074	0.0022	0.60	0.034	562	27	461	14	478	27	0.088	462	13	3.5	0.061
	40-R	0.41	0.053	0.0030	0.070	0.0021	0.51	0.033	336	19	435	13	419	27	1.2	434	13	2.5	0.12
	44-R	0.49	0.058	0.0026	0.073	0.0022	0.58	0.032	512	23	453	14	463	25	0.049	454	13	1.3	0.26
	47-R	0.47	0.057	0.0033	0.073	0.0020	0.57	0.037	475	28	455	13	458	29	0.27	455	12	0.089	0.77
	59-C	0.48	0.059	0.0036	0.078	0.0021	0.63	0.042	559	34	482	13	496	33	0.030	483	12	1.2	0.27
(c) Porphyritic rhyolite, #12Hr1011	4-R	0.50	0.057	0.0036	0.068	0.0031	0.53	0.041	478	30	424	19	432	34	0.72	424	18	0.56	0.46
	5-C	0.42	0.054	0.0044	0.085	0.0027	0.63	0.056	379	31	526	17	499	44	n.d	524	16	2.8	0.10
	5-R	0.44	0.059	0.0036	0.072	0.0022	0.59	0.039	562	34	449	13	468	32	0.015	450	13	2.7	0.10
	6-C	0.40	0.056	0.0047	0.078	0.0036	0.61	0.058	464	39	485	22	481	46	4.0	484	21	0.051	0.82
	6-R	0.79	0.057	0.0036	0.073	0.0032	0.57	0.044	487	30	453	20	459	35	0.42	454	19	0.23	0.63
	7-R	0.58	0.058	0.0040	0.073	0.0033	0.59	0.048	544	38	457	20	471	39	1.3	458	19	1.2	0.26
	8-R	0.35	0.057	0.0043	0.073	0.0033	0.57	0.050	477	36	452	20	456	40	0.57	452	20	0.087	0.77
	9-R	0.39	0.057	0.0045	0.074	0.0034	0.58	0.053	483	38	459	21	463	42	n.d	460	20	0.069	0.79
	9-R	0.49	0.059	0.0044	0.073	0.0033	0.60	0.052	583	43	454	20	476	41	0.78	456	20	2.3	0.13

* Percentage of ^{206}Pb contributed by common Pb on the basis of ^{204}Pb. The data are displayed to 2 significant digits.

Value of common Pb was assumed by Stacey and Kramers (1975) model. n.d. : no detection of ^{204}Pb, C: core, R: rim.

Table 2

Rock type and sample number	Grain number	Th/U	Isotope ratios						Apparent ages (Ma)						^{206}Pbc* (%)	Concordia age (Ma)		MSWD	Probability
			^{207}Pb/^{206}Pb	Error (±2σ)	^{206}Pb/^{238}U	Error (±2σ)	^{207}Pb/^{235}U	Error (±2σ)	^{207}Pb-^{206}Pb age	Error (±2σ)	^{238}U-^{206}Pb age	Error (±2σ)	^{235}U-^{207}Pb age	Error (±2σ)		Conc. age (Ma)	Error (±2σ)		
(a) Fine to	7	0.49	0.057	0.0056	0.057	0.0016	0.45	0.046	476	47	359	10	375	38	3.2	359	10	1.1	0.30
medium grained	9	0.96	0.085	0.043	0.061	0.0056	0.72	0.36	1322	661	382	35	549	279	n.d	381	34	2.1	0.15
sandstone	11	0.57	0.060	0.0059	0.068	0.0024	0.57	0.059	617	60	424	15	456	47	2.5	425	14	2.9	0.087
#12Hr0814	15	0.62	0.059	0.0080	0.061	0.0024	0.49	0.070	573	78	380	15	408	58	n.d	380	15	1.5	0.22
	16	0.67	0.055	0.0067	0.059	0.0022	0.45	0.057	415	50	368	14	375	48	2.0	368	13	0.11	0.74
	17	1.8	0.057	0.0041	0.051	0.0016	0.40	0.031	484	35	321	10	341	27	n.d	321	10	3.8	0.052
	21	0.91	0.055	0.0040	0.054	0.0016	0.41	0.032	403	29	340	10	348	27	n.d	340	10	0.58	0.45
	27	0.47	0.056	0.0072	0.055	0.0020	0.43	0.056	462	59	345	12	360	48	1.6	345	12	0.63	0.43
	29	0.77	0.053	0.0068	0.052	0.0017	0.38	0.050	323	42	324	11	324	43	n.d	324	10	0.00013	0.99
	34	0.91	0.057	0.0064	0.061	0.0018	0.48	0.056	483	54	384	11	399	46	1.6	384	11	0.59	0.44
	35	0.53	0.051	0.0051	0.062	0.0016	0.43	0.045	222	23	388	10	365	38	1.9	387	10	2.2	0.14
	36	1.1	0.061	0.0069	0.063	0.0020	0.53	0.062	624	71	394	12	430	51	1.8	394	12	3.0	0.081
	38	0.88	0.071	0.0031	0.16	0.0031	1.6	0.076	958	41	974	19	969	46	n.d	974	17	0.14	0.71
	40	0.98	0.060	0.012	0.058	0.0024	0.48	0.099	613	124	362	15	398	82	n.d	362	15	1.1	0.29
	45	0.59	0.060	0.014	0.066	0.0030	0.54	0.13	592	139	410	19	439	105	11	410	18	0.46	0.50
	46	0.92	0.089	0.050	0.054	0.0051	0.66	0.37	1409	785	336	32	513	290	0.094	335	31	2.1	0.15
	47	0.64	0.054	0.0030	0.058	0.0016	0.43	0.027	387	22	362	10	365	23	0.77	362	10	0.16	0.69
	49	1.6	0.051	0.0067	0.073	0.0025	0.51	0.069	221	29	453	16	417	57	n.d	425	15	2.7	0.10
	50	0.67	0.057	0.0069	0.060	0.0021	0.47	0.059	497	60	376	13	393	49	1.3	376	13	0.76	0.38
	52	0.54	0.057	0.0037	0.061	0.0017	0.48	0.034	475	31	385	11	398	28	n.d	385	10	1.5	0.22
	53	0.54	0.054	0.0042	0.069	0.0020	0.52	0.043	391	30	428	13	422	35	1.1	428	12	0.19	0.67
	54	0.72	0.052	0.0094	0.058	0.0024	0.42	0.078	299	54	366	15	357	66	3.3	366	14	0.11	0.74
	58	0.67	0.061	0.0071	0.064	0.0019	0.54	0.064	652	75	397	12	437	52	n.d	398	11	3.6	0.058
	59	0.86	0.056	0.0044	0.063	0.0013	0.49	0.040	455	36	392	8.4	402	33	0.46	393	8.2	0.48	0.49
	63	0.77	0.057	0.0071	0.055	0.0017	0.43	0.056	480	60	348	11	366	47	2.4	348	10	0.83	0.36
	65	2.1	0.058	0.010	0.052	0.0019	0.42	0.073	537	92	327	12	354	62	6.9	327	12	1.1	0.30
	66	1.7	0.054	0.0045	0.060	0.0013	0.45	0.038	365	30	376	8.0	374	32	1.0	376	7.8	0.016	0.90
	67	0.62	0.062	0.017	0.065	0.0033	0.56	0.15	688	183	408	21	453	122	0.87	408	20	0.82	0.37
	68	0.94	0.052	0.0036	0.057	0.0011	0.41	0.029	281	19	358	6.7	348	25	2.3	357	6.5	1.0	0.32
	69	0.49	0.054	0.0053	0.056	0.0013	0.42	0.043	392	38	352	8.4	357	36	5.1	352	8.2	0.12	0.72

* Percentage of ^{206}Pb contributed by common Pb on the basis of ^{204}Pb. The data are displayed to 2 significant digits.

Value of common Pb was assumed by Stacey and Kramers (1975) model. n.d. : no detection of ^{204}Pb.

Table 2

Rock type and sample number	Grain number	Th/U	Isotope ratios						Apparent ages (Ma)						^{206}Pbc* (%)	Concordia age (Ma)		MSWD	Probability
			^{207}Pb/^{206}Pb	Error (±2σ)	^{206}Pb/^{238}U	Error (±2σ)	^{207}Pb/^{235}U	Error (±2σ)	^{207}Pb-^{206}Pb age	Error (±2σ)	^{238}U-^{206}Pb age	Error (±2σ)	^{235}U-^{207}Pb age	Error (±2σ)		Conc. age (Ma)	Error (±2σ)		
(b) Coarse grained sandstone #12Hr0819	1	0.97	0.058	0.012	0.051	0.0026	0.41	0.087	512	107	322	16	346	74	n.d	322	16	0.61	0.44
	2	0.97	0.058	0.0082	0.064	0.0024	0.51	0.076	513	73	403	15	420	62	n.d	403	15	0.45	0.50
	4	0.72	0.057	0.0032	0.062	0.0014	0.48	0.029	473	27	388	8.6	400	24	n.d	387	8.4	1.8	0.18
	7	0.81	0.052	0.0067	0.058	0.0020	0.41	0.056	283	37	363	12	352	47	n.d	362	12	0.30	0.58
	8	1.7	0.050	0.0054	0.053	0.0016	0.36	0.041	182	20	333	10	315	35	n.d	333	10	1.6	0.21
	9	0.90	0.055	0.0077	0.059	0.0023	0.45	0.065	425	59	370	14	378	55	n.d	370	14	0.12	0.73
	11	1.0	0.057	0.0062	0.054	0.0018	0.42	0.049	488	54	339	12	359	41	n.d	340	11	1.4	0.24
	13	0.97	0.055	0.0078	0.059	0.0023	0.45	0.066	412	58	369	15	375	55	n.d	369	14	0.070	0.79
	14	1.3	0.058	0.0054	0.058	0.0018	0.46	0.045	520	48	361	11	383	37	3.3	361	11	2.2	0.14
	18	0.83	0.057	0.0060	0.061	0.0023	0.48	0.054	504	53	381	15	399	45	n.d	381	14	1.0	0.31
	19	0.87	0.049	0.0096	0.055	0.0027	0.37	0.075	141	28	345	17	320	65	n.d	345	16	0.89	0.34
	22	1.4	0.049	0.0073	0.054	0.0023	0.36	0.056	133	20	336	14	312	49	n.d	335	14	1.5	0.22
	24	1.2	0.052	0.0037	0.056	0.0019	0.41	0.032	296	21	354	12	346	27	n.d	354	12	0.53	0.47
	26	0.79	0.054	0.0079	0.054	0.0023	0.40	0.061	381	56	340	15	345	52	n.d	340	14	0.060	0.81
	27	0.98	0.060	0.0094	0.053	0.0019	0.44	0.071	596	93	335	12	370	60	0.85	335	12	2.0	0.16
	28	0.64	0.051	0.0051	0.068	0.0017	0.48	0.049	251	25	422	10	396	41	0.73	421	10	2.4	0.12
	30	1.5	0.052	0.0051	0.058	0.0014	0.42	0.042	302	29	365	8.8	356	35	0.31	365	8.6	0.34	0.56
	31	0.74	0.064	0.012	0.063	0.0028	0.56	0.11	731	140	396	17	449	88	10	397	17	2.2	0.14
	32	0.79	0.067	0.019	0.063	0.0038	0.58	0.17	827	239	394	24	464	137	9.0	394	23	1.6	0.21
	33	1.2	0.055	0.0065	0.056	0.0016	0.43	0.052	416	49	353	10	361	44	n.d	352	10	0.22	0.64
	34	2.1	0.057	0.0040	0.058	0.0012	0.46	0.033	492	34	365	7.3	383	28	n.d	365	7.1	2.5	0.11
	38	1.9	0.049	0.0061	0.053	0.0019	0.35	0.046	142	18	330	12	308	40	4.8	330	11	1.8	0.18
	39	1.1	0.054	0.0087	0.057	0.0024	0.42	0.071	354	58	360	15	359	60	n.d	360	15	0.0013	0.97
	40	0.90	0.059	0.0064	0.061	0.0021	0.49	0.056	549	60	380	13	405	47	0.81	380	13	1.8	0.18
	41	1.5	0.055	0.0072	0.057	0.0022	0.43	0.059	416	54	359	14	367	50	n.d	359	13	0.14	0.71
	42	0.84	0.061	0.0081	0.055	0.0022	0.46	0.064	635	84	346	14	387	53	3.5	346	13	3.4	0.064
	44	0.79	0.062	0.011	0.062	0.0029	0.53	0.093	671	114	387	18	431	76	1.7	387	17	2.0	0.15
	46	1.3	0.055	0.0069	0.052	0.0021	0.39	0.052	424	53	325	13	338	44	n.d	325	13	0.46	0.50
	50	2.7	0.056	0.0049	0.051	0.0018	0.40	0.038	461	41	324	11	341	32	1.2	324	11	1.8	0.18
	51	1.1	0.047	0.0073	0.053	0.0023	0.35	0.055	61	9.4	333	14	301	48	n.d	332	14	2.6	0.11
	53	1.1	0.061	0.0076	0.059	0.0024	0.49	0.065	631	79	370	15	408	54	n.d	370	15	3.2	0.075
	54	1.9	0.055	0.0064	0.054	0.0020	0.41	0.050	404	47	339	12	347	42	n.d	339	12	0.24	0.62
	56	1.5	0.056	0.0087	0.056	0.0024	0.43	0.069	445	70	349	15	362	59	n.d	350	15	0.28	0.59

* Percentage of ^{206}Pb contributed by common Pb on the basis of ^{204}Pb. The data are displayed to 2 significant digits.

Value of common Pb was assumed by Stacey and Kramers (1975) model. n.d. : no detection of ^{204}Pb.

Table 2

Rock type and sample number	Grain number	Th/U	Isotope ratios						Apparent ages (Ma)						^{206}Pbc* (%)	Concordia age (Ma)		MSWD	Probability
			^{207}Pb/^{206}Pb	Error (±2σ)	^{206}Pb/^{238}U	Error (±2σ)	^{207}Pb/^{235}U	Error (±2σ)	^{207}Pb-^{206}Pb age	Error (±2σ)	^{238}U-^{206}Pb age	Error (±2σ)	^{235}U-^{207}Pb age	Error (±2σ)		Conc. age (Ma)	Error (±2σ)		
(b) Coarse	57	0.69	0.057	0.0054	0.059	0.0020	0.46	0.047	480	46	368	12	384	39	0.73	368	12	1.0	0.31
grained	59	0.84	0.060	0.0082	0.057	0.0023	0.47	0.067	598	82	356	14	390	56	n.d	356	14	2.3	0.13
sandstone	60	0.64	0.058	0.0056	0.063	0.0021	0.50	0.051	514	50	396	13	413	42	1.8	396	13	1.1	0.29
#12Hr0819	61	0.33	0.059	0.0072	0.056	0.0021	0.46	0.058	576	70	350	13	381	48	n.d	350	13	2.6	0.11
	63	0.94	0.052	0.0074	0.059	0.0029	0.43	0.064	295	42	372	18	361	54	0.49	372	17	0.24	0.62
	64	0.61	0.056	0.0051	0.065	0.0027	0.50	0.050	446	41	405	17	411	41	3.4	405	16	0.16	0.69
	66	0.86	0.048	0.0098	0.058	0.0033	0.38	0.081	80	17	361	21	326	70	17	360	20	1.6	0.21
	67	0.93	0.055	0.0087	0.061	0.0031	0.46	0.077	396	63	381	20	383	64	9.0	381	19	0.0067	0.93
	68	1.4	0.058	0.0067	0.056	0.0026	0.45	0.056	533	62	354	16	379	47	1.9	354	16	1.8	0.18
	70	0.64	0.053	0.010	0.068	0.0039	0.49	0.10	322	64	422	24	407	84	3.7	422	23	0.21	0.64
	71	1.0	0.057	0.0051	0.055	0.0023	0.44	0.043	496	44	348	15	368	36	0.88	349	14	2.0	0.15
	72	1.1	0.053	0.0057	0.054	0.0015	0.39	0.043	308	33	336	10	333	37	n.d	336	9.4	0.055	0.81
	74	0.70	0.051	0.0046	0.059	0.0015	0.41	0.039	236	21	368	9.3	351	33	n.d	368	9.0	1.7	0.19
	76	1.0	0.053	0.0049	0.063	0.0016	0.46	0.044	323	30	395	10	385	37	n.d	395	10	0.50	0.48
	77	0.75	0.055	0.013	0.054	0.0030	0.41	0.10	417	101	337	19	347	86	1.0	337	18	0.082	0.77
	90	1.9	0.059	0.0078	0.056	0.0025	0.45	0.064	553	74	352	16	380	54	n.d	353	16	1.7	0.20
	91	0.65	0.059	0.010	0.058	0.0030	0.48	0.085	569	97	366	19	395	71	1.9	366	19	1.0	0.31
	92	0.82	0.052	0.0043	0.061	0.0023	0.44	0.040	282	24	382	14	368	34	0.87	382	14	1.2	0.28
	93	0.97	0.056	0.0072	0.068	0.0030	0.53	0.071	451	58	427	19	430	58	1.9	427	18	0.027	0.87
	95	1.3	0.059	0.0075	0.063	0.0028	0.51	0.068	558	71	393	17	417	56	n.d	393	17	1.3	0.26
	96	0.72	0.054	0.011	0.058	0.0032	0.43	0.090	391	78	362	20	366	76	4.7	362	20	0.016	0.90
	97	0.69	0.057	0.014	0.059	0.0038	0.46	0.12	511	123	367	24	387	96	n.d	367	23	0.27	0.60
	98	1.7	0.055	0.0030	0.058	0.0020	0.44	0.029	412	23	361	13	368	24	0.028	362	12	0.65	0.42
	99	0.56	0.073	0.0071	0.17	0.0052	1.7	0.17	1016	99	1003	31	1007	103	0.45	1003	28	0.016	0.90
	100	0.49	0.059	0.0050	0.062	0.0016	0.50	0.044	551	47	386	10	410	37	3.3	386	9.6	2.8	0.093
	101	0.69	0.064	0.015	0.051	0.0027	0.45	0.11	756	172	321	17	380	89	n.d	321	17	2.5	0.11
	103	0.71	0.097	0.013	0.058	0.0025	0.77	0.11	1568	215	363	16	582	84	n.d	363	14	2.0	0.16
	104	1.7	0.055	0.0037	0.058	0.0013	0.44	0.031	428	29	361	8.0	370	26	n.d	361	7.7	0.77	0.38
	106	0.67	0.050	0.0058	0.061	0.0018	0.43	0.050	213	24	384	11	361	43	n.d	384	11	1.9	0.17
	108	1.5	0.058	0.0092	0.062	0.0026	0.50	0.082	541	85	390	16	412	67	6.9	390	16	0.69	0.40
	109	0.92	0.060	0.010	0.054	0.0024	0.45	0.077	608	102	337	15	374	65	0.0069	337	15	1.9	0.17
	112	0.76	0.060	0.0068	0.062	0.0021	0.52	0.061	617	70	390	13	424	50	n.d	390	13	3.0	0.083

* Percentage of ^{206}Pb contributed by common Pb on the basis of ^{204}Pb. The data are displayed to 2 significant digits.

Value of common Pb was assumed by Stacey and Kramers (1975) model. n.d. : no detection of ^{204}Pb.

Table 3

Chemical composition of the sandstone of the Örmögtei Formation

Horizons	h5	h6	h6	h6	h6	h8	h8	h9	h9
Sample number	12Hr0809	12Hr0812	12Hr0813	12Hr0814	12Hr0816	15Hr2330	12Hr0822	12Hr0829	15Hr2320
Major element oxides (wt%)									
SiO_2	67.8	62.7	65.7	66.3	61.7	68.9	70.9	62.7	65.4
TiO_2	0.689	0.699	0.653	0.630	0.721	0.660	0.564	0.826	0.740
Al_2O_3	15.8	17.7	16.8	17.3	18.4	15.3	14.9	17.0	16.2
Fe_2O_3*	5.12	5.07	3.69	4.30	4.42	4.23	3.03	5.18	4.52
MnO	0.036	0.069	0.091	0.048	0.057	0.048	0.038	0.075	0.070
MgO	1.90	1.42	0.897	1.32	1.27	1.07	0.763	1.42	1.46
CaO	0.862	1.26	2.29	1.03	1.67	1.40	1.21	3.34	3.29
Na_2O	2.86	6.23	6.42	6.32	7.66	4.37	5.86	5.06	4.95
K_2O	3.79	2.13	1.95	1.33	1.46	2.67	1.38	2.09	1.28
P_2O_5	0.172	0.209	0.176	0.167	0.184	0.162	0.136	0.195	0.198
Total	99.0	97.5	98.7	98.7	97.6	98.8	98.8	97.9	98.1
LOI	1.87	1.75	2.31	1.91	1.83	1.99	1.49	1.99	2.30
Trace elements (ppm)									
Cr	25	1	b.d.l.	b.d.l.	6	3	1	11	n.d
Co	5	7	6	5	6	4	3	3	n.d
Ni	15	7	10	7	10	7	8	9	n.d
Cu	15	b.d.l.	1	b.d.l.	b.d.l	14	b.d.l	9	n.d
Zn	82	105	82	84	93	78	71	82	n.d
Ga	22	25	23	24	25	25	19	23	n.d
Rb	122	52	46	37	29	94	38	114	n.d
Sr	167	628	630	679	913	860	525	468	n.d
Y	39	19	20	18	16	24	20	29	n.d
Zr	278	211	235	235	236	259	222	246	n.d
Nb	12	6	6	6	5	6	6	8	n.d
Pb	38	35	32	20	29	60	32	48	n.d
Th	17	9	11	9	8	13	12	13	n.d

LOI: loss of ignition, Fe_2O_3*: total iron as Fe_2O_3, b.d.l. : below detection limit, n.d. : no data.

The major elements displayed to 3 significant digits, except for MnO.